Ph. D. DISSERTATION

Cooperative Hydration Effect on Water Reorientation Dynamics in Aqueous Electrolyte Solution

전해질 수용액의 물분자 재배향 동역학에 작용하는 협동수화효과에 관한 연구

BY

Seonmyeong Kim

FEBRUARY 2021

DEPARTMENT OF PHYSICS AND ASTRONOMY
COLLEGE OF NATURAL SCIENCE
SEOUL NATIONAL UNIVERSITY

Cooperative Hydration Effect on Water Reorientation Dynamics in Aqueous Electrolyte Solution

전해질 수용액의 물분자 재배향 동역학에 작용하는 협동수화효과에 관한 연구

지도교수 박 건 식

이 논문을 이학박사 학위논문으로 제출함

2020 년 12 월

서울대학교 대학원

물리천문학부

김선명

김선명의 이학박사 학위논문을 인준함

2020 년 12 월

위 원 장	제 원 호	
부 위 원 장	박 건 식	
위 원	박 혜 윤	
위 원	최 현 용	
위 원	박 재 헌	

Abstract

This thesis describes the structure and reorientation dynamics of water in $MgCl_2$ aqueous electrolyte solution by using ab-initio MD simulation and dielectric relaxation spectroscopy method. By using $MgCl_2$, which has strong hydration effect, as a system solute, ion hydration and its cooperativity were investigated. Unlike bulk water, $MgCl_2$ has considerable influences on the hydrogen bond network of water, as confirmed by the analysis of the radial distribution function, hydrogen bond kinetics, and vibrational density of state. Through this, we found the strong interaction with Mg ions bounds the water in the first hydration shell. Also, the weakening of water-water interaction can be found beyond the first hydration shell.

In addition, in this thesis, water molecules' reorientation dynamics were characterized using a cooperative ion hydration model to quantify the cooperative hydration effect. This hydration model showed that the cation-anion mixture effect appears in the reorientation dynamics of water. We have found that water molecules in the second shell of Mg^{2+} and the first shell of Cl^- show retarded reorientation dynamics compared with bulk-like behavior because of cooperative ion hydration.

Finally, through a comparison of macroscopic DRS measurement and MD simulation, we have found that the existing additive concept fails to describe the hydration number changing with the concentration. However, the model considering the cooperative effect of Mg2+ and Cl- can accurately describe the hydration number changing with the concentration. These results can indicate that the cooperative effect in the short-range could be an essential factor in determining macroscopic solvent properties.

Keywords: Ion hydration, cooperative effect, MD simulation, dielectric relaxation spectroscopy, $MgCl_2$

Student number: 2014-21351

Contents

List of Figures

List of Tables

Chapter 1

Introduction

1.1 Water

Water molecules, the most abundant element in our world, is a major constituent of the Earth's surface and the fluid that forms the basis of almost all living organisms in our neighborhood. As the essential component of our planet, water is involved in many phenomena ranging from biochemical processes that occur in vivo to geological processes that occur in the Earth. Since water has an inseparable relationship with our lives, efforts to understand water have a very long history. Since Thales of ancient Greece said that water is the primary essence of nature, numerous scientific efforts have been made to elucidate water composition and structure. In 1781, British scientist Henry Cavendish discovered that water was made up of hydrogen and oxygen, and in 1935 it was first proposed that water molecule is structured through hydrogen bonding. Numerous studies up to date have revealed that

hydrogen bonding is the origin of more than 70 water anomalies, such as high heat capacity and strong surface tension [1]. However, only recently, water's role in various phenomena is recognized for its importance, and it has begun to be studied as an active constituent rather than a passive solvent [2].

Water is a molecule composed of two atoms of hydrogen and oxygen and is formed in a structure in which two hydrogen atoms covalently bond with the central oxygen atom. These two covalent OH bonds occupy two out of a total of four sp^3 hybridized electron pairs, and each OH arm has an angle of 104.5 degrees to each other. Above non-linear structure of water allows the water molecule to have a strong polarity. This polarity makes ions or polar molecules soluble in water. In the case of the remaining two lone pairs, they participate in forming a hydrogen bond structure with hydrogen molecules of adjacent water molecules with δ^+ (partially +) charge. As a result, water molecules form a tetrahedral hydrogen bonding structure with surrounding water molecules as shown in Fig. 1.1. This hydrogen bond is weaker than the strong covalent bond and stronger than the van der Waals interaction and has an energy of about 12 kJ/mol, which is similar to the thermal energy level of 4 kJ/mol at room temperature. Therefore, in the liquid water phase at room temperature, water molecules are constantly breaking and forming due to thermal fluctuations. This water's peculiar dynamics is called reorientation dynamics, which constantly reorients dipolar water molecules in hydrogen bonding network on the picosecond (ps) time scale. Not surprisingly, the reorientation dynamics of water molecules are affected by the nature of the hydrogen bonding network of surrounding water molecules. Therefore, when the hydrogen bond network of water molecules changes, such as the presence of solute molecules or confinement effects, it is possible to see how the above distortion affects the water H-bond network by observing the changes in

reorientation dynamics. In this thesis, the effect of ion solute on the hydrogen bond network and the reorientation dynamics of water in an aqueous electrolyte solution is the main subject.

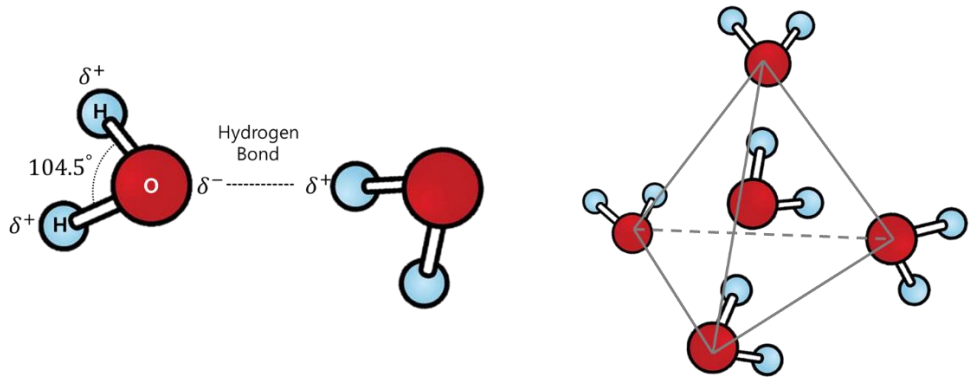

Figure 1. 1 (a) Water molecules in hydrogen bond (b) Tetrahedral hydrogen bonding structure in water

1.2 Aqueous electrolyte solution

1.2.1 Ion hydration

Natural aqueous solutions are far from pure water, being rich in ions, making solution environments highly influential on the macroscopic properties of aqueous solutions — e.g., their viscosity [3] — or to processes involving other solutes in those solutions — e.g., crystal nucleation and growth [4] — relative to pure water. The hydration of ionic solute in a water solvent in an aqueous electrolyte solution can be classified as a solvation process. Solvation is the process by which a dissolved molecule and a solvent interact with each other to reorganize a solvent and a solute into a new solvation complex. In the case of an aqueous electrolyte solution, dissolved ions form a concentric shell of solvent around the ion by ion-dipole interaction, as shown in Fig. 1.2. As above, solvation usually means forming a new solvation complex through bond formation, van der Waals interaction, or hydrogen bonding, and in particular, the process of solvation by water molecules is called hydration.

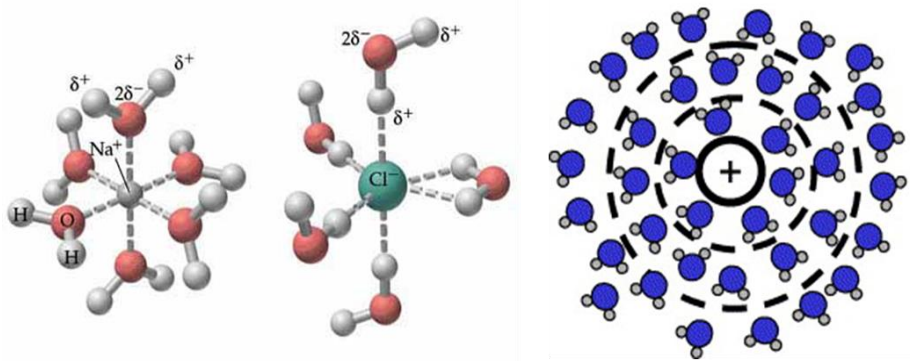

Figure 1. 2 (a) First hydration shell around ion (b) Concentric shell of solvent around the positively charged ion

Therefore, it can be seen that ions in the aqueous electrolyte solution change the structure of the surrounding water molecules while being hydrated, form a hydration shell, and affect macroscopic properties and various bio-chemical processes occurring in aqueous ionic solutions, e.g. for membrane transport, signal transport and nucleation process. It was also discovered in the late 19th century that changes in the macroscopic properties of solutions and the influence of ions in biochemical processes are highly ion-specific. A typical example is the Hofmeister series, which revealed that protein solubility in an aqueous electrolyte solution strongly depends on the ions that are present in solution.

Hofmeister series (effect)

The Hofmeister series has shown that different salts increase or decrease the solubility of proteins in aqueous solutions depending on the type and concentration of salt [5,6]. This Hofmeister series shows that not only protein solubility but also ion-specific effects such as surface tension and protein stability appear with similar sequences in the global biological and physical phenomena, as shown in Fig.1.3. Furthermore, recently, it was found that the Hofmeister series appeared in various enzyme actions and protein folding. Although it has been extensively studied since the 19th century, the critical phenomenon in ion solvation, the Hofmeister series (effect), has not been fully understood at the microscopic level. The most widely accepted explanation is that ions influence the surrounding water structure, and the changed water structure becomes the origin of the Hofmeister effect. Here, different ions are classified into a two group: water structure-makers (“Kosmotropes”) and structure-breakers (“Chaotropes”)

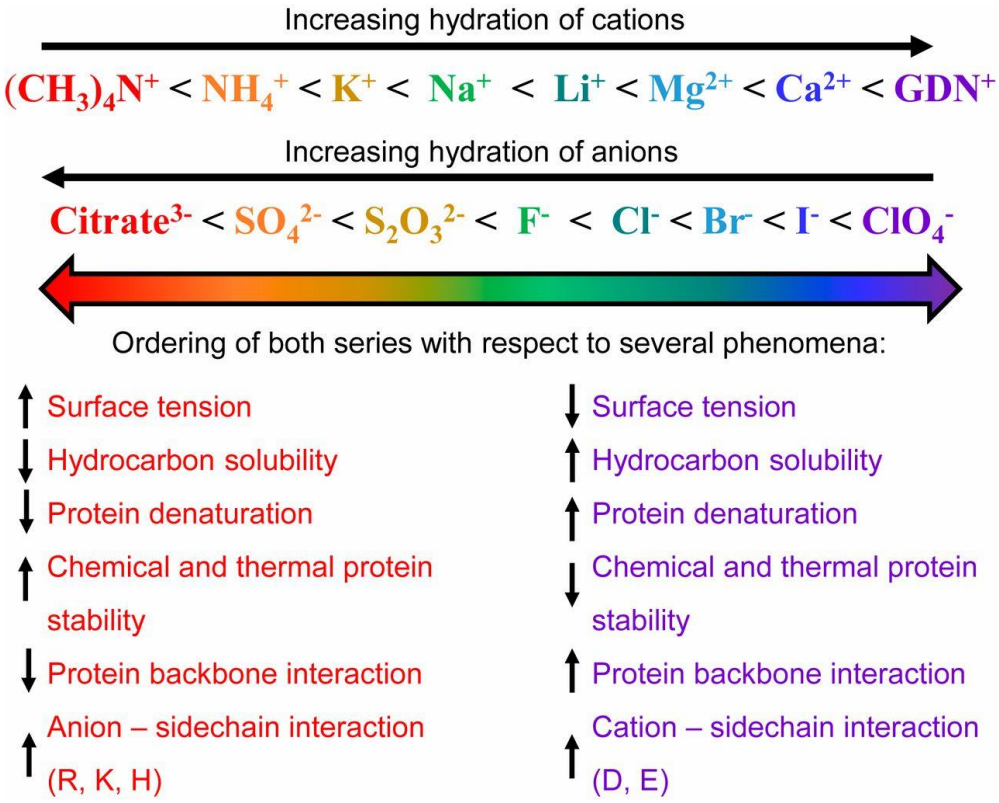

Figure 1. 3 Cationic and anionic Hofmeister series. The ion-hydration series is shown by black arrows, and the corresponding global biological and physical phenomena are listed [7]

1.2.2 Effect of ions on water structure

Water structure making/breaking concept

Ion molecules dissolved in water change the hydrogen bond structure of the surrounding water molecules. Based on the above facts, there have been studies to understand the Hofmeister series in connection with ion ability to alter the water structure. As can be seen in Fig 1.3, in the case of "kosmotropes" such as Ca^{2+} or Mg^{2+}, it can be seen that the ordered hydration layer is formed near the ions, effectively taking water from other solutes (salting out). Conversely, this "chaotrope" like iodide or thiocyanate creates a disordered structure near the ions, creating space for other solutes to dissolve (salting in). According to this view, the key to a complete understanding of the Hofmeister effect is how ions change the hydrogen bond structure of nearby water molecules.

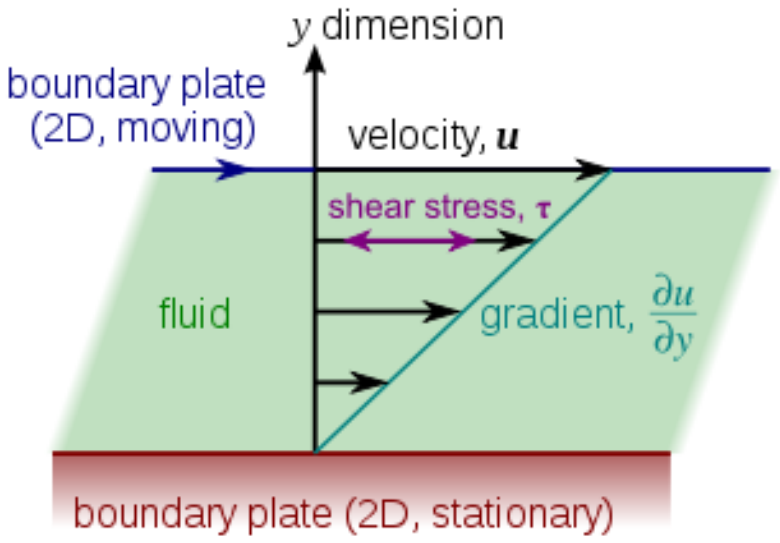

Figure 1. 4 Friction between the fluid and boundaries makes the fluid to shear. The force required for shear stress is dynamic viscosity of fluid.

Dynamic viscosity (η) is a representative example of measuring the degree to which the hydrogen bond structure of water changes with the presence of ions in an aqueous electrolyte solution. Dynamic viscosity is a gradient of shear stress to the relative motion in a fluid layer as shown in Fig 1.4; qualitatively, the fact that fluid has a strong viscosity means that the intermolecular interaction in the fluid is strong and vice versa. The aqueous electrolyte solution exhibits a different viscosity from pure water as ions are added, and the concentration dependence of this relative viscosity, as shown in Fig. 1.5, can be explained by the widely known Jones-Dole empirical formula.

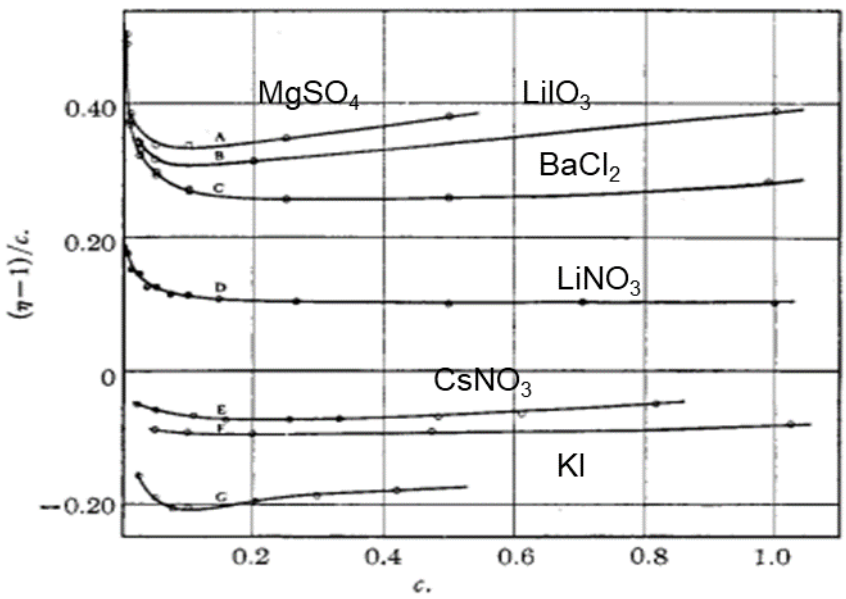

Figure 1. 5 Concentration dependent relative viscosity of various salt solution [9].

Jones-Dole empirical expression at first is developed to interpret fluidity, which is inversely correlated to the relative viscosity. Later original Jones-Dole expression is inverted and recast in terms of the relative viscosity:

$$\frac{\eta}{\eta_0} = 1 + Ac^{1/2} + Bc \qquad (1.1)$$

which is typically used until recently. Some electrolytes require an additional term in the square of the concentration at accessible concentrations:

$$\frac{\eta}{\eta_0} = 1 + Ac^{1/2} + Bc + Dc^2 \qquad (1.2)$$

With A, B, and D being coefficients depending on the solute, solvent, and the temperature. For most salts the term in the square of the concentration is unimportant at $c < 0.5$ mol dm^{-3}, but its inclusion makes the empirical expression (1.2) valid at substantially higher concentrations [8].

The Jones-Dole A-coefficient depends on the interionic interaction and can be evaluated theoretically. Based on the assumption that A-coefficient arises from interionic interaction, A-coefficient is positive in all ions and zero for the neutral solute. The theoretical calculation shows highly match with experimental values. Therefore, Jones-Dole A-coefficient describes ion-ion electrostatic interaction in the electrolyte solution. On the other hand, the B coefficient is theoretically not yet fully understood and is known to depend on the interaction between the ion and the solvent. Interestingly, unlike the A-coefficient, the B-coefficient was both positive and negative, depending on the kind of ion. That is, the positive (negative) B-coefficient means that the ion and the solvent interact in the direction that the viscosity increases (decreases) as the ions dissolved into aqueous solution. Cox and Wolfenden suggest the

Cations	B	Anions	B	
Mg^{2+}	0.385	PO_4^{3-}	0.590	Structure making
Ca^{2+}	0.285	$CH_3CO_2^-$	0.250	
Ba^{2+}	0.22	SO_4^{2-}	0.208	
Li^+	0.150	F^-	0.10	
Na^+	0.086	HCO_2^-	0.052	
K^+	−0.007	Cl^-	−0.007	Structure breaking
NH_4^+	−0.007	Br^-	−0.032	
Rb^+	−0.030	NO_3^-	−0.046	
Cs^+	−0.045	ClO_4^-	−0.061	
		I^-	−0.068	
		SCN^-	−0.103	

Sources: Phosphate, formate, and perchlorate from Krestov (1991); all others from Robinson et al. (1981).

Figure 1. 6 Jones-Dole viscosity B coefficient and classification of structure making/breaking ion; tables from ref [11].

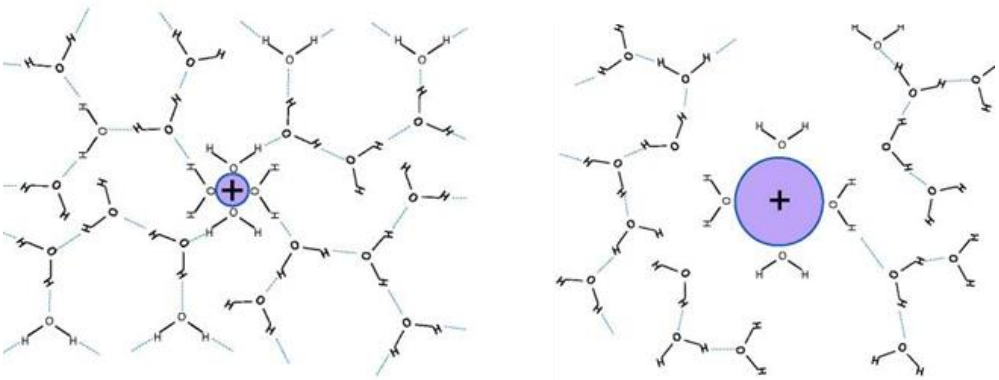

Figure 1. 7 Schematic of water hydrogen bond structure near positively charged ion (a) Structure making ion (b) Structure breaking ion

connection between water structure and viscosity B-coefficient. They mentioned generally applicable explanation of the "negative viscosity" corresponding to negative values of B, is due to"depolymerization" of the solvent water [10]. In other words, structure of water molecules is decreased because of the ion. Based on this concept, if the hydrogen bond structure of the water around the ion is weakened (negative B-coefficient), it is classified as a structure breaker, and if it is strengthened (positive B-coefficient), it is classified as a structure maker. Also, under the assumption that the B-coefficient is additive, the B-coefficient of each ion can be calculated by assuming that the B-coefficient of K^+ and Cl^- ions (having similar mobility) are the same. As shown in Fig 1.6, various ions are divided into structure making/breaking ions based on the viscosity B-coefficient, which can be seen to have high similarity to the ion-specific series appearing in the Hofmeister series.

Critical questions in ion hydration

Although the method to understand the various biochemical processes occurring in aqueous electrolyte solutions through the water structure making/breaking concept is robust and straightforward, several problems have recently been raised. These issues are linked to two critical questions for understanding ion hydration, which have been actively discussed until recently.

(i) To what extent do ions influence hydrogen bond structure and dynamics of the surrounding water molecules?

(ii) Can "Hofmeister series" be understood in terms of individual ion's effect on water

The first question, how many water molecules are affected by ions, can be understood in other words, what is the range of ion hydration? In this regard, the concept that ions change the overall water structure and dynamics has been widely accepted. This concept was understood based on the fact that various bulk properties of aqueous electrolyte solutions, such as viscosity [12], diffusion coefficients [13] and hydration entropy [14], show consistent changes depending on the concentration even when the concentration of ions is very dilute. However, this over-simplified notion has been argued that the range of ion hydration effect may be only limited in few layers through recent experiments [15-17] and simulation studies [18,19]. Especially, spectroscopy studies on electrolyte solution lead to the conclusion that the effect of dissolved salts on the overall structure and dynamics is negligible, only limited to the first few layers. Still, many studies such as neutron diffraction, dielectric spectroscopy and infrared photo-dissociation spectroscopy have yielded controversial results for the range of ion effects on water whether it is a long-range or short-range.

Another issue related to the second question is whether the ion-specific effect can be viewed as the effect of individual ions. This problem is closely related to the additive assumption. In order to measure the degree of structure making/breaking in viscosity, it is assumed that the B-coefficient of each ion is additive in the aqueous electrolyte solution. As such, the additive assumption is used in many ion effects on solvent properties such as enthalpies, Gibbs free energies, and entropies of hydration and solvation. However, recent studies have reported that the changes in water structure or dynamics that occur when ions are dissolved do not appear simply additive. For example, strongly hydrated ions such as Mg^{2+} or SO_4^{2-} have 6 and 1 hydration water per ion (water whose structure or dynamics changed due to the influence of ions),

respectively, when dissolved with weakly hydrated counter ions in an aqueous electrolyte solution. However, when these two ions are dissolved together in the electrolyte, they have 18 hydration water, which is much more than the additive assumption (7 hydration water). The non-additive picture that appears in the aqueous electrolyte solution is called the cooperative effect of ion hydration and is the main subject of this thesis.

1.3 Reorientation dynamics of water

Reorientation dynamics refers to water dynamics in which dipolar water molecules are continuously breaking and forming hydrogen bond on a picosecond timescale by thermal fluctuation. The reorientation dynamics of water by thermal fluctuation was explained as the process by which the molecular dipole moment is rearranged through Brownian motion by P. Debye [20]. Debye's reorientation dynamics model well explains the dielectric relaxation process that occurs when an external oscillating electric field is applied. Therefore, information on the molecular reorientation dynamics of water can be obtained by measuring the dielectric constant in the GHz-THz range electric field (picosecond time window). As mentioned in Section 1.1, since reorientation dynamics react sensitively to changes in the surrounding hydrogen bonding network, we can determine how ions affect the surrounding water structure and dynamics by measuring reorientation dynamics.

In this thesis, we are interested in the molecular level understanding of ion hydration process in electrolyte solutions. There are many studies related to ion hydration, but until recently, many discussions on the range and cooperative effect of ion hydration have been underway. In this context, we want to broaden our understanding of ion hydration through how ions change the reorientation dynamics of surrounding water molecules in aqueous electrolyte solutions. As we have seen above, water reorientation dynamics can be considered divided into two levels; molecular level reorientation dynamics (microscopic) and dielectric relaxation of total polarization (macroscopic). We used MD simulation and dielectric relaxation spectroscopy, respectively, to connect molecular-level understanding and macroscopic dielectric relaxation properties. Through MD simulation, we will investigate

the reorientation dynamics of water affected by ion at the microscopic level and how the cooperative effect is found macroscopically through dielectric relaxation spectroscopy.

1.4 Outlook

This thesis discusses cooperative effect of ion hydration in electrolyte solution using MD simulation and dielectric relaxation spectroscopy. Chapter 2 gives information about the $MgCl_2$ aqueous electrolyte solution as the sample system and details about MD simulation and experimental technique of dielectric relaxation spectroscopy. The solvation structure of electrolyte solution $MgCl_2$ is mainly discussed in the view of ion effect on hydrogen bond structure in Chapter 3 and dynamics in Chapter 4. Finally, we discuss about molecular level cooperative effect in ion hydration and how this results connected to macroscopic dielectric relaxation properties using hydration numbers in Chapter 5

Chapter 2

Materials & Methods

2.1 Molecular dynamics simulation

2.1.1 General principles

The principles of a molecular dynamics simulation are quite simple. It is solving simple Newtonian mechanics with N equation of motion; N is the number of atoms or molecules in the system. Start with the initial condition of the position and velocities of all atoms in the simulation system, we need to calculate the force exerted to the molecule at time t. To calculate the position and velocity of the next step of each atom or molecule, the interaction potential according to the atom position is used to solve the equation of motion in the frame of each atom. Depending on how this interaction potential is calculated, molecular dynamics simulation can be classified into two categories; one is classical MD simulation and the other is Ab-initio MD simulation. As we will

cover in detail in a later section, classical MD simulation approximates interaction potential as pairwise additive potential and Ab-initio MD simulation calculates interaction potential considering the electronic structure of atoms and molecules; in other words, Ab-initio MD simulation counts quantum mechanical consideration as shown in Fig 2. 1.

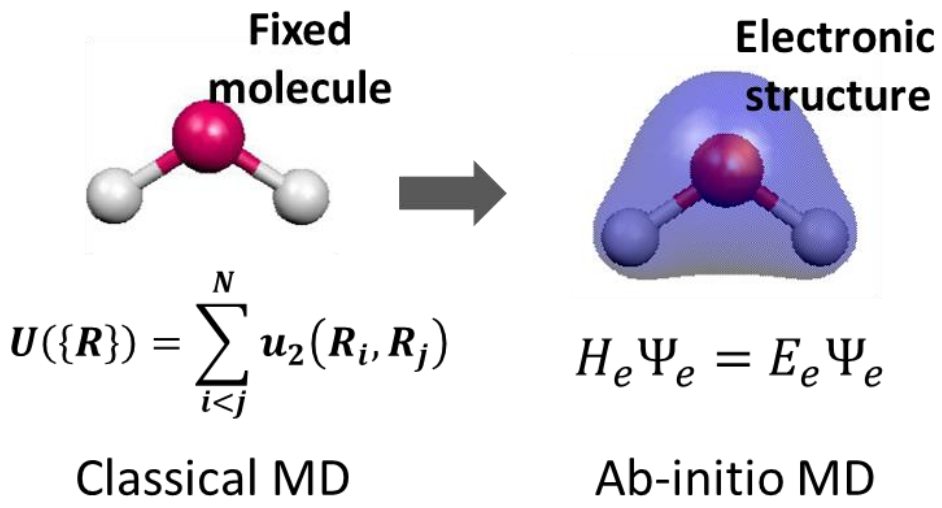

Figure 2. 1 Difference between classical MD simulation and Ab-initio MD simulation

Once molecular configuration (velocity and positions) of the system is determined at a specific time, all other parameters for describing system at that time can be obtained. For example, the temperature can be obtained through average kinetic energy from the velocity data and equipartition theorem. The equations governing the molecular dynamics of an atom I can be written as

$$F_i = -\frac{\partial U}{\partial r_i} = m_i a_i \qquad (2.\ 1)$$

where F_i is the force exerted on atom i, U is the potential energy of the system with all atom positions as variables, a_i and m_i is the acceleration and mass of atom i.

Typical MD simulation is performed as shown in the flow chart below (Fig 2. 2).

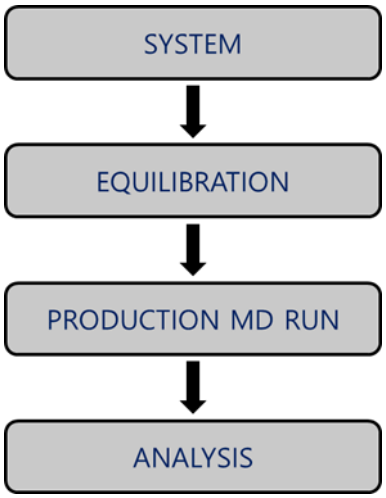

Figure 2. 2 Flow chart of typical MD simulation

First, when system parameters such as the initial configuration, unit cell size, initial temperature, number, and kind of molecules to be simulated are set, it goes through the equilibration step to make the given system into the desired equilibrium state. Through sufficient step equilibration process, you can get the configuration to produce molecular dynamics in a given macroscopic variable such as given Number of atom, volume, energy, temperature and

pressure. Through MD production, each molecule's position and velocity can be obtained over time. And finally, information on structure and dynamics can be reconstructed through this microscopic position and velocity information.

2.1.2 Classical molecular dynamics simulation

Integrating the classical equation of motion

Algorithms to find the next position and velocity using a given field and configuration of MD trajectory are typically given Verlet, velocity Verlet and leapfrog algorithm. Starting from Taylor series expansion up to second order for the position r at time t +Δt:

$$r_i(t + \Delta t) \approx r_i(t) + \Delta t v_i(t) + \frac{\Delta t^2}{2m_i} F_i(t) \qquad (2.\ 2)$$

Similarly, position r at time t -Δt:

$$r_i(t - \Delta t) \approx r_i(t) - \Delta t v_i(t) + \frac{\Delta t^2}{2m_i} F_i(t) \qquad (2.\ 3)$$

And combining equation (2. 2) and (2. 3):

$$r_i(t + \Delta t) \approx 2r_i(t) - r_i(t - \Delta t) + \frac{\Delta t^2}{m_i} F_i(t) \qquad (2.\ 4)$$

Above equation (2. 4) is the well-known Verlet algorithm [21]. Starting from initial position and velocity, one can obtain position at time Δt. Then it can be possible to get trajectory from $-\Delta t$ to Δt using equation (2. 4). The Verlet algorithm does not calculate velocity automatically, so it can be calculated from difference between position at $-\Delta t$ to Δt.

$$v_i(t) = \frac{r_i(t + \Delta t) - r_i(t - \Delta t)}{2\Delta t} \qquad (2.\ 5)$$

The Verlet algorithm has a weakness in that position and velocity are not given simultaneously on the fly; velocity needs to be calculated after getting position first. The velocity Verlet algorithm is modified version that calculate position and velocity at once.

Starting from equation (2. 3) and solve at $\mathrm{t} = \mathrm{t} + \Delta\mathrm{t}$

$$r_i(t) \approx r_i(t + \Delta t) - \Delta t v_i(t + \Delta t) + \frac{\Delta t^2}{2m_i} F_i(t + \Delta t) \qquad (2.\ 6)$$

and substitute the value $r_i(t + \Delta t)$ into equation (2. 2) and recast for v_i

$$v_i(t + \Delta t) \approx v_i(t) + \frac{\Delta t}{2m_i}[F_i + F_i(t + \Delta t)] \qquad (2.\ 7)$$

Combining equation (2. 2) and (2. 7), velocity Verlet algorithm can get position and velocity synchronously. One of the variations of this velocity verlet algorithm is the leapfrog algorithm. Using position at time t, force at time t is calculated. The next step is update velocity at time $t - \frac{\Delta t}{2}$ to velocity at $t + \frac{\Delta t}{2}$ using force at time t. And finally, updating position from t to $t + \Delta t$. Above velocity Verlet and leapfrog method have one crucial advantage: stable for oscillatory motion when the time step is constant and less than half of period of oscillatory motion. Water has many oscillatory motion such as molecular vibration (strethching, bending), libration and rotational reorientation in femtosecond to picosecond. So we choose leapfrog algorithm and short time step (1fs) for stable integration of trajectory.

MD simulation in statistical ensemble

In order to produce molecular dynamics in a given macroscopic variable such as given Number of atom, volume, energy, temperature and pressure, the canonical ensemble (constant NVT) or the isothermal-isobaric (constant NPT) ensemble is typically used for reflecting common experimental condition. The popular method used in the MD simulation to achieve this ensemble condition are the Berendsen and the Nosé-Hoover thermostat [22, 23]. The thermostat mentioned above is a re-scale algorithm to control statistical variables such as energy or temperature of a given system in updating the position and velocity of atoms according to each time step.

The Berendsen algorithm is a method that makes the instantaneous temperature to the target temperature by rescaling the speed in the following way. The basic principle of rescaling assumes that the system is weakly coupled to the heat bath having the target temperature. This situation controls the fluctuation of the system's kinetic energy. This system's temperature is exponentially decayed by the temperature deviation centered on the target temperature, and this can be summarized as an equation as follows.

$$\frac{d\mathrm{T}}{dt} = \frac{T_0 - T}{\tau} \qquad (2.\ 8)$$

Here, T_0 is target temperature, T is system temperature, and τ is the decaying constant depending on coupling degree between heat bath and system. The smaller this decay constant, the faster the timescale at which the heat bath suppresses the fluctuation. Therefore, this decay constant depends on the temperature fluctuation of the system's kinetic energy and usually has a value between 0.5 and 2 ps. In the above heat bath coupling situation, the velocity rescaling constant can be obtained as follows. Equation (2. 8) can be

rewritten in discrete integration concept.

$$\frac{\Delta T}{T} = \frac{\Delta t}{\tau} * \left(\frac{T_0}{T} - 1\right) \tag{2. 9}$$

According to the Equipartition Theorem, since the temperature is proportional to E_{kin} and v^2, it can be converted to the Rescaling factor of velocity through Equation (2. 9). When the above rescaling factor is multiplied by the velocity at time t, the total kinetic energy is rescaled to the timescale to the target temperature. The velocity rescales performed in the integration algorithm. As you can see in Fig 2. 3, velocity is rescaled by thermostat when position and velocity are updated to next step t → t+Δt. Typically, velocity recalling by the thermostat is performed in the last step in the algorithm.

1. VV1:

$$\begin{aligned} \underline{v}(t+\frac{1}{2}\Delta t) &\leftarrow \underline{v}(t) + \frac{\Delta t}{2}\frac{\underline{f}(t)}{m} \\ \underline{r}(t+\Delta t) &\leftarrow \underline{r}(t) + \Delta t\, \underline{v}(t+\frac{1}{2}\Delta t) \end{aligned}$$

2. RATTLE_VV1
3. FF:

$$\underline{f}(t+\Delta t) \leftarrow \underline{f}(t)$$

4. VV2:

$$\underline{v}(t+\Delta t) \leftarrow \underline{v}(t+\frac{1}{2}\Delta t) + \frac{\Delta t}{2}\frac{\underline{f}(t+\Delta t)}{m}$$

5. RATTLE_VV2
6. Thermostat:

$$\begin{aligned} \chi(t+\Delta t) &\leftarrow \left[1 + \frac{\Delta t}{\tau_T}\left(\frac{\sigma}{E_{kin}(t+\Delta t)} - 1\right)\right]^{1/2} \\ \underline{v}(t+\Delta t) &\leftarrow \underline{v}(t+\Delta t)\,\chi \ . \end{aligned}$$

Figure 2. 3 Velocity Verlet algorithm with Berendsen thermostat

In general, thermostats do not generate accurate canonical ensembles for small systems. Still, in systems with hundreds/thousands of atoms or molecules, most properties approximately match statistical ensembles. Berendsen thermostat is used because it has good efficiency to relax the system's temperature with the target temperature. However, since the Nose-Hoover thermostat generates a more accurate trajectory of the canonical ensemble, in many cases, the simulation system is initially equilibrated with a Berendsen thermostat and later equilibrated with a Nosé-Hoover thermostat.

The Nosé-Hoover thermostat is a algorithm for constant-temperature molecular dynamics simulation such as canonoical ensemble. The main idea is to simulate with fixed particle number N, the volume V and the temperature T. Similar to the Berendsen thermostat's assumption, the Nosé-Hoover thermostat introduces an extra degree of freedom for heat bath s into Hamiltonian governing molecular dynamics simulation.

$$\mathcal{H}_{\text{Nose}} = \sum_{i=1}^{N} \frac{P_i^2}{2m_i s^2} + U(r_1, \dots, r_N) + \frac{p_s^2}{2Q} + gkTln\, s \qquad (2.\ 10)$$

Here, $U(r_1, \dots, r_N)$ is the potential energy, k and T are Boltzmann constant and Target temperature, and g is the number of independent momentum degrees of freedom of the system (ensemble average at g = 3N is equal to the canonical ensemble). In Nosé Hamiltonian, s actually regulate the system temperature to target temperature through scales the velocities. Q is a parameter related to time scales of which thermostat regulates the thermal fluctuation of the system. The equations of motion from Nosé Hamiltonian are as belows.

$$\dot{r}_i = \frac{\partial \mathcal{H}_{\text{Nose}}}{\partial p_i} = \frac{\mathrm{P_i}}{m_i s^2}$$
$$\dot{p}_i = -\frac{\partial \mathcal{H}_{\text{Nose}}}{\partial r_i} = F_i$$
$$\dot{s} = \frac{\partial \mathcal{H}_{\text{Nose}}}{\partial p_s} = \frac{p_s}{Q} \qquad (2.\ 11)$$
$$\dot{p_s} = -\frac{\partial \mathcal{H}_{\text{Nose}}}{\partial s} = \frac{1}{s}\left[\sum_{i=1}^{N} \frac{P_i^2}{m_i s^2} - gkT\right]$$

Above equation of motion can be simplified introducing coordinates as follows.

$$\mathrm{P_i'} = \frac{\mathrm{P_i}}{s},\ t' = \int^t \frac{d\tau}{s},\ r_i' = r_i,\quad \frac{1}{s}\frac{ds}{dt'} = \frac{d\eta}{dt'} \qquad (2.\ 12)$$

And rearrange equation (2. 11) using (2. 12):

$$\dot{r}_i = \frac{P_i}{m_i}$$
$$\dot{p}_i = F_i - \frac{p_\eta}{Q} P_i$$
$$\dot{\eta} = \frac{p_\eta}{Q} \qquad (2.\ 13)$$
$$\dot{p_\eta} = \sum_{i=1}^{N} \frac{P_i^2}{m_i} - gkT$$

Above equation of motion has the form of frictional forces exerted to the momentum depends on p_η. Furthermore, this friction term is driven by the

energetic difference between instantaneous kinetic energy and canonical heat bath thermal energy. Furthermore, this friction term is driven by the energetic difference between instantaneous kinetic energy and canonical thermal energy of heat bath. Therefore, this frictional term can regulate instantaneous kinetic energy fluctuation and control the system to have the constant energy level of the heat bath.

Force field molecular dynamics simulation

In classical MD simulation, force fields are empirical potential form that well reproduce exact potential energy surface of the system. Then forces exerted on atom or molecule can be obtained as the gradients of the potential energy in the molecular frame. The empirical potential can be defined based "ball and spring" model for the atoms. The electronic structure is ignored in this model. This empirical potential function is usually approximated by pair-wise additive potential as shown in Fig 2. 4.

$$U(\{R\}) = \sum_{i}^{N} u_1(R_i) + \sum_{i<j}^{N} u_2(R_i, R_j) + \sum_{i<j<k}^{N} u_3(R_i, R_j, R_k) + \cdots$$

$$\Downarrow$$

$$U(\{R\}) = \sum_{i<j}^{N} u_2(R_i, R_j)$$

Figure 2. 4 Pair-wise additive potential function

Typically, this pairwise potential expanded by bonded interaction term and non-bonded interaction term. The parameterization (value of K) is different depending on the system and usually fitting to the results of ab initio calculation.

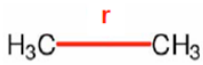

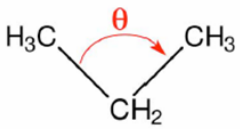

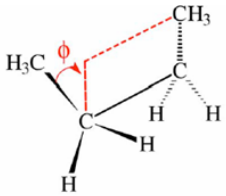

$$\sum_{bonds} K_b(r - r_0)^2 \qquad \sum_{angles} K_\theta(\theta - \theta_0)^2 \qquad \sum_{dihedrals} K_\varphi(1 + \cos(n\varphi - \delta))$$

$$\sum_{i>j} \frac{q_i q_j}{4\pi\varepsilon_0 \varepsilon r_{ij}} \qquad \sum_{i>j} \varepsilon_{i,j} \left[\left(\frac{r_{ij}^{min}}{r_{ij}} \right)^{12} - 2 \left(\frac{r_{ij}^{min}}{r_{ij}} \right)^{6} \right]$$

Figure 2. 5 Bonded and non-bonded pair-wise additive interaction potential

As shown in Fig. 2. 5, there are typical examples of bonded and non-bonded interaction potential. The above three terms account for bonded interaction related with bond, angle and dihedral respectively. The below two terms are non-bonded interaction related with Coulomb interaction between molecules and a van der Waals interaction. Depending on which system is being simulated, the interaction potential should be determined by carefully considering which interaction to include and each coefficients of the interaction.

However, considering that MD simulation is generally performed in

an extensive system, the larger the number of molecules, the larger the computational cost for calculating the non-bonded term. In order to reduce computational cost, relatively weak and short-ranged van der Waals interaction are usually calculated only up to interaction with molecule within "cutoff" distance as shown in Fig 2. 6.

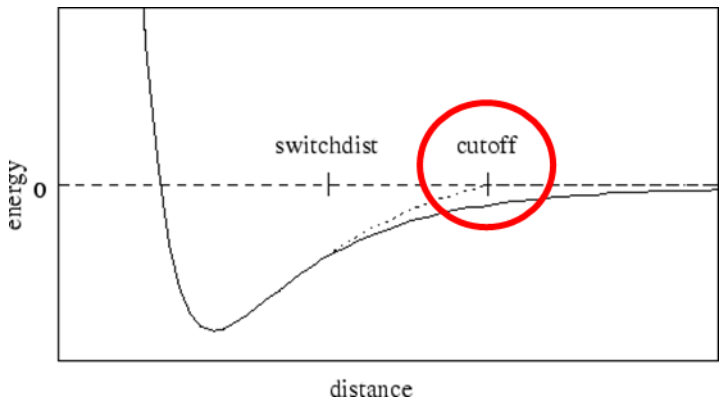

Figure 2. 6 Lennard-Jones potential and cutoff distance

As seen above, Classical MD simulation has limitation calculating the interaction potential without considering the electronic structure of the molecule, but assuming a pair-wise potential (higher-order term is neglected), and ignoring the interaction beyond the cutoff distance. When these limitations are no longer negligible and have substantial effects, classical MD simulation fails to reproduce system well.

2.1.3 Ab-initio molecular dynamics simulation

Unlike classical MD, Ab-initio molecular dynamics simulation considers the electronic structure of an atom or molecule, so processes including charge transfer or polarization, or hydrogen bonding, can be more accurately simulated. In order to consider electronic structure of the molecule, Ab-initio molecular dynamics simulation use Schrödinger equation to find exact potential energy surface.

$$\hat{\mathcal{H}}\Psi_0 = E_0\Psi_0 \tag{2. 14}$$

Here, Ψ_0 is the wave function, $\hat{\mathcal{H}}$ is the Hamiltonian operator of total energy, and E_0 is the total energy of the system. Among the most widely used molecular Hamiltonian, "Coulomb Hamiltonian" is written as follows.

$$\begin{aligned}\hat{\mathcal{H}} = -\frac{1}{2}\sum_i \nabla_i^2 - \frac{1}{2M_a}\sum_a \nabla_a^2 - \sum_{a,i}\frac{Z_a}{r_{ai}} \\ + \sum_{a>b}\frac{Z_a Z_b}{R_{ab}} + \sum_{i>j}\frac{1}{r_{ij}}\end{aligned} \tag{2. 15}$$

Above Coulomb Hamiltonian, the kinetic energy of the electrons, the kinetic energy of the nuclei, the Coulombic interaction energy between electrons and nuclei, the Coulombic interaction energy between nuclei, and the Coulombic interaction energy between electons are included in order. The above equation can be rewritten to make the variables more clear.

$$\begin{aligned}\hat{\mathcal{H}} = \hat{T}_e(r) + \hat{T}_N(R) + \hat{V}_{eN}(r,R) \\ + \hat{V}_{NN}(R) + \hat{V}_{ee}(r)\end{aligned} \tag{2. 16}$$

Here, r is the set of electronic coordinates and R is the set of nuclear coordinates and each operator corresponds to the operator in equation (2. 15) in order.

Born-Oppenheimer approximation

The Born-Oppenheimer approximation is basically separate important two steps in MD simulation. For obtaining potential energy surface, electronic structure is considered and Schrödinger equation is used. However, given potential energy surface, molecular trajectory (nucleus) is described in Newtonian mechanics same as classical MD. Above can be realized based on assumption as follows: In a frame of fast-moving electrons, the motion of a much heavier nucleus is almost negligible and can therefore be assumed static. On the contrary, from a nucleus perspective, it can be seen as moving by the average field applied by fast-moving electrons. Based on above scheme, Schrödinger equation is solved for fixed nuclear coordinates R:

$$\begin{aligned} \widehat{\mathcal{H}}_{el}\phi_{el}(r;R) &= E_{el}\phi_{el}(r;R) \\ \Psi(\mathrm{r},\mathrm{R}) &= \phi_{el}(r;R)\psi_N(R) \end{aligned} \qquad (2.\ 17)$$

where E_{el} is the electronic energy, $\Psi(\mathrm{r},\mathrm{R})$ is the total wave function and $\phi_{el}(r;R)$ is the electronic wave function and $\psi_N(R)$ is the nuclei waver function. Looking at the above wave function, the two degrees of freedom in the system, electronic and nuclear, can be un-linked. The electron Hamiltonian operator in equation (2. 17) is the same as the total Hamiltonian in equation (2. 16) leaving only the term with electron contribution.

$$\widehat{\mathcal{H}}_{el} = \hat{T}_e(r) + \hat{V}_{eN}(r,R) + \hat{V}_{NN}(R) + \hat{V}_{ee}(r) \qquad (2.\ 18)$$

Using the electron Hamiltonian above, expanding the solution of the total Schrödinger equation into the eigenstates of the electronic Hamiltonian and neglecting the coupling term due to the non-adiabatic effect, the Schrödinger equation for the nucleus can be written as:

$$\left[\hat{T}_N + E_{el}\right]\psi_N = E_k\psi_N \tag{2. 19}$$

Solving the time dependent Schrödinger equation (2. 20) using above eigenstates from time independent Schrödinger equation.

$$i\frac{\partial}{\partial t}\Psi = \hat{\mathcal{H}}\Psi \tag{2. 20}$$

Using Born-Oppenheimer approximation to separate nuclear and electronic motion, Newton equation of motions for nuclei which are treated as "classically" become:

$$M_I\ddot{R}_I(t) = -\nabla_I < \Psi_{el}|\hat{\mathcal{H}}_{el}|\Psi_{el} > \tag{2. 21}$$

Molecular dynamics simulation using the Born-Oppenheimer approximation (BOMD) has the advantage of reflecting the electronic structure; but, it has the disadvantage of requiring a high computational cost. This high computational cost is reduced by introducing the density functional theory, and ab-initio MD could be used in a many different systems.

Density functional theory

One of the most widely used methods in the density functional theory is the Kohn-Sham method. In the Kohn-Sham method, the Eigenstates are obtained through non-interacting N fictitious electrons of which the density

and energy of the fictitious electrons are identical to the real system. For above non-interacting electrons, electronic Hamiltonian can be written as the one particle operator for Schrödinger equation.

$$\widehat{\mathcal{H}}_e^{KS} = \sum_i \left[-\frac{1}{2}\nabla_i^2 + V_{eff}(r_i) \right] = \sum_i \hat{h}_{eff}^{KS} \tag{2. 22}$$

Here, V_{eff} is the effective potential for Kohn-Sham model that the fictitious electron density is identical to the electron density of the real system. The Schrödinger equation for fictitious electron can be written using above Kohn-Sham Hamiltonian in equation (2. 22).

$$\widehat{\mathcal{H}}_e^{KS}\Psi_0^{KS} = E_0^{KS}\Psi_0^{KS} \tag{2. 23}$$

Above solution Ψ_0^{KS} can be written as a Slater determinant of orthonormal eigenstates from single particle Schrödinger equation.

$$\begin{gathered} \Psi_0^{KS} = \frac{1}{\sqrt{N}}|\psi_1, \dots, \psi_N| \\ \hat{h}_{eff}^{KS}\psi_i = \epsilon_i\psi_i \end{gathered} \tag{2. 24}$$

Moreover, the electron density of above fictitious system can be obtained by summation of above orbitals.

$$\mathrm{n(r)} = \sum_i |\psi_i(r)| \tag{2. 25}$$

Now, by the Kohn-Sham method, the problem that needs to be solved by considering all N electrons has been reduced to having only electron density at position r as a variable. In general, the effective Kohn-Sham potential in equation (2. 22) has the following expression

$$\mathrm{V_{eff}}(r) = \sum_{i,j} \frac{Z_I}{|R_I - r|} + \int \frac{n(r')}{|r - r'|} dr' + V_{XC}(n(r)) \qquad (2.\ 26)$$

where the successive terms, interaction energy with external potential given by the nuclei ($\mathrm{V_{ext}}$), electronic Hartree potential ($\mathrm{V_H}$), and the local exchange-correlation potential. Finally, replace $\mathrm{V_{eff}}(r)$ in equation (2. 22) to equation (2. 26) then we get ground-state electronic energy of system as a functional of the electronic density n(r) from fictitious system which is identical to electronic energy of real system.

$$E_0^{KS} = -\frac{1}{2}\sum_i < \psi_i|\nabla_i^2|\psi_i > + \int V_{ext} n(r) dr + \frac{1}{2}\int V_H n(r) dr + E_{XC}(n(r)) \qquad (2.\ 27)$$

Gaussian plane wave method

The ground state electron wave function Ψ_o minimize the energy of the electronic Hamiltonian.

$$\mathrm{E_0}(\{R\}) = \min_{\Psi_0} < \Psi_0|\mathcal{H}|\Psi_0 > \qquad (2.\ 28)$$

Here, the ground state energy can be obtained alternatively by minimizing energy of fictitious electron system with respect to the $\{\psi_i\}$ in the Kohn-Sham density function theory scheme $\Psi_0 = \det\{\psi_i\}$

$$\mathrm{E_0^{KS}}(\{R\}) = \min_{\{\psi_i\}} < \Psi_0|\mathcal{H}|\Psi_0 > \qquad (2.\ 29)$$

Typically, the Kohn-Sham single-particle orbitals $\{\psi_i\}$ can be expanded with a basis of $\{\phi_\alpha\}$ where $\{c_\alpha^{(i)}\}$ are the coefficients set for i-th electron orbital.

$$\psi_i = \sum_{\alpha} c_{\alpha}^{(i)} \phi_{\alpha} \qquad (2.\ 30)$$

The most widely used basis sets for above expansion is atom-centered Gaussian wave functions [24]. Then Gaussian wave function expansion (2. 30) for the orbitals can be used for ground state electronic energy as a function of the expansion coefficient $\{c_{\alpha}^{(i)}\}$ using gradient based minimization.

(i) Getting gradient of hypersurface of E_0^{KS} with respect to expansion coefficient $\{c_{\alpha}^{(i)}\}$

(ii) Approach to the minimum using steepest descent gradient

With potential energy surface E_0^{KS} and its gradient in terms of atomic position, we can conduct MD simulation in the same way in the classical MD; calculate interaction potential, force exerted to nuclei at time t are evaluated and update atomic configuration for t+Δt.

2.1.4 Sample system ($MgCl_2$) & Simulation details

In this thesis, the Classical MD and Ab-initio MD were used to investigate the hydration of ions in aqueous electrolyte solution at molecular level. Isolated metal ions such as Mg^{2+}, Ca^{2+}, K^+, Na^+, Cs^+ and Cl^- are simulated at both level (classical & ab-initio MD) to observe solvation structure and effect of individual ion on water structure and dynamics. For observing cooperative hydration effect on water reorientation dynamics, we choose $MgCl_2$ aqueous electrolyte solution as sample solution because it has strong hydration effect compare to other metal ion such as K^+, Na^+, Cs^+. Also, we can see the cooperative ion hydration effect occurring in the aqueous electrolyte solution by comparing the hydration properties of the $MgCl_2$ electrolyte aqueous solution and the hydration properties of the isolated Mg^{2+} and isolated Cl^- solutions. In addition, according to many study [25,26], the ion pairing phenomenon was observed in the sample solution, MgCl2, which shares solvent water due to the close distribute on of ions of opposite charges. Therefore, it becomes a good sample salt solution to check how the effect of individual ion effects on water structure and dynamic changes in a situation where opposite charges are distributed close together, such as ion pairing.

Classical molecular dynamics simulation

Classical dynamics simulations were performed using version 4.03.3 of the DL_POLY molecular dynamics package [27]. The leapfrog algorithm with a time step of 5 fs was used to integrate the equations of motion. The isothermal-isobaric (constant NPT) ensemble was used to maintain a temperature of 300 K and a pressure of 1 bar. The weak-coupling algorithms of Barendsen and co-workers [28] were used with 0.1 ps and 1.0 ps as the

thermostat and barostat relaxation times, respectively. The electrostatic forces were calculated by means of the Ewald summation method [29]. A value of 0.54722sÅ-1 was used for the Ewald convergence parameter with a 6.0 Å cutoff for the real-space part of the Ewald sum. A value of 14 was used for the maximum k-vector index in all three directions in the reciprocal space. Together these three parameters correspond to a relative error in the Coulombic energy of 10-6. A 6.0 Å cutoff was also used for the van der Waals forces. The water molecules were represented using the extended simple point charge (SPC/E) potential [30]. In the SPC/E model, the geometry of the water molecule is fixed such that the OH distance is 1.0 Å and the HOH angle is equal to 109.47°. The geometry of the water molecules was held fixed by the SHAKE algorithm [31]. The interactions between Mg–Cl, Mg–Mg, Cl–Cl, Mg–O and Cl–O and were described using the Lennard-Jones potential parameters parameterised by Dang and co-workers.

Ab-initio molecular dynamics simulation

Simulations were conducted with the electronic structure code CP2K/Quickstep code, version 4.1 [32]. CP2K implements DFT based on a hybrid Gaussian plane wave. The Perdew-Burke-Ernzerhof (PBE) [33] generalized-gradient approximations for the exchange and correlation terms were used together with the general dispersion correction termed DFT-D3 developed by Grimme at al. [34] to provide a more accurate description of the structure of liquid water [35, 36]. The Goedecker-Teter-Hutter pseudopotentials were used to describe the core-valence interactions [37]. All atomic species were represented using a double-zeta valence polarized basis set. The plane wave kinetic energy cut off (E_{cut}) was set to 1000 Ry. Table 2. 1 reports a comparison of the solvation structure of the hydrated cations (isolated ion, no counter ions) considered in this study (Mg^{2+}, Ca^{2+}, Na^{+}, K^{+} and Cs^{+}) with

System	Reference	Method [a]	Functional	Pseudopot. [b]	Basis set [c]	r_{max}	$g(r_{max})$	CN
Na^+	This study	BOMD	PBE-D3	GTH	DZVP/PW (1000 Ry)	2.41	5.0	5.1
		BOMD	revPBE-D3	GTH	DZVP/PW (1000 Ry)	2.53	4.6	5.6
	Duignan et al. [38]	BOMD	revPBE-D3	GTH	DZVP/PW (400 Ry)	2.51	4.1	
		BOMD	SCAN	GTH	DZVP/PW (1200 Ry)	2.36	5.9	
	Galib et al. [39]	BOMD	revPBE	GTH	TZV2P/PW (400 Ry)	2.45	5.8	5.7
		BOMD	revPBE-D3	GTH	TZV2P/PW (400 Ry)	2.53	4.8	6.0
		BOMD	revPBE	GTH	DZVP/PW (400 Ry)	2.46	5.7	5.7
		BOMD	revPBE-D3	GTH	DZVP/PW (400 Ry)	2.56	4.0	6.1
		BOMD	BLYP	GTH	TZV2P/PW (400 Ry)	2.40	5.9	4.9
		BOMD	BLYP-D2	GTH	TZV2P/PW (400 Ry)	2.46	6.4	5.7
NaCl (6 m)	Galib et al.[39]	EXAFS				2.37		5.4
		XRD				2.38		5.5
NaCl (2.5 m)	Galib et al.[39]	XRD				2.38		5.9
K^+	This study	BOMD	PBE-D3	GTH	DZVP/PW (1000 Ry)	2.80	3.4	6.2
	Duignan et al.[38]	BOMD	revPBE-D3	GTH	DZVP/PW (400 Ry)	2.98	3.1	
		BOMD	SCAN	GTH	DZVP/PW (1200 Ry)	2.78	3.8	
	Glezakou et al.[40]	EXAFS				2.76		6.1
Cs^+	This study	BOMD	PBE-D3	GTH	DZVP/PW (1000 Ry)	3.17	2.7	5.9
	Roy et al.[41]	BOMD	PBE-D3	PAW	PW (30 Ry)	3.15	3.3	
Mg^{2+}	This study	BOMD	PBE-D3	GTH	DZVP/PW (1000 Ry)	2.11	13.5	6.0
	Di Tommaso et al.[42]	CPMD	PBE	USPP	PW (30 Ry)	2.08	12.3	6.0
	Callahan et al.[43]	XRD				2.0-2.12		6.0
Ca^{2+}	This study	BOMD	PBE	GTH	DZVP/PW (1000 Ry)	2.40	10.8	6.0
		BOMD	PBE-D3	GTH	DZVP/PW (1000 Ry)	2.40	10.2	6.0
		BOMD	BLYP	GTH	DZVP/PW (1000 Ry)	2.40	9.6	6.3
		BOMD	BLYP-D3	GTH	DZVP/PW (1000 Ry)	2.42	9.9	6.8
		BOMD	revPBE	GTH	DZVP/PW (1000 Ry)	2.43	9.4	6.6
		BOMD	revPBE-D3	GTH	DZVP/PW (1000 Ry)	2.39	10.8	6.1
	Di Tommaso et al.[42]	CPMD	PBE-D3	GTH	DZVP/PW (1000 Ry)	2.36	8.5	6.4
	Bako et al.[44]	CPMD	BLYP	NCPP	PW (70 Ry)	2.45	10.5	6
$CaCl_2$ (6 m)	Fulton et al.[45]					2.43		7.2

[a] BOMD = Born-Oppenheimer molecular dynamics, CPMD = Car-Parrinello Molecular Dynamics. [b] GTH = Goedecker-Teter-Hutter; USPP = Ultra-Soft Pseutopotential; PAW = projector augmented wave; NCPP = Norm-Conserving Pseudopotential. [c] DZVP = double-zeta valence polarized; TZV2P = triple-zeta valence doubly polarized; PW = plane wave.

TABLE 2. 1 Structural properties of the cation–water radial distribution functions obtained from the *ab initio* MD simulations of the hydrated ions (isolated ion, no counterion). The positions, r_{max}, and amplitudes, $g(r_{max})$, of first peak and the average coordination number (CN) of the cation hydration shell are compared with other *ab initio* MD studies and available experimental data. Distances in Å.

the data obtained from other simulations and experimental measurements, from which we can deduce that the PBE-D3 functional with the hybrid Gaussian (DZVP) plane wave (E_{cut} = 1000 Ry) basis set gives an accurate representation of the first hydration shell structure. The k-sampling was restricted to the Γ point of the Brillouin zone. Simulations were carried out with a wave function optimization tolerance of 10^{-6} au. Periodic boundary conditions were applied throughout. The ab initio MD simulations were carried out in the canonical constant volume, constant temperature (NVT) ensemble using a Nosé-Hoover chain thermostat to maintain the average temperature at 300 K with 0.1 ps as the thermostat relaxation time

Simulation protocol

Details of the electrolyte solutions considered in this thesis (number of ions and water molecules, average cell lengths and system concentrations) are reported in Table 2. 2. First, classical MD simulations of 729 water molecules in the isothermal-isobaric constant pressure, constant temperature (NPT) ensemble were conducted to generate an equilibrated aqueous solution. The last configuration was then used to generate $MgCl_2$(aq) with concentrations ranging from 0.1 to 2.8 mol kg^{-1} by randomly replacing N water molecules with N/3 Mg^{2+} and 2N/3 Cl^- ions. As the formation of Mg^{2+}/Cl^{-1} contact ion pairs (CIPs) has been subject to some debate, [25, 46] for the 0.63 and 1.30 mol kg^{-1} solutions we generated two set of initial configurations, with and without CIPs. Each system was subject to 6 ns of classical MD (NPT) simulations to equilibrate the cell volume using the Mg - O and Mg - Cl Lennard Jones potential parameterized by Aqvist [47] together with the SPC/E water model.[30] This combination of force fields has been shown to provide a reasonable description of the structure and dynamic properties of hydrated Mg^{2+}.[48] The last configuration was used to initiate ab initio MD. Table 2. 3

System	#	c (molkg^{-1})	n_{pairs}	n_{water}	Cell length (Å)	Mg–Cl ion pairing
Bulk water	1	0.00	0	729	28.0	
$MgCl_2$	2	0.08	1	726	28.0	*without* ion pairing
	3	0.15	2	723	27.8	*without* ion pairing
	4	0.63	8	705	27.8	*without* ion pairing
	5	0.63	8	705	27.7	*with* ion pairing
	6	1.30	16	681	27.7	*without* ion pairing
	7	1.30	16	681	27.7	*with* ion pairing
	8	2.81	32	633	27.4	*with* ion pairing
CsCl	9	0.63	16	710	27.7	
Mg^{2+}	10	0.88	1	63	12.3	
Ca^{2+}	11	0.88	1	63	12.4	
K^+	12	0.88	1	63	12.5	
Na^+	13	0.88	1	63	12.5	
Cs^+	14	0.88	1	63	12.5	
Cl^-	15	0.88	1	63	12.5	

TABLE 2. 2 Details of the electrolyte solutions: concentration (c) in molkg^{-1}, number of units and H_2O molecules, cell length after classical MD (NPT) simulation, presence of Mg^{2+}–Cl^- contact ion pairs at the initial coordinates of the ab initio MD simulation of $MgCl_2$ solutions.

System	c (mol.kg^{-1})	CIP (%)	SSHIP (%)	SSIP (%)
2	0.08	0.0	29.8	70.2
3	0.15	0.0	0.0	100.0
4	0.63	0.0	58.4	35.0
5	0.63	25.0	32.1	42.9
6	1.30	0.0	93.4	6.6
7	1.30	50.0	41.9	8.1
8	2.81	56.2	43.7	0.0

TABLE 2. 3 Ion pairing of magnesium chloride:

The speciation of magnesium chloride ion pairs as a function of concentration determined in terms of the following ion pairing criteria: contact ion pair (CIP) when Mg^{2+} and Cl^{-} are in direct physical contact; a SSHIP is considered when Mg^{2+} and Cl^{-} are separated by one water molecule; solvent-shared ion pairs (SSHIP) when Mg^{2+} and Cl^{-} are separated by one water molecule; solvent-separated ion pairs (SSIP) when Mg^{2+} and Cl^{-} are separated by two water molecules; free ion pairs (FIP) when the above conditions are not met, and the cation and anion are fully hydrated beyond the second hydration shell. Assignments made according to the analysis of the Mg–O and Mg–Cl radial distribution functions (RDFs): CIP if $r_{Mg-Cl} \leq r_{Mg-Cl}^{min1}$; SSHIP if $r_{Mg-Cl}^{min1} < r_{Mg-Cl} \leq r_{Mg-Cl}^{min2}$; SSIP if $r_{Mg-Cl}^{min2} < r_{Mg-Cl} \leq \left(r_{Mg-O}^{min2} + r_{Cl-O}^{min2}\right)$, where r_{Mg-Cl}^{min1} and r_{Mg-Cl}^{min2} are the positions of the first and second minima, respectively, of the Mg–Cl, Mg–O and Cl–O radial distribution functions, where r_{Mg-X}^{min1}, r_{Mg-X}^{min2} are the positions of the first and second minima, respectively, of the M–X (X = O and Cl) radial distribution function, and r_{Cl-O}^{min2} is the position of the second minima of the Cl–O RDF.

reports the percentages of contact ion pairs (CIP), solvent-shared ion pairs (SSHIP), and solvent-separated ion pairs (SSIP) in the 0.1–2.8 mol kg^{-1} MgCl2 solutions. The more diluted solutions (0.1–0.6 mol kg^{-1}) display a non-monotonous variation of the contact, solvent-shared and solvent-separated ion pairs, which could be related to initial configuration effects because of the slow water dynamics around Mg^{2+} (order of microseconds) [49] and the low number of ions in the simulation box. We have also conducted simulations of pure liquid water, of 0.63 mol kg^{-1} CsCl(aq), and of the hydrated ions Mg^{2+}, Ca^{2+}, Cs^{+}, Na^{+}, K^{+} and Cl^{-1}. For the ab initio MD simulations of $MgCl_2$(aq), each time step required, on average, 45 seconds on 288 cores of the ARCHER UK National Supercomputing Service. The ab initio MD simulations reported herein required approximately 890k CPU hours (wall-clock time × number of processors). Statistics were collected for a period of 20 ps.

2.2 Dielectric relaxation spectroscopy

2.2.1 Theoretical background

Electromagnetic waves and Maxwell equations

The dielectric relaxation spectroscopy is measuring method for dielectric response of given system to electromagnetic fields. In order to understand the dielectric relaxation spectroscopy and relation with physical properties of system in dielectric response, light-matter interaction should be understood first. The electromagnetic wave can be described by Maxwell's equations.

$$(a)\ \vec{\nabla}\cdot\vec{D}=0, \qquad (b)\vec{\nabla}\cdot\vec{B}=0$$
$$(c)\ \vec{\nabla}\times\vec{E}+\frac{\partial\vec{B}}{\partial t}=0, \qquad (d)\ \vec{\nabla}\times\frac{\vec{B}}{\mu_0}-\frac{\partial\vec{D}}{\partial t}=0 \tag{2. 31}$$

Here, $\vec{E}$ is the electric field, $\vec{B}$ is the magnetic field, $\vec{D}$ is the dielectric displacement and μ_0 is the permeability at vacuum. The dielectric displacement $\vec{D}$ can be written with vacuum permittivity ϵ_0 and complex permittivity $\tilde{\epsilon}$ when the electric field at angular frequency ω exerted on the system as follows.

$$\vec{D}(\omega)=\epsilon_0\vec{E}(\omega)+\vec{P}(\omega)=\epsilon_0\tilde{\epsilon}(\omega)\vec{E}(\omega) \tag{2. 32}$$

Here, $\vec{P}(\omega)$ is the induced polarization by electric field $\vec{E}(\omega)$ and $\tilde{\epsilon}(\omega)$ is the complex permittivity, which relates the polarization to the applied electric field. In Maxwell equation, by taking the curl of equation (2. 31) (c) and solve it using (a) and (d), we can obtain wave equation for electric field as equation (2. 33).

$$\nabla^2\vec{E}(r,t) = \mu_0\epsilon_0\frac{\partial^2\tilde{\epsilon}\vec{E}(r,t)}{\partial t^2} \quad (2.\ 33)$$

By using Fourier transformation, we can solve wave equation in the frequency domain with wave vector $\vec{k}$ and angular frequency ω.

$$\mathrm{F}(\vec{k},\omega)=\mathcal{F}\big(\mathrm{f}(\mathrm{r},\mathrm{t})\big) = \iint_{-\infty}^{\infty} f(r,t)e^{i(\vec{k}\cdot r-\omega t)}drdt \quad (2.\ 34)$$

Fourier transform of equation (2. 33) shows that the general solution for the electric field is:

$$\vec{E}(r,t) = \int_{-\infty}^{\infty} E_0(\omega)\, e^{i(\omega t-\vec{k}\cdot r)}d\omega \quad (2.\ 35)$$

with dispersion relation $\vec{k}$ as follows.

$$\vec{k}(\omega) = \sqrt{\omega^2\mu_0\epsilon_0\tilde{\epsilon}(\omega)} \quad (2.\ 36)$$

When light passes through a medium (not in a vacuum), the velocity of EM wave propagation can be retarded, and the intensity of EM wave can be decreased. It is because of refraction and absorption in a medium, respectively. The attenuation of EM wave is related with the imaginary part of the complex refractive index

$$\tilde{n}(\omega) \equiv n(\omega) - i\kappa(\omega) \equiv \frac{\left|\vec{k}(\omega)\right|c}{\omega} = \sqrt{\tilde{\epsilon}(\omega)} \quad (2.37)$$

where n is the refractive index and indicates the phase velocity, while κ is the extinction coefficient related with attenuation.

Complex dielectric constant with free charges

In this thesis, we consider the system of investigation as an electrolyte solution that contains ions, free charges in the system. In case of a system contains extra free charges, conductivity term should be considered as driving sources in the Maxwell equations. Then (d) in equation (2. 31) is modified as follows.

$$\vec{\nabla} \times \frac{\vec{B}}{\mu_0} - \frac{\partial \vec{D}}{\partial t} = \mu_0 \sigma \vec{E} \tag{2. 2}$$

And this modification leads EM wave has dispersion relation $\vec{k}(\omega)$ including conductivity term.

$$\vec{k}(\omega) = \sqrt{\omega^2 \mu_0 \epsilon_0 \tilde{\epsilon}(\omega) - i\omega\mu_0\sigma} \tag{2. 3}$$

Above dispersion relation is basically same as we change $\tilde{\epsilon}(\omega)$ in equation (2.36) as $\tilde{\epsilon}(\omega) + \frac{\sigma}{i\omega\epsilon_0}$. This means additional conductivity term in dielectric constant is in the imaginary part, increasing absorption due to free charges is called “ohmic loss.”

Observing the above macroscopic optical properties by using EM wave, for example, reflection, transmission, and attenuated total reflection, we can obtain information about how target system interacts with EM wave through measuring complex refractive index or equivalently complex dielectric constant.

Dielectric relaxation

The dielectric displacement $\vec{D}(\omega)$ can be written as equation (2. 32). In macroscopic viewpoint $\epsilon_0\vec{E}$ is independent of system, while $\vec{P}$ is the polarization term due to the effect of an electric field on system. If we look at polarization in a microscopic view, it can be explained as the sum of orientational polarization and induced polarization.

$$\vec{P} = \vec{P}_{\mu} + \vec{P}_{\alpha} = \sum_i \rho_i < \vec{\mu}_i > = \sum_i \rho_i \alpha_i \left(\vec{E}\right)_i \qquad (2.\ 40)$$

Here, first term is sum of orientational polarization originated from molecular dipoles with permanent dipole moment $\vec{\mu}_i$ of species i. Above summation means that orientational polarization of molecular dipoles of species i is described as number density ρ_i times average dipole moment $< \vec{\mu}_i >$ in the applied electric field against thermal fluctuation in the system. Second term is the induced polarization in the system due to local field $\left(\vec{E}\right)_i$ exerted at exact position of the atom or molecule.

Orientational polarization in a polar molecule such as water has pico- to nanosecond time scale dynamics, corresponding to GHz-THz frequency domain. Due to orientational polarization caused by the reorientation motion of dipoles in the applied electric field against thermal fluctuation in liquid, broad dielectric dispersion is observed in the GHz-THz frequency regime. The induced polarization is in much higher frequency above microwave region. Typically, intramolecular dynamics of the medium can be obtained from induced polarization and its frequency dependence. For example, information about intramolecular dynamics usually can be obtained by induced polarization in the infrared (IR) frequency domain, and electron dynamics can

be obtained by induced polarization in the ultraviolet (UV) range.

Because two different polarization have distinct time scales, both effects can be separated and independent variable in frequency domain. In the high-frequency limit, induced polarization effect only exists because orientational polarization averages out to zero in the external electric field's fast oscillation. Therefore, orientational polarization and induced polarization can be written as:

$$\begin{aligned} \vec{P}_{\mu} &= \epsilon_0(\tilde{\epsilon} - \epsilon_{\infty})\vec{E} \\ \vec{P}_{\alpha} &= \epsilon_0(\epsilon_{\infty} - 1)\vec{E} \end{aligned} \tag{2. 41}$$

where ϵ_{∞} is polarization decrement after orientational polarization frequency domain as called permittivity for infinite frequencies usually obtained from the extrapolation beyond microwave region.

Debye relaxation for dielectric relaxation response (macroscopic)

Dielectric relaxation from are usually described by model functions. The most widely used model to describe the dielectric spectrum of a liquid is the Debye model. The Debye model explains the dielectric spectrum through a polarization response induced proportionally by an external electric field. Frist, Debye model can be reviewed in terms of macroscopic relaxation point of view. As shown in Fig 2. 7, we can set the system of macroscopic polarization relaxation follows exponential decay. In this system total polarization of system exponentially decreases after external applied field. When oscillating field is applied, macroscopic rate equation based on

$$\frac{dP_2}{dt} = \frac{P - P_1 - P_2}{\tau} \tag{2. 42}$$

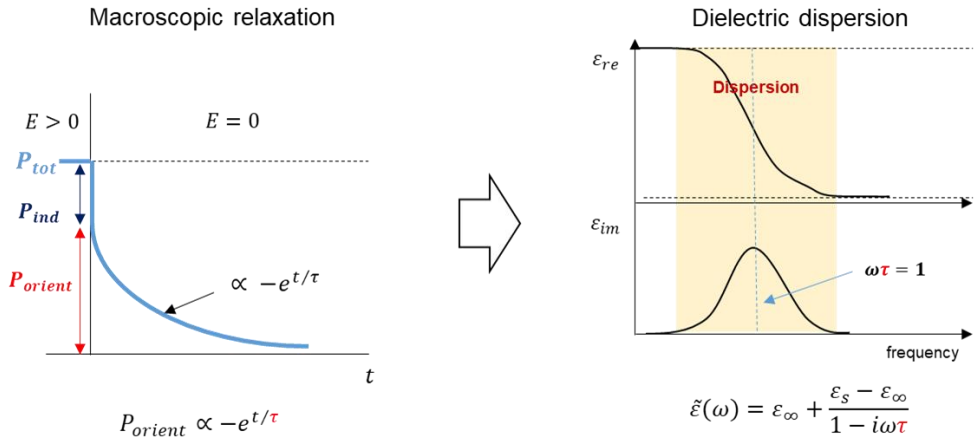

Figure 2. 7 Macroscopic relaxation and resultant dielectric dispersion

exponential relaxation of total dipole moment can be written as equation (2. 42) where P is total dipole moment, P_1 is induced dipole moment and P_2 is permanent dipole moment.

The oscillating field and polarization can be written using dielectric properties of the polar molecule.

$$\begin{aligned} E &= E_0 exp(-j\omega t) \\ P &= \varepsilon_0(\varepsilon_s - 1)E \\ P_1 &= \varepsilon_0(\varepsilon_\infty - 1)E \\ P_2 &= A\exp(-j\omega t) \end{aligned} \tag{2. 43}$$

By substituting (2. 43) to rate equation (2. 42) and rearrange into P, we can reach results based on the Debye model's assumption; orientational polarization due to external field decreases exponentially with time in the absence of field.

$$\varepsilon_r = \varepsilon_\infty + \frac{\varepsilon_s - \varepsilon_\infty}{1 - j\omega\tau} \quad (2.44)$$

Through the above results, it can be seen that the dielectric dispersion measured in the GHz-THz frequency region is originated from the relaxation of total dipole polarization, and its characteristic timescale can be obtained from τ by Debye model fitting of dielectric spectrum in frequency domain.

Debye model for reorientation dynamics (microscopic)

In the above section, the debye model was derived macroscopically through a simple assumption that the response of total polarization to the external electric field decays exponentially. Now, we will look at how dielectric relaxation process is microscopically originated by derive Debye model from individual molecular dipole.

In 1987, Drude find "Anomalous dispersion" from dielectric spectrum of polar liquid in GHz frequency domain. Later, P. Debye theoretically explained this dispersion originated from the reorientation motion of molecules due to collision. In the liquid state, molecules are continuously collision each other and cause random motion in the translational and rotational degree of freedom. In Debye theory, rotational Brownian motion. As shown in Fig. 2. 8, to explain the rotational reorientation motion, it is assumed that an externally vibrating electric field is applied to the system at a constant temperature. At this time, all dipole moments in the system can be mapped to sphere, size of the dipole moment, and the distribution of dipole moments in the solid angle $\mathrm{d}\Omega$ can be expressed as $\mathrm{f}\,\mathrm{d}\Omega$. random motion is assumed to be a small step diffusion, which leads to Dipole moment distribution in solid angle $\mathrm{d}\Omega$ follows rate equation (2. 45) in time step $\delta\mathrm{t}$.

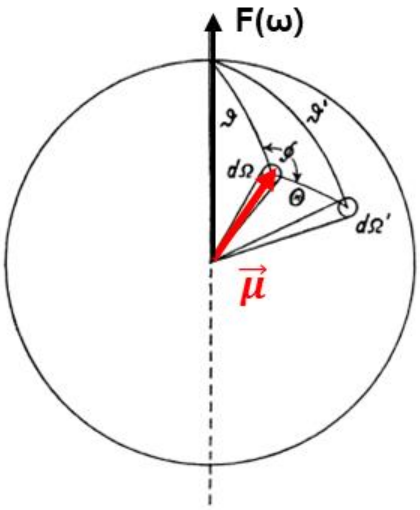

Figure 2. 8 Dipole moment sphere: $\vec{\boldsymbol{\mu}}$ is dipole moment, F is direction of external electric field and $\mathbf{d\Omega}$ is solid angle

$$\delta t \frac{\partial f}{\partial t} d\Omega = \Delta_1 + \Delta_2 \qquad (2.45)$$

Δ_1 is orientation motion caused by external electric field F and Δ_2 is from random Brownian motion in rotational degree of freedom.

Contribution from dipole moment distribution by Brownian motion Δ_2 can be decomposed to inflow term and outflow term as bellows.

$$\Delta_2 = -f d\Omega + \int f' d\Omega' W d\Omega \qquad (2.46)$$

$Wd\Omega$ is the probability to find dipole moment originally in direction of solid angle $d\Omega$ at solid angle $d\Omega'$ after δt left. Also, above f' can be expressed using Taylor expansion using solid angle θ.

$$f' = f + (\vartheta' - \vartheta)\frac{\partial f}{\partial \vartheta} + \frac{(\vartheta' - \vartheta)^2}{2}\frac{\partial^2 f}{\partial \vartheta^2} + \cdots \qquad (2.\ 47)$$

Based on small step diffusion assumption we can ignore higher order term greater than 3rd order. Substituting the equation (2. 47) into (2. 46) and arranging it using spherical trigonometry, it can be calculated as follows.

$$\Delta_2 = d\Omega \frac{\overline{\theta^2}}{4}\left[\frac{cos\vartheta}{sin\vartheta}\frac{\partial f}{\partial \vartheta} + \frac{\partial^2 f}{\partial \vartheta^2}\right] \qquad (2.\ 48)$$

This model describes rotational reorientation as rotational diffusion motion through Brownian motion, equation (2. 48) can be written alternaively using Einstein-Smoluchowski relation.

$$\Delta_2 = d\Omega\delta t \frac{kT}{\zeta}\left[\frac{cos\vartheta}{sin\vartheta}\frac{\partial f}{\partial \vartheta} + \frac{\partial^2 f}{\partial \vartheta^2}\right] \qquad (2.\ 49)$$

For the dipole moment variation due to external field Δ_1 can be calculated from continuous equation. When applied field reorient dipole moment to its direction there exist frictional force to hinder the free rotation motion and this frictional force is assumed to same in small step diffusion. By using above concept we can obtain Δ_1 as follows.

$$\Delta_1 = \frac{\partial}{\partial \vartheta}\left(f\frac{\mu F sin\vartheta}{\zeta}\delta t sin\vartheta\right) \qquad (2.\ 50)$$

Combining equation (2. 49) and (2. 50) together we can get rate equation of dipole moment in solid angle dΩ.

$$\frac{\partial f}{\partial t} = \frac{1}{\zeta sin\vartheta}\frac{\partial}{\partial \vartheta}\left[sin\vartheta\left(kT\frac{\partial f}{\partial \vartheta} + f\mu F sin^2\vartheta\right)\right] \quad (2.\ 51)$$

And this rate equation has Ansatz form as bellows.

$$f = A\cdot\left(1 + \frac{1}{1 - i\omega\tau'}\frac{\mu F cos\theta}{kT}\right) \quad (2.\ 52)$$

Now using above Ansatz form for dipole distribution considering molecular reorientation motion due to thermal fluctuation when external electric field is applied as shown in Fig. 2. 9.

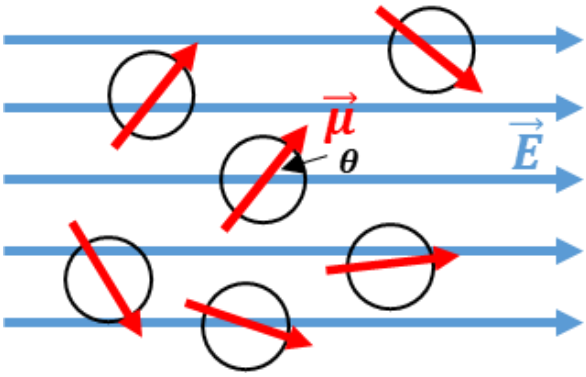

Figure 2. 8 Permanent dipole and applied field in polar molecule medium

The average orientation polarization is can be obtained by using Ansatz and spherical integration. Except for θ angle between applied field and dipole moment, integrate to zero because of spherical symmetry.

$$P_{orient} = N\mu\langle cos\theta\rangle = \frac{N\mu^2 F}{3kT(1 - i\omega\tau')} \quad (2.\ 53)$$

Orientational polarization can be written in local field F when external electric field E is applied to the system, as in the above equation (2. 53)

This local field F can be obtained based on assumption that system is homogenous medium and negligible interaction between individual molecule in the system.

$$F = E + \frac{P}{3\varepsilon_0} = \left(\frac{\varepsilon_r + 2}{3}\right) E \tag{2. 54}$$

Using above equation (2. 54) macroscopic dielectric dispersion ε_r can be written in microscopic dipole polarization considering reorientation dynamics of polar molecule as (2. 55)

$$\frac{\varepsilon_r - 1}{\varepsilon_r + 2} = \frac{N}{3\varepsilon_0}\left(\alpha + \frac{\mu^2}{3kT(1 - i\omega\tau')}\right) \tag{2. 55}$$

Using low frequency ($\varepsilon_r = \varepsilon_s$: static permittivity) and high frequency limit ($\varepsilon_r = \varepsilon_\infty$: high frequency permittivity limit), the well-known Debye relation for dielectric dispersion can be obtained as (2. 56)

$$\varepsilon_r = \varepsilon_\infty + \frac{\varepsilon_s - \varepsilon_\infty}{1 - i\omega\tau} \tag{2. 56}$$

In the Debye model, it was confirmed microscopically that dielectric dispersion appeared due to rotational diffusion of dipole moment due to thermal fluctuation when the external field was applied. Also, macroscopically, it can be confirmed that orientational polarization responds to an external electric field, resulting in Debye relaxation. Therefore, connecting the above two facts, Debye relaxation can be seen as a response to the external electric field of the system dipole moment by molecular-level reorientation dynamics.

2.2.2 Experimental techniques

Dielectric response measurement using Vector Network Analyzer

Dielectric relaxation spectroscopy measures the frequency-dependent complex dielectric constants of the system. Typically, dielectric relaxation spectra are given by measuring optical properties such as refractive index and extinction coefficient using such as reflectometry, transmission measurement, and attenuated total reflection measurement. One of the most widely used methods is reflectometry using Vector Network Analyzer. This method measures the scattering parameter of the sample over a target frequency range, and this scattering parameter can be converted to a dielectric constant using the bilinear model. Basically, VNA measures incident, reflected and transmitted waves traveling along transmission lines.

This method can generally be thought of as the same phenomenon as reflection and transmission when light passes through a medium as shown in Fig. 2. 10. In this scheme, measuring the accurate reflectance (ratio between the reflected signal and the incident signal) or transmittance (ratio between the transmitted signal and the incident signal) is main objective.

We measured the complex dielectric constant of aqueous electrolyte solution using this vector network analyzer and open-ended coaxial probe. The frequency range that can be measured varies according to the vector network analyzer's structure transporting the RF frequency as shown in Fig. 2. 11. Since the dielectric relaxation of water molecules in the aqueous electrolyte solution is 20 GHz as the center frequency in the GHz range, an open-ended coaxial probe was used as shown in Fig. 2. 12.

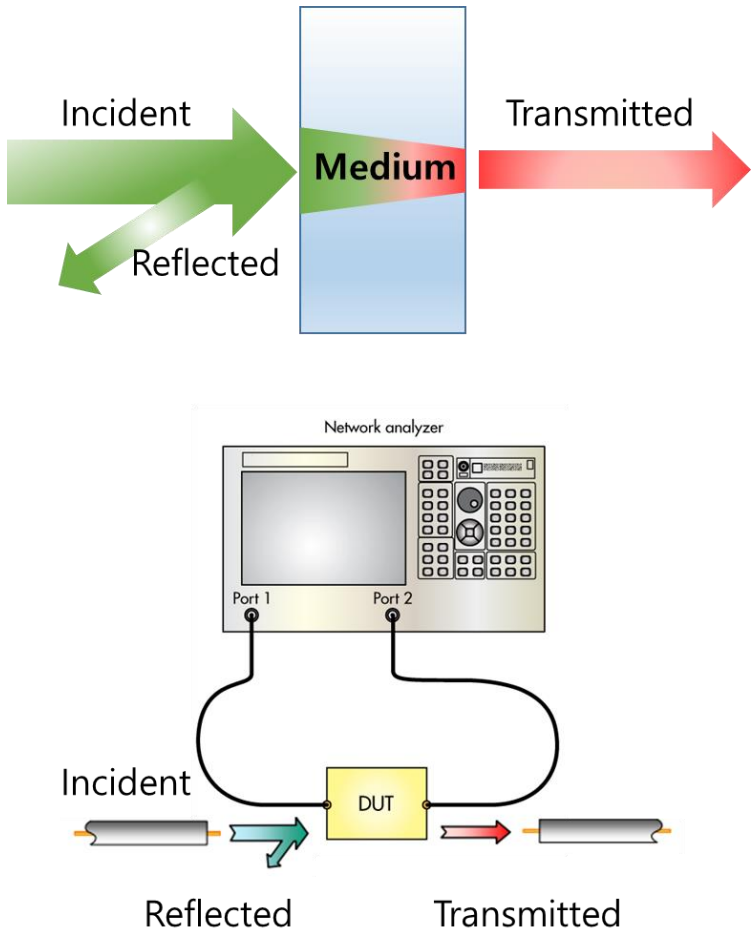

Figure 2. 10 Vector Network Analyzer in terms of light-wave analogy

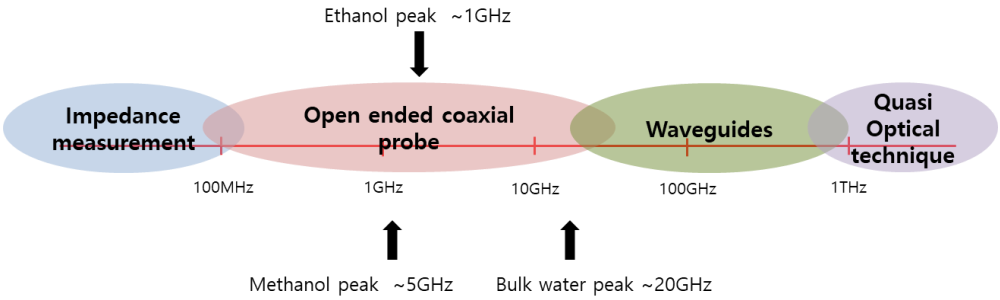

Figure 2. 11 Measurement method using VNA depend on frequency range

Open-ended coaxial probe method

The key elements of measuring the dielectric constant of a liquid using an open-ended coaxial probe are described in Fig 2. 12. One end of the coaxial line is connected to an open-ended coaxial probe immersed in the material under test (MUT) to transport radio frequency signals from the VNA to the MUT.

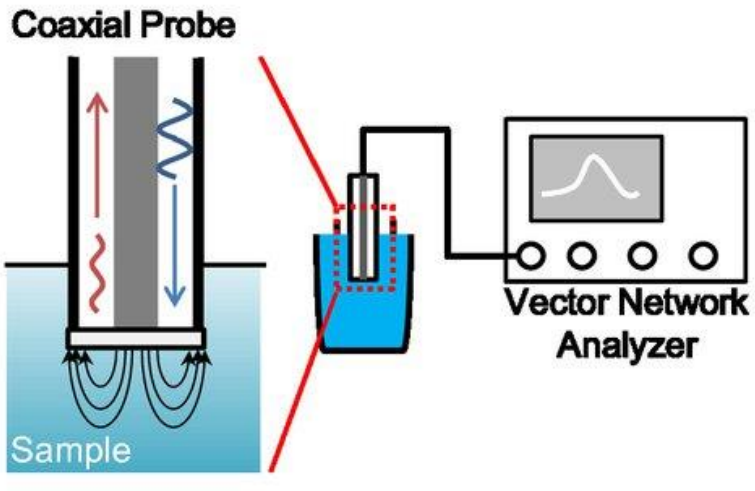

Figure 2. 12 Schematic of the open-ended coaxial probe for liquid sample

As shown in the Fig. 2. 12, since the electric field is fringed on the sample at the end of the open-ended coaxial probe, the interaction between the sample and the electric field is reflected in the reflected signal. This coaxial probe at the sample-probe reflection surface can be understood as a simplified capacitor model.

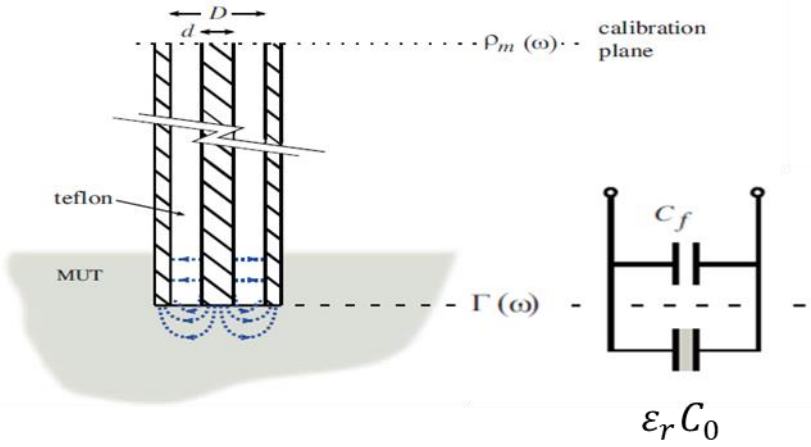

Figure 2. 13 Capacitor model for open-ended coaxial probe

As shown in Fig. 2. 13, the electric field fringed into coaxial probe is described as electric field in capacitor of capacitance C_f and the electric field fringed into the sample is described as electric field in capacitor of capacitance of $\varepsilon_r C_0$ where ε_r is the dielectric constant of MUT. Here, admittance for the model capacitor is given as equation (2. 57).

$$Y_L(\omega) = j\omega(C_f + \varepsilon_r C_0)$$
$$\varepsilon_r = \varepsilon' - j\varepsilon''$$
$$Y_L = \frac{1}{Z_L}, \qquad Z = \frac{1}{j\omega C} \tag{2. 57}$$

Then, admittance y_x between unknown sample and probe can be written as bilinear relation in terms of admittance y_s between known sample and probe and reflectance ρ measured by reflection signal from both sample as follows.

$$y_x - y_s = \frac{A\rho - C}{1 - B\rho} \tag{2. 58}$$

Combining equation (2. 57) and (2. 58) the recast in terms of the dielectric constant of the sample, we can obtain the dielectric constant of the unknown sample by the bilinear form of reflectance measured by VNA.

$$\varepsilon_x^* = \frac{A^*\rho_x^* + C}{1 - B^*\rho_x^*} \tag{2. 59}$$

The A,B and C parameter from the bilinear model is given by relating well-known dielectric constant such as air, metal and water and reflectance measured by VNA.

Experimental setup

The complex dielectric spectra of 1024 points measured at equally spaced in log scale over the frequency range from 0.01 GHz to 110 GHz, were obtained by open-ended coaxial probe (850070E, Keysight Inc.) connected to Anritsu model MS4647B vector network analyzer (VNA) with 3739C broadband test set. Open-ended coaxial probe was immersed into sample solution at 25 ± 0.1℃. Temperature was controlled by a Finepcr ALB 6400 model. We used above bilinear model [50, 51] which is widely used in open-ended coaxial probe for determining dielectric constant of liquid sample. All spectra were obtained from measured ρ_x^* using above equation (2. 59). Three coefficients were extracted by relating dielectric constant $\varepsilon_s^*$and measured S parameter ρ_s^* with three independent calibrations (with deionized water,

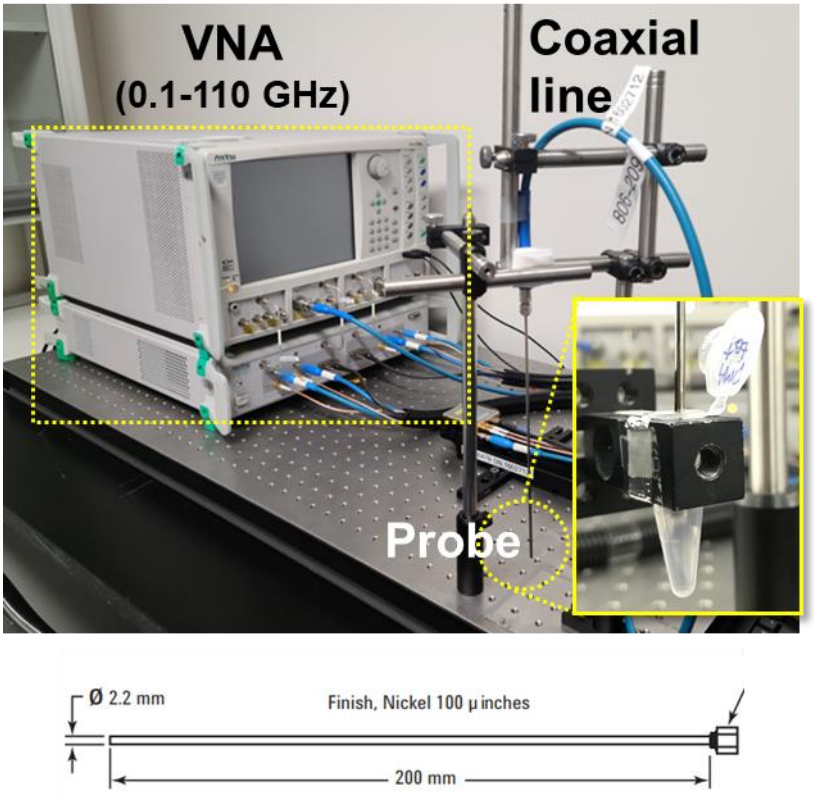

Figure 2. 14 Experimental setup for 0.1-110 GHz dielectric measurement by using VNA and open-ended coaxial probe

dimethyl sulfoxide(≥99.9%) and 2-propanol(≥99.5%) from Sigma) [52, 53]. In order to check the accuracy of the dielectric constant measured through the above experimental setup, an experiment was performed on a well-known water-ethanol mixture, which was consistent with the results of the previous study shown in Fig. 2. 15.

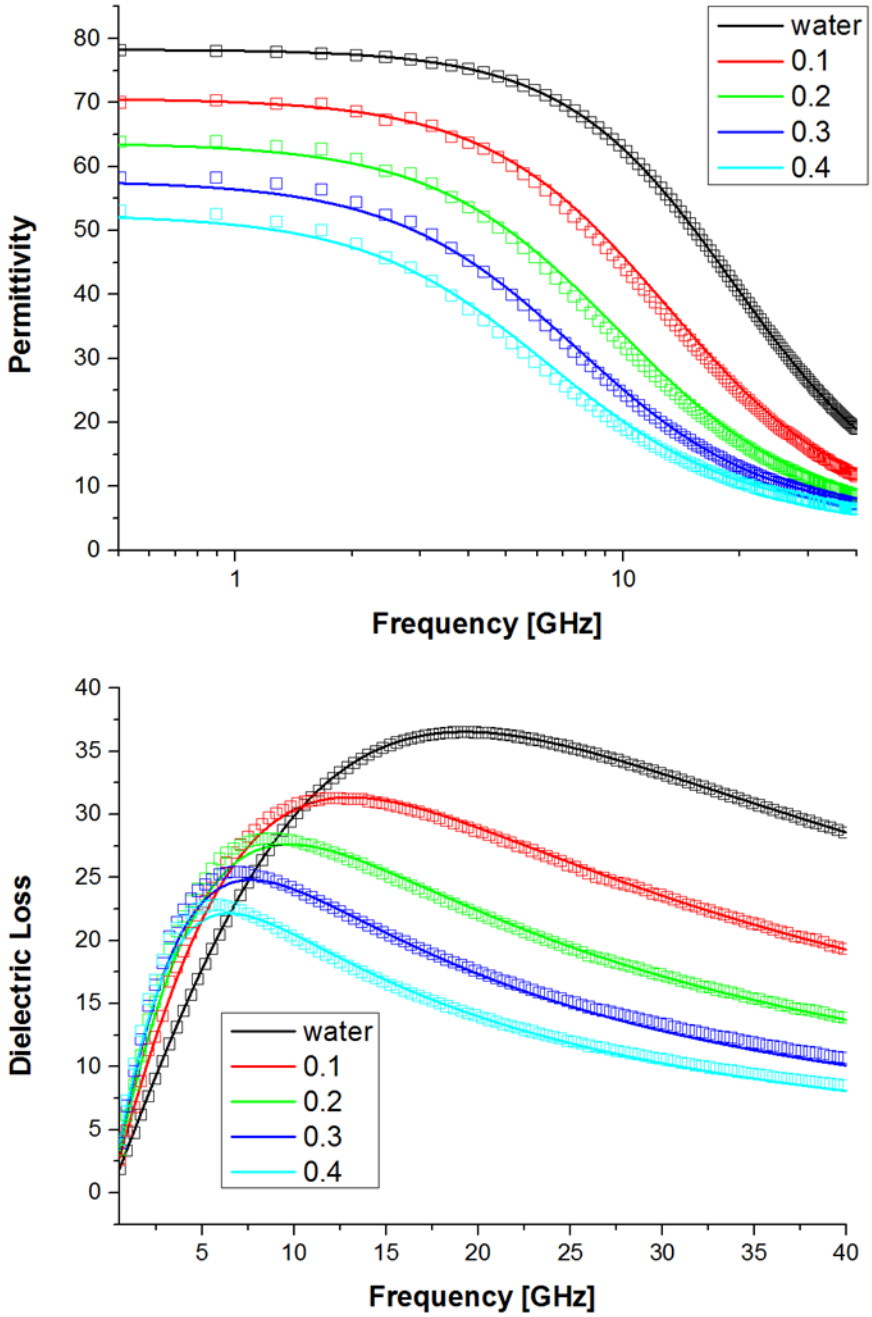

Figure 2. 15 Dielectric measurement of Water-ethanol mixture by increasing ratio (ethanol:water) line reference [54] and dots our experiment.

Sample preparation

Aqueous $MgCl_2$ solutions were prepared by dissolving $MgCl_2$ powder in deionized water. $MgCl_2$ powder with a purity of over 98% was purchased from Sigma and used without further purification process. High purity deionized water with electrical resistance of 18.2MΩ·cm was prepared by Milli-Q systems. Solutions were prepared by first measuring the weight of $MgCl_2$ powder using a balance with a precision of 0.1mg and dissolving it in deionized water by measuring concentration volumetrically (mol/kg).

Supporting measurements: Densimetry

To calculate concentration of electrolyte solution accurately, solution density was measured under accuracy of 0.001g/cm^3 using vibrating-tube densimeter Anton Paar DMA 500 [55]. The instrument was calibrated using deionized water with electrical resistance of 18.2MΩ·cm was prepared by Milli-Q systems. Temperature was controlled at 25 ℃ by a Finepcr ALB 6400 model with accuracy of ± 0.1℃.

Supporting measurements: Conductivity

The typical complex dielectric spectra of electrolyte solution can be explained by following equation.

$$\eta^*(\nu) = \varepsilon^*(\nu) + \eta_k^*(\nu) = \varepsilon^*(\nu) + \frac{\kappa}{2\pi\nu\varepsilon_0} \qquad (2.60)$$

The $\varepsilon^*(\nu)$ is a term comes from fluctuations of the total dipole moment of aqueous solutions with amplitude and time constant.. The $\eta_k^*(\nu)$ term is a dielectric loss due to Ohmic loss because aqueous electrolytes solution has electrical conductivity, κ. In order to obtain dielectric relaxation spectra

$\varepsilon^*(\nu)$ from dipole fluctuation and kinetic depolarization correction for calculating hydration number, conductivity of solution is independently measured by using conductivity meter from mettler Toledo S230.

Chapter 3

Solvation Structure

3.1 Pair-correlation function

The pair correlation function is usually used to explain the intermolecular structure of system. This quantity can be compared directly with the structure factor measured by X-ray scattering or neutron scattering. The pair correlation function describes how the particle of interest is distributed with respect to reference particle. For example, one of the most widely used pair correlation functions, the radial distribution function of a uniformly distributed ideal gas has a constant value at all distances because it has no internal structure or intermolecular structure. However, for a solid structure where molecules are repeatedly distributed with specific spacing (lattice structure), the pair correlation function has sharp peak features at the distance particles are highly located and is almost zero at distances where particles are rarely located. Also, liquid structure can be investigated using

radial distribution function because it has short-range structure from angstrom to nanometer range.

In this thesis, radial distribution function (RDF) is used to observe internal structure of electrolyte solution such as ion-water structure (solvation structure) or water-water structure. The radial distribution function g(r) gives the probability of finding a particle in the distance r from reference atom or molecule. And the quantity g(r) is defined as ratio between local density $\rho(r)$ and overall density of atoms ρ_0 as shown in Fig. 3. 1.

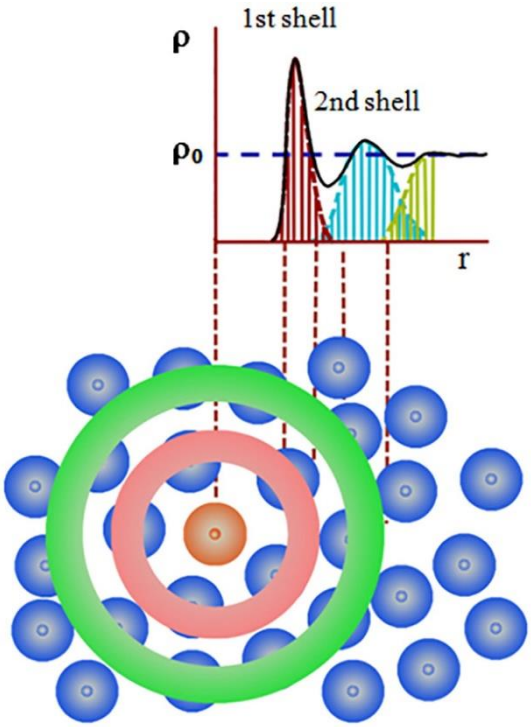

Figure 3. 1 The illustration of radial distribution function

By the definition we can calculate average atom number that lie in a spherical shell of radius r and thickness dr by integrating g(r) as follows.

$$\int g(r)4\pi r^2 dr \tag{3. 1}$$

3.2 Solvation structure around ion

Hydration shell structure of Mg^{2+} ion

For example, Mg^{2+} - Oxygen radial distribution function in isolated Mg^{2+} ion simulation is can be obtained as shown in Fig. 3. 2. The first thing we can look at is that we can see peaks around 2.1 Å and 4.3 Å. This peak means that oxygen in water is found with a high probability at a specific location near Mg, and it can be seen that water forms two major hydration shells near Mg.

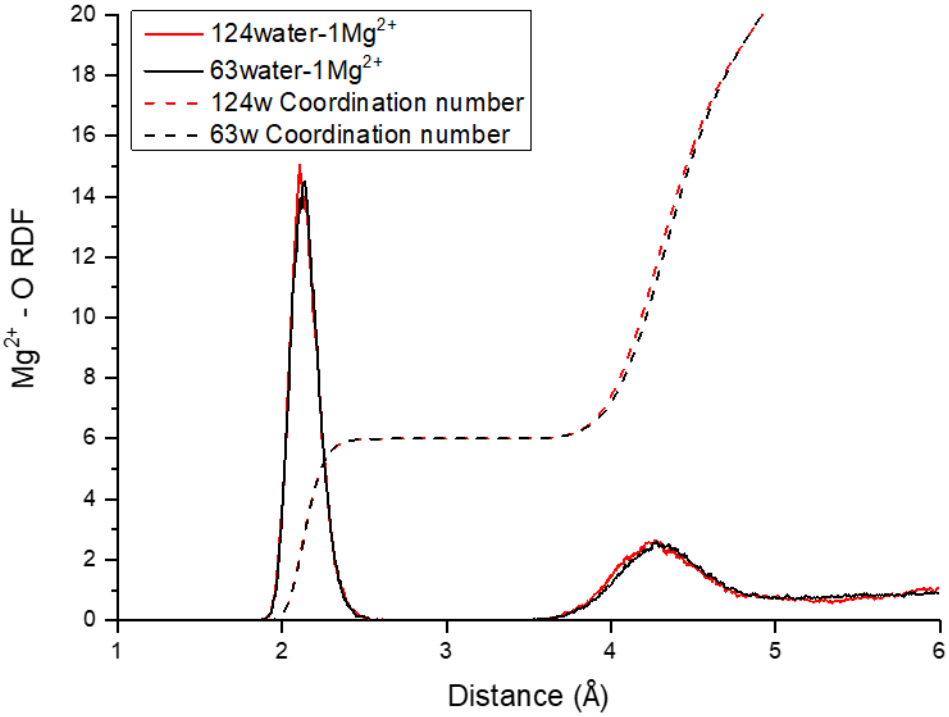

Figure 3. 2 Mg^{2+} - Oxygen RDF of isolated Mg^{2+} ion simulation

The second information that can be obtained is information on how many water molecules are contained in this hydration shell. As shown above, one can calculate the coordination number in a specific hydration shell near ions by integrating g(r), which is 6 in the first hydration shell and 12 in the second hydration shell. Also, beyond the second hydration shell, it can be seen that the RDF converges to 1, which means that the intermolecular structure has no significant long-range order beyond the second hydration shell. Finally, it can also be found that the structure around isolated Mg^{2+} does not change according to the simulation size by comparing the isolated Mg^{2+} in 63 water molecules and the isolated Mg^{2+} situation in 124 water molecules.

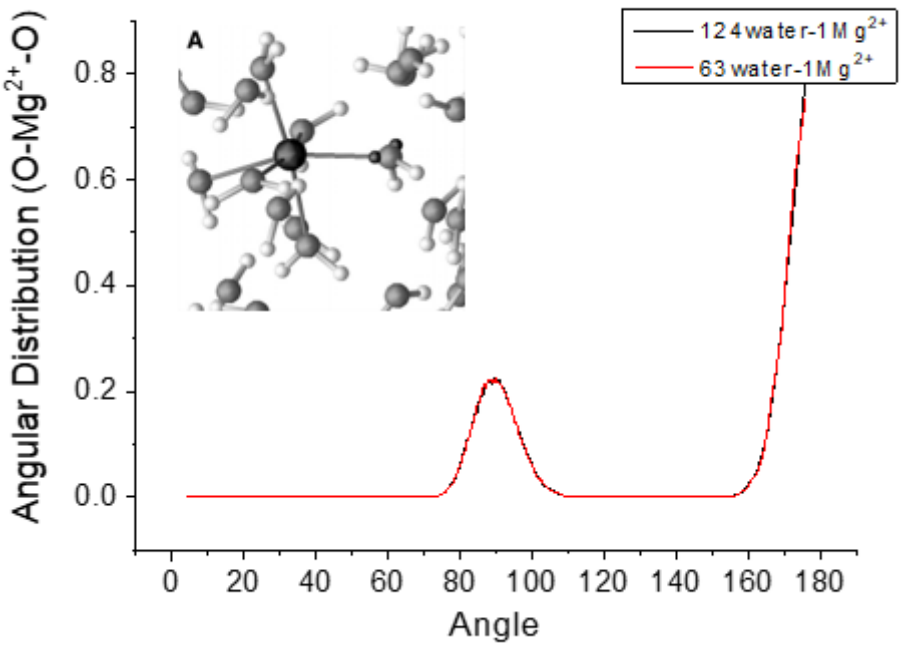

Figure 3. 3 Angular distribution function of angle $\angle \mathbf{OMg^{2+}O}$ and configuration of first hydration shell water

Fig. 3. 3 is the angle distribution between $\angle \mathbf{OMg^{2+}O}$, and the peak can be found at about 90 degrees and 180 degrees. Combining RDF and ADF results shows that six water molecules are distributed with Mg ions forming an angle of 90 degrees and 180 degrees. The structure that satisfies this is an octahedral arrangement, which is experimentally observed.

Ion-water radial distribution in electrolyte solution

Experimentally, the first hydration shell Mg-O distance is 2.09±0.04 Å, the average over available diffraction data [57], and the second shell is in the range of 4.1–4.2 Å [58]. Interatomic Mg-water distances can be determined from the ab initio MD simulations through the generation of the Mg-O radial distribution functions (RDF), g(r), which represent the probability, relative to a random distribution, of finding Mg and O separated by distance r as shown in Fig 3. 4. Key structural properties of the hydration shell of Mg^{2+} obtained from the RDFs (positions, amplitudes, and average coordination number of the first and second hydration shells) are listed Table 3. 1. In all solutions, the magnesium ion is characterized by a well defined peak at 2.1 Å, which is in excellent agreement with the experimental ranges of equilibrium Mg-O distances (2.09±0.04 Å) [57], and a second widely distributed second shell in the range of 4.1–4.3 Å. The differences between the Mg-O and Cl-O RDF profiles (inset of Figure 3. 4) reflect the rigidity of the hydration shell of Mg^{2+} and the fast exchange dynamics of the water molecules coordinated to Cl^- : using the "direct" method by Hofer et al. to characterize the dynamics of ionic solvation shell [59], between 160 and 330 water exchanges every ten ps, depending on the solution concentration and speciation, were accounted around each chlorine ion, to which corresponds a sub-ps mean residence time of waters in the coordination shell of Cl^- . In comparison, the intensity of the Mg-O RDF of the MgCl2 solutions is zero be-

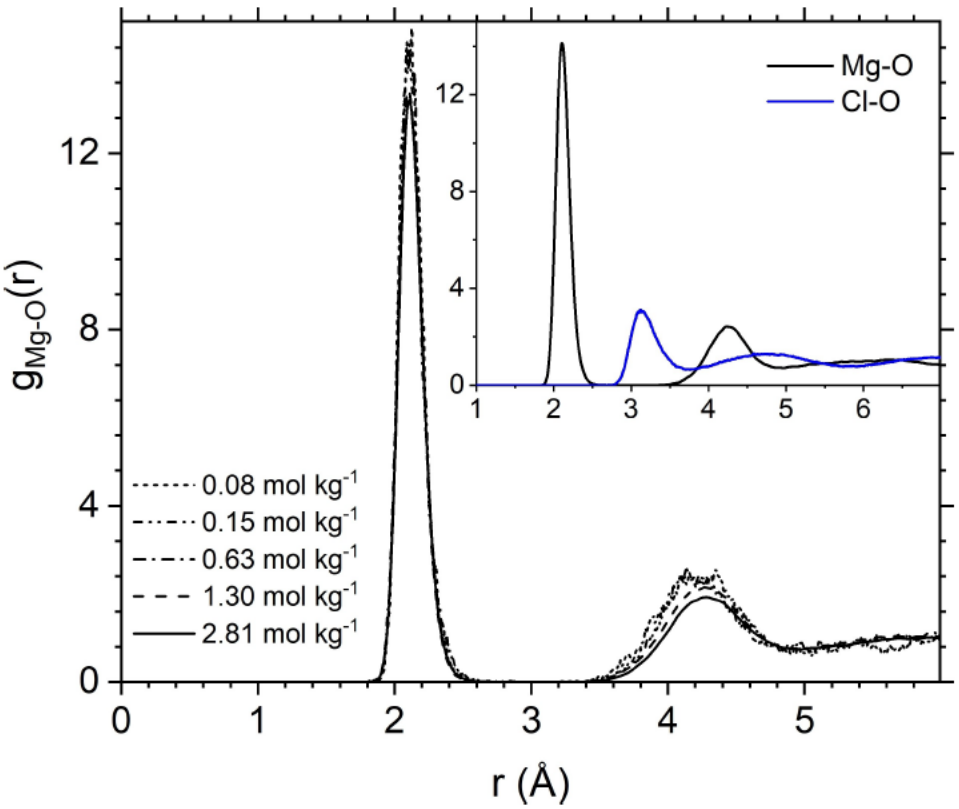

Figure 3. 4 Mg-O radial distribution functions obtained from ab initio MD simulations of aqueous MgCl2 solutions. Inset: Comparison of the Mg-O and Cl-O RDFs obtained from the 0.63 molkg^{-1} aqueous $MgCl_2$ solution

System	Concentration	r_1^{max}	$g(r_1^{max})$	r_2^{max}	$g(r_2^{max})$	CN_1	CN_2
2	0.08	2.11	14.7	4.35	2.6	6.0	15.4
3	0.15	2.11	14.0	4.14	2.6	6.0	14.4
4	0.63	2.10	15.3	4.23	2.4	6.0	13.8
5	0.63	2.12	14.3	4.21	2.4	5.8	13.4
6	1.30	2.10	15.6	4.20	2.4	6.0	13.8
7	1.30	2.12	13.5	4.27	2.2	5.4	12.5
8	2.81	2.12	13.4	4.30	1.9	5.1	10.5
Experiment		2.09 ± 0.04		4.1–4.2		6.0	12.0

Table 3. 1 Structural properties of the magnesium–water radial distribution functions obtained from the *ab initio* MD simulations of $MgCl_2$ solutions. The positions (r^{max}) and amplitudes [$g(r^{max})$] of first and second peaks, the average coordination number of the first (CN_1) and second (CN_2) hydration shells are compared with available experimental data. Distances in Angstrom. The system number is same as Table 2. 2

tween the first and second peak because no water exchanges occur around Mg^{2+}. The slow kinetics of Mg-dehydration originates from the high free energy barrier to remove a single water molecule from the first hydration shell of Mg^{2+}, as revealed by previous classical MD simulations of hydrated Mg^{2+} (isolated ion, no counterion) [60–63] and $MgCl_2$ [64]. A recent transition path sampling MD study of the kinetic pathways in the first hydration shell of magnesium concluded that the time spent by water molecules in the first hydration shell of Mg^{2+} is 40 ms [65].

3.3 Influence of ion on the structural properties of water

Ion effect on water structure

The oxygen-oxygen (O-O) radial distributions (RDF) for pure water and aqueous $MgCl_2$ solution, with and without contact ion pairs, are reported in Figure 3. 5. The first and second peak are positioned at 2.74 Å and 4.5 Å, which correspond to the average O-O distance of two hydrogen bonded water molecules and of two water molecules hydrogen bonding to the same water molecule, respectively. The O-O RDF profiles show a progressive rise in the first minimum and lowering of the first and second maxima with increasing concentration, this being associated with a decreasing order in the system. The influence of $MgCl_2$ on the water structure is noticeable even at low concentrations (0.15 mol kg^{-1}). On the contrary, Gaiduk et al. reported ab initio MD simulations of NaCl (aq) where the O-O RDF was very close that of pure water, even at much higher concentrations (0.9 mol dm^{-3}) [66]. Similarly, classical MD simulations of KCl (aq) and CsCl (aq) with concentrations ranging from 0.11 to 1.90 mol kg^{-1} did not display significant effects on the water structure [67].

Hydrogen bond structure of water

As can be seen in Fig 3. 6, water forms a hydrogen bond with the surrounding water molecules, and hydrogen bond is one of the key elements in understanding water, as we have seen in the introduction. In the simulation, the hydrogen bond can be geometrically defined using the distance between molecules and the angle between molecules or energetically defined. In this theses, we have used geometrical criteria because its simplicity and robustness.

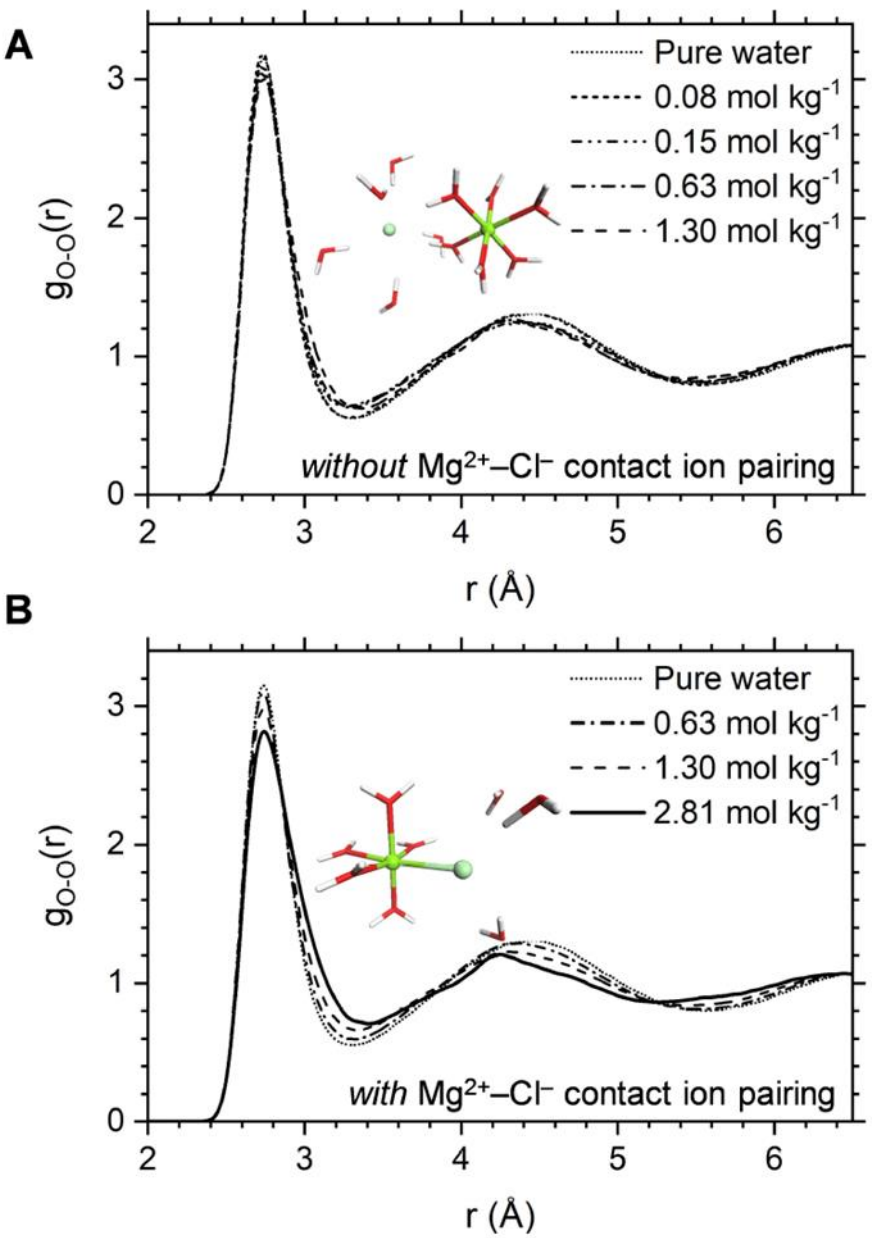

Figure 3. 5 Oxygen-oxygen radial distribution function, $g_{O\text{-}O}(r)$, for aqueous MgCl2solutions (A) without Mg^{2+}-Cl^{-}contact ion pairing (B) with Mg^{2+}-Cl^{-} contact ion pairing.

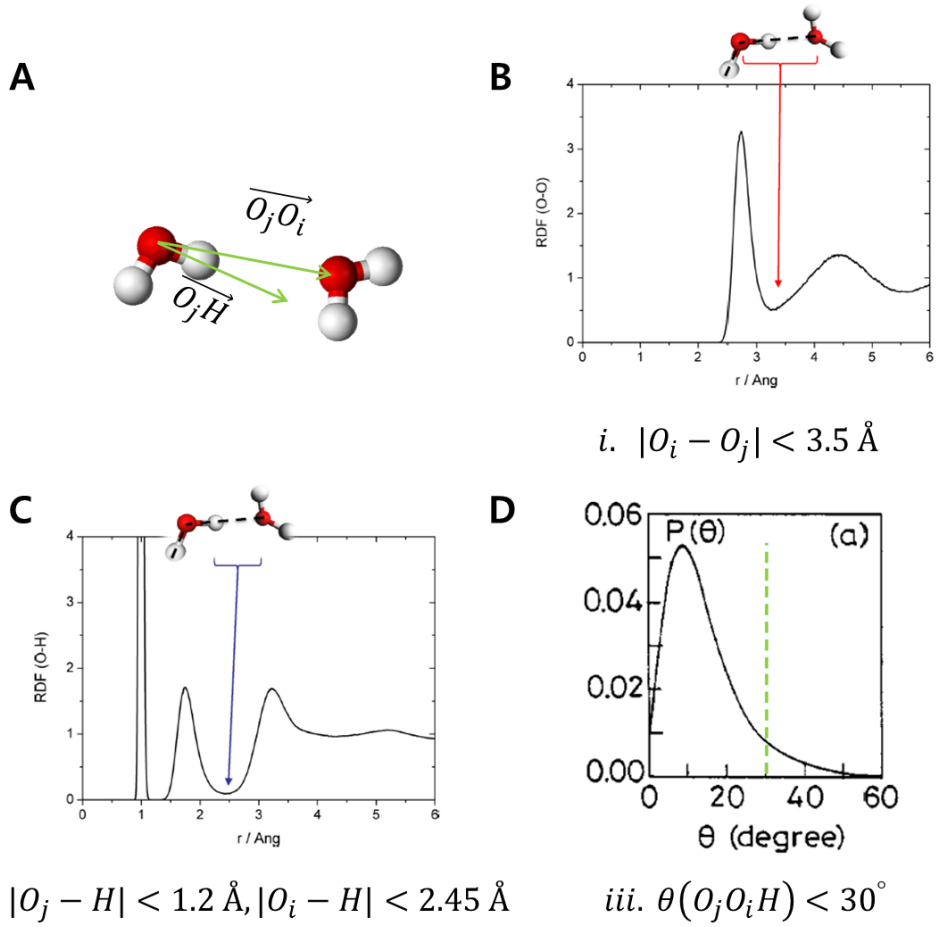

$i.\ |O_i - O_j| < 3.5$ Å

$ii.\ |O_j - H| < 1.2$ Å, $|O_i - H| < 2.45$ Å

$iii.\ \theta(O_jO_iH) < 30^{\circ}$

Figure 3. 6 Hydrogen bonded water molecules (A) and geometrical hydrogen bond criteria of (B) O-O distance (C) O-H distance (D) Angle between O-O axis and OH arm

As suggested by Chandra et al. [68], We have used a set of geometric criteria where an HB between two water molecules exists if the following distance and angular criteria are satisfied: O-O distance is less than 3.5 Å, O-H distance is less than 2.5 Å, and the O-O-H angle is no more than 30° as shown in Fig. 3. 6. Earlier studies considered these geometrical criteria to characterize the

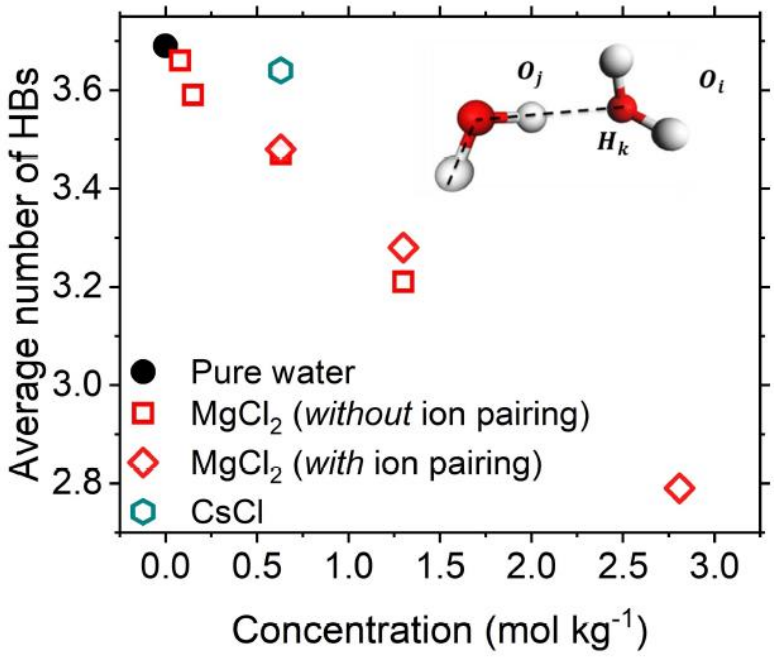

Figure 3. 7 Average number of hydrogen bonds in pure liquid water, aqueous $MgCl_2$ solutions and aqueous CsCl solutions

statistics and dynamics of hydrogen bonds in pure water [69–71], in aqueous electrolyte solutions [19, 68, 72], in the first hydration shell around hydrated ions [73, 74], and at the water-mineral interface [75]. Through the algorithm to find the water pairs forming hydrogen bonds using the above conditions at every time steps in the simulation, we were able to study how many hydrogen bonds are formed on average in the entire system and how they change by ions. The average number of hydrogen bonds (n_{HB}) computed from the ab initio MD trajectories of pure water and $MgCl_2$ solutions are reported in Fig. 3 7. The values of n_{HB} decreases linearly from 3.7 in pure liquid water to 2.8 in the 2.81 mol kg^{-1} $MgCl_2$ solution because the fraction of water molecules engaging in two or three HBs increases with the solute concentration as shown in Table 3. 2. A comparison of the HB statistics in the $MgCl_2$ solutions obtained from ab-

	System	c (mol.kg^{-1})	f_0	f_1	f_2	f_3	f_4	f_5	n_{HB}	Mg^{2+}–Cl^- ion pairing
Water	1	0.00	0.0	0.6	5.8	21.9	66.8	4.8	3.69	
$MgCl_2$	2	0.08	0.0	0.6	6.4	23.0	65.9	4.0	3.66	*without* ion pairing
	3	0.15	0.0	0.9	8.3	25.7	60.6	4.4	3.59	*without* ion pairing
	4	0.63	0.1	2.0	11.2	27.6	55.4	3.7	3.47	*without* ion pairing
	5	0.63	0.1	1.9	11.3	27.4	56.0	3.3	3.48	*with* ion pairing
	6	1.30	0.4	5.7	29.2	45.2	2.6	0.0	3.21	*without* ion pairing
	7	1.30	0.1	3.7	15.7	32.1	46.0	2.4	3.28	*with* ion pairing
	8	2.81	1.6	11.2	24.7	32.9	28.0	1.5	2.79	*with* ion pairing
CsCl	9	0.63	1.0	6.6	23.6	64.4	4.1	0.0	3.64	

TABLE 3. 2 The fraction (f) of water molecules with n number of hydrogen bonds per water molecule, the average number of hydrogen bonds (n_{HB}) per water molecule in bulk water and in aqueous $MgCl_2$ solutions at different concentrations (mol.kg^{-1}), obtained from *ab initio* MD simulations (PBE-D3).

	Forcefield	c (mol.kg^{-1})	f_0	f_1	f_2	f_3	f_4	f_5	n_{HB}
Water	SPC/E	0.00	0.0	1.0	8.9	33.2	51.0	5.8	3.52
$MgCl_2$	Aqvist, SPC/E	0.08							
		0.15	0.0	1.4	11.1	33.6	48.3	5.4	3.45
		0.63	0.1	3.1	16.8	34.3	41.2	4.4	3.27
		1.30	0.5	6.1	22.5	34.0	33.4	3.4	3.04
		2.81	2.6	14.9	30.1	20.2	1.8	0.0	2.56
$MgCl_2$	Duboue-Dijon, SPC/E	0.08	0.1	1.2	9.7	32.7	50.5	5.8	3.50
		0.31	0.1	2.0	12.6	33.6	46.6	5.0	3.40
		0.63	0.2	3.2	15.9	33.9	42.2	4.5	3.28
		1.30	0.7	6.8	21.6	33.7	3.5	0.0	3.03
		2.81	3.3	17.2	30.2	29.6	18.1	1.6	2.47
		3.65	6.8	23.5	31.6	25.2	12.0	1.0	2.15

TABLE 3. 3 The fraction (f) of water molecules with n number of hydrogen bonds per water molecule, the average number of HB (n_{HB}) per water molecule in bulk water and in aqueous $MgCl_2$ solutions at different concentrations (mol.kg^{-1}), obtained from classical MD simulations using the Lennard-Jones potentials developed by Aqvist [47] and Duboue-Dijon et al. [76] to describe the ion-ion and ion-water interactions together with the SPC/E water model.

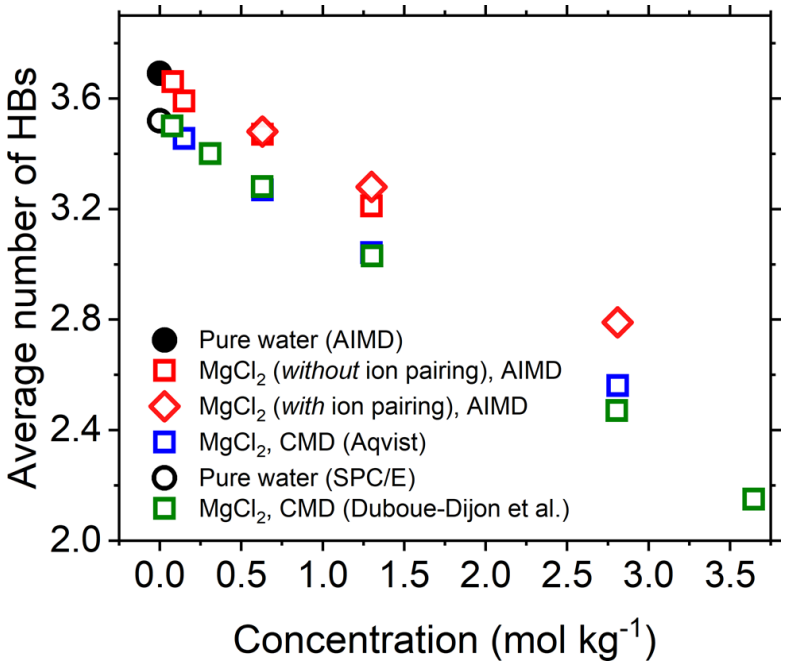

Figure 3. 8 Comparison of the average number of hydrogen bonds (HBs) in pure liquid water and aqueous $MgCl_2$ solutions obtained from *ab initio* MD and classical MD

initio and classical MD simulations is reported in Table 3. 3 and Figure 3. 8. According to the above comparison, the absolute value of the average number of HB shows a slight difference due to the over-structure effect [77] of Ab-initio MD, but the overall trend is consistent. Other chloride-containing solutions with alkali metal ions such as Cs+, which are listed in Table 3. 4, or Na^+ and K^+ [67, 68] display a similar but less noticeable influence. For example, the average numbers (Fig. 3. 7) and distributions (Table 3. 2) of HBs in the 0.63 mol kg^{-1} $MgCl_2$ and CsCl solutions shows that the influence of $MgCl_2$ on the HB network is significantly more pronounced than CsCl. Therefore, the presence in solution of Mg^{2+} causes the observed, large perturbations to the water HB network.

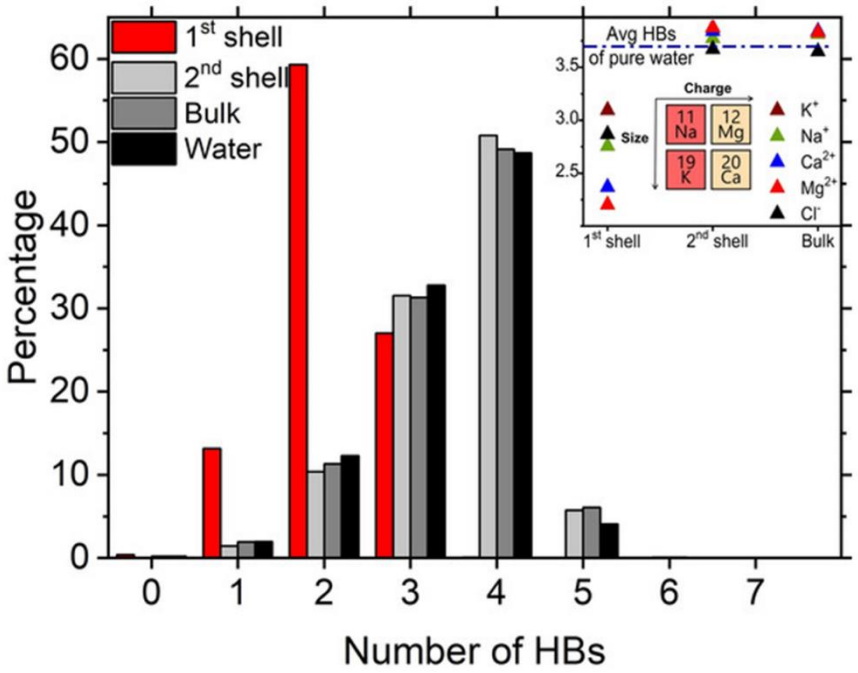

Figure 3. 9 Percentage of H_2O molecules engaging in n HBs in the first and second shell of Mg^{2+} and in the bulk. Inset: Average number of HBs in pure water (blue dashed line) and in the solvation shells of hydrated Mg^{2+}, Ca^{2+}, K^+, Na^+ and Cl^- ions (isolated ions, no counterions).

In Section 3.2, the solvation structure in which water forms a hydration shell near ions was discussed. Using this scheme, we can deepen our understanding by analyzing the hydrogen bond structure change in the different hydration shell. The distribution of HBs in the Mg^{2+} first hydration shell in Fig. 3. 9 has large deviations from bulk behavior, with the waters directly coordinated to Mg^{2+} being mostly hydrogen-bonded to only two other molecules. The inset of Fig. 3. 9 compares the average number of HBs for the water molecules in the first and second hydration shell of the divalent cations Mg^{2+} and Ca^{2+}, of the monovalent cations K^+, Na^+, and Cs^+, and of the anion Cl^-. In the first coordination shell of the ions, the n_{HB} values is the lower than in the bulk but

this effect is particularly strong for the water molecules directly coordinated to Mg^{2+}(n_{HB}=2.25). This further confirms that the influence of $MgCl_2$ on the water-water HB network is due to the specific Mg-water interaction. For all ions, the average number of HBs for the water molecules in the second hydration shell converges to the of "bulk" water (beyond the first and second shells). However, small differences can be observed between the values of "bulk" water and pure liquid water, which are likely due to finite size effects (size of the simulation box). In fact, ab initio MD simulations of one Ca^{2+} ion in 124 H_2O (50 ps) gives n_{HB}=3.72 for "bulk" water, which is very close to that obtained for pure liquid water (3.7). The results in the inset of Fig. 3. 9 also confirms the long-range effects of ions on the water-water HB network discussed by Gaiduk and Galli [66].

Chapter 4

Effect of ion on the water dynamics

4.1 Hydration shell vibrational density of states

Vibrational density of states (VDOS)

Further insights into the effect of ions on the HB network were obtained from the vibrational density of states (VDOS) of the excitation spectrum of water as shown in Fig. 4. 1, which was computed from the ab initio MD trajectories as the sum of the Fourier transform of the velocity-autocorrelation function (VACF) of the oxygen and hydrogen atoms [78]:

$$f(\omega) = \mathcal{F}\big(\gamma(t)\big) = \mathcal{F}\left(\frac{<\sum \vec{v}_i(0)\vec{v}_i(t)>}{<\sum \vec{v}_i(0)\vec{v}_i(0)>}\right) \qquad (4.\ 1)$$

where $\vec{v}_i$ is the velocity vector of O or H atoms in the i-th water molecule,

and the sum is taken over all atoms in the system. The different vibrational modes in system of investigation can be described by VDOS as peaks. The maxima of peaks can be used to determine the resonant frequency of the mode. We can use VDOS to understand influence of ion to intermolecular vibration dynamics in electrolyte solution.

Intermolecular dynamics in hydrogen bonding network

In the low frequency region (0–1200 cm^{-1}), the spectrum in Fig. 4. 1 (A) has a peak at 50 cm^{-1} corresponding to the O−O−O bonding intermolecular motion, at ~250 cm^{-1} corresponding to the O−O intermolecular stretching, and a band between 300 and 1200 cm^{-1} that has been assigned to librational modes, hindered rotational motions of water about the three principal inertia axis of free water [79]. These vibrational (HB stretch) and librational bands are very sensitive to the specific ion-water interactions and ordering of water [79, 80]. We investigated the local effect of the metal cations to the excitation spectrum of water by restricting the averages in equation 4. 1 to the water molecules belonging to the first hydration shell of Mg^{2+} and Ca^{2+}, which were defined by the position of the first minimum in the ion-water radial distribution functions. A previous ab initio MD study of the spectroscopic properties of water around small hydrophobic solutes did not show significant differences with respect the bulk signal [81], but Fig. 4. 1 (B) displays the appearance of clear fingerprints of the ionic solvation shell in the libration region of the VDOS. Moreover, the HB peaks and the librational part of in-shell water of Mg^{2+} is more structured and shifted to higher-frequency modes compared to Ca^{2+}.

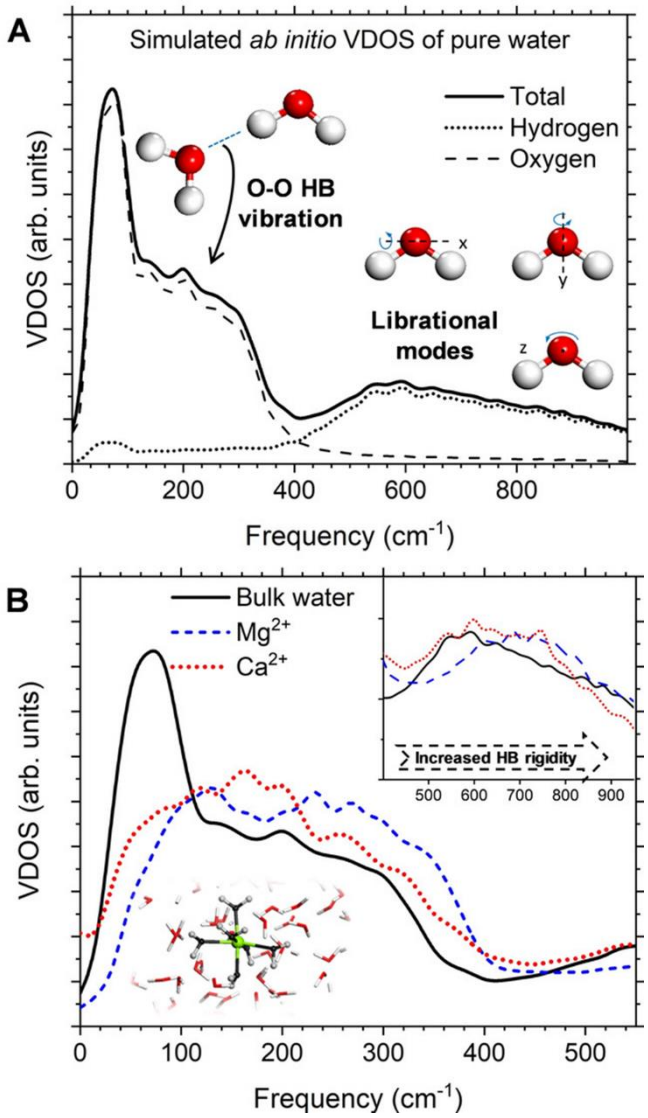

Figure 4. 1 Vibrational density of states (VDOS) from ab-initio MD.
(A) VDOS of pure water showing the vibrational (HB stretch) and librational bands. (B) Comparison of the VDOS of pure water and of the water molecules in the first hydration shell of Mg^{2+} and Ca^{2+}. The first shells were defined by the position of the first min. of the Mg–O (3.0 Å) and Ca–O (3.2 Å) RDFs.

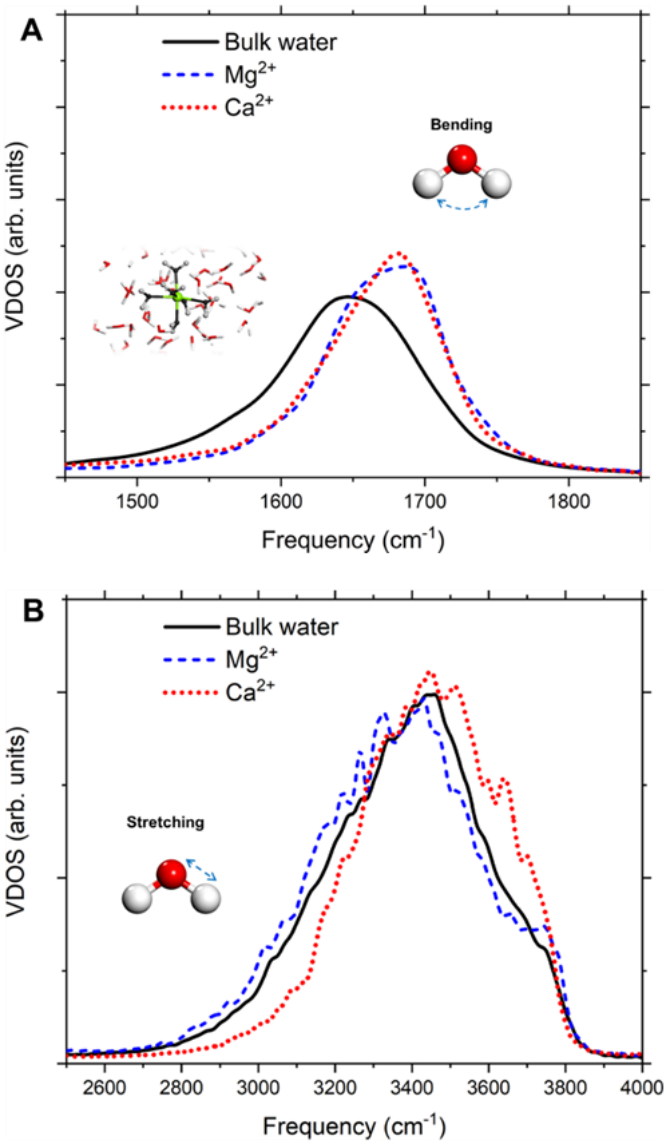

Figure 4. 2 Bending (A) and stretching (B) regions of the vibrational density of states (VDOS) of water. Comparison of pure water and of the water molecules in the first hydration shell of Mg^{2+} and Ca^{2+}.

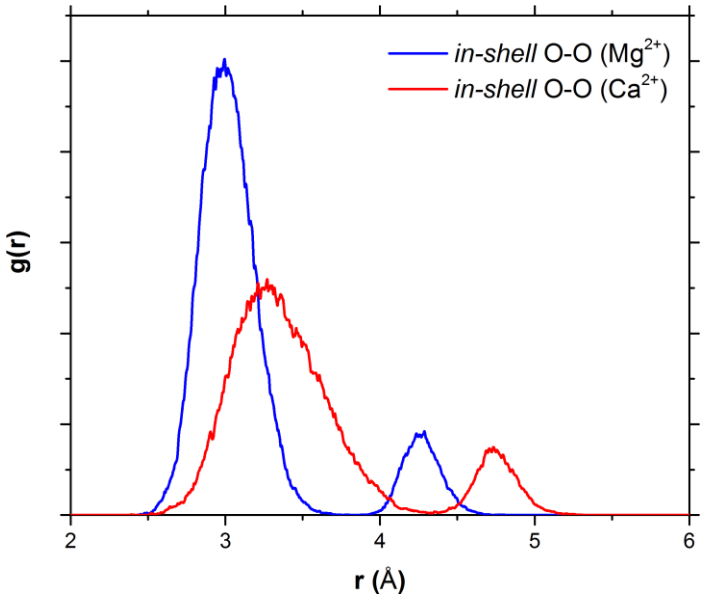

Figure 4. 3 Oxygen–oxygen radial distribution functions [g(r)] for the water molecules that are part of the hydration shell of Mg^{2+} and Ca^{2+} obtained from ab initio MD simulations of isolated ions in solution.

This suggests a stronger water-water HB network around the magnesium ion. In the first hydration shell of these two cations, the bending H−O−H mode is also blue-shifted by approximately 50 cm^{-1} compared to bulk water (cf. 1650 cm^{-1}), whereas less clear conclusions can be drawn from the O−H stretching region between 2500 and 4000 cm^{-1} of the VDOS in Fig. 4. 2. An X-ray spectroscopy study of $MgCl_2$ (aq) by Techer and co-workers assigned the distortions of the pre-, main, and post-edge of the X-ray absorption spectra on the oxygen K-edge in the vicinity of the ions to the strengthening of the HBs in the solvation shell around Mg^{2+} [82]. In shell VDOS analysis agrees with this assignment. Further support to this conclusion is provided by the analysis of the average water-water distance between the water molecules around Mg^{2+} (3.0 Å), which significantly shorter than Ca^{2+} (3.3 Å) in Figure 4. 3.

4.2 Hydrogen-Bond kinetics

According to the approached proposed by Rapaport [83], the dynamics of breaking and making of hydrogen bonds can be quantified in terms of the continuous HB time correlation function (TCF), $S_{HB}(t)$, which gives the probability that a pair, ***i*** and ***j***, remains continuously hydrogen-bonded from time 0 to **t** [19, 84]:

$$S_{HB}(t) = \frac{< h_{ij}(0) \cdot H_{ij}(t) >}{< h_{ij}(0)^2 >} \qquad (4.\ 2)$$

The hydrogen bond population variables $h_{ij}(t)$ and $H_{ij}(t)$ in equation. 4. 2 are defined in the following way: $h_{ij}(t) = 1$ when a tagged water pair is hydrogen-bonded at time t and $h_{ij}(t) = 0$ otherwise; $H_{ij}(t) = 1$ if the tagged water pair remains continuously hydrogen-bonded in the time interval [0, t] and $H_{ij}(t) = 0$ otherwise. To construct this correlation function, we have used the geometrical criteria of hydrogen bonded in Chapter 3. The brackets in equation 4. 2 denote average over all water pairs in the solution. We obtained well convergent $S_{HB}(t)$ profiles by using multiple time origins and overlapping intervals [0, t] of time length equal to 11 ps. The detailed protocol used to compute TCFs is explain in Appendix A and is based on the procedure outlined by Leach [85]. The average HB lifetime, τ_{HB} can be determined from the integration of equation (4. 2). Values of τ_{HB} equal to 1.56 ps and 1.31 ps were obtained from simulation boxes containing 729 and 64 water molecules, respectively, which are within the experimental range of 0.5–1.7 ps [86]. These results support the ab initio MD methodology used in this study to characterize the low-frequency water dynamics.

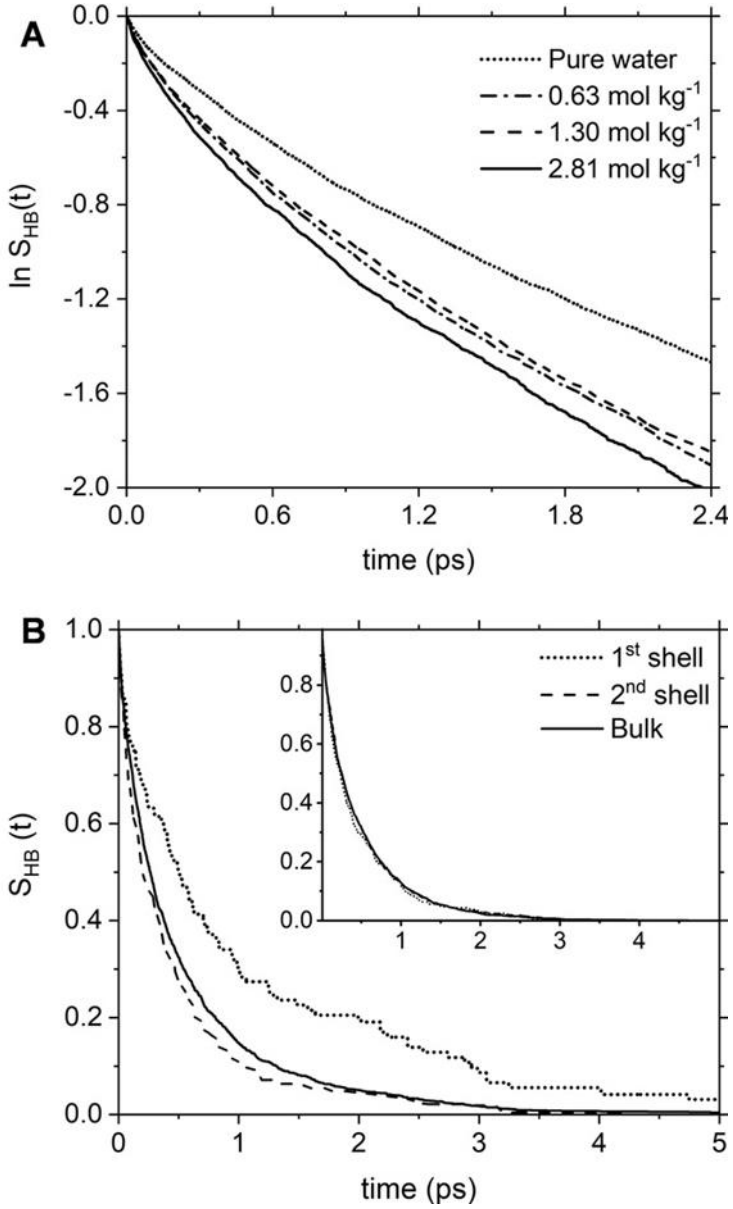

Figure 4. 4 The continuous hydrogen bonding (HB) time correlation functions $\mathbf{S_{HB}}(t)$ for aqueous $MgCl_2$ solutions at different concentrations. (A) Profiles of $\mathbf{S_{HB}}$ for pure water (dotted line) and $MgCl_2$ solutions (dashed and solid lines). (B) Profiles of $\mathbf{S_{HB}}(t)$ for the water molecules in the first and second shell of Mg2+ and Cl− (inset) compared with bulk behavior.

System	c (mol.kg^{-1})		τ_{HB}
729 H_2O	0.00		1.56
64 H_2O	0.00		1.31
$MgCl_2$ (aq)	0.63	*without* CIP	1.26
	0.63	*with* CIP	1.13
	1.30	*without* CIP	1.22
	1.30	*with* CIP	1.17
	2.81	*with* CIP	1.06
Mg^{2+} (aq)		1st shell	2.09
		2nd shell	1.93
		Overall	1.68
Cl^- (aq)		1st shell	1.36
		2nd shell	1.25
		Overall	1.28

TABLE 4. 1 Relaxation time, τ_{HB}, computed from the integration of the continuous hydrogen bond correlation function. Relaxation times are expressed in units of ps.

Fig. 4. 4 compares $S_{HB}(t)$ profiles obtained for pure liquid water and $MgCl_2$(aq) with Mg^{2+}–Cl^- contact ion pairs in solution; the analysis of the solutions without ion pairing gave very similar results. The HB dynamics are faster in $MgCl_2$ solutions (faster decay of $S_{HB}(t)$ profiles) than in pure water and accelerates with the solute concentration. This is confirmed by the average HB lifetimes in aqueous $MgCl_2$ solutions, which are lower than pure water; the fastest dynamics of HB making/breaking is observed for the 2.81 mol kg^{-1} $MgCl_2$ solution with CIPs as shown in table 4. 1. Therefore, the presence of Mg^{2+} and Cl^- in solution weakens the water-water strength of pairing. Further insights can be obtained from the characterization of the HB dynamics of the water molecules in the first hydration shells of Mg^{2+} and Cl^-. In Fig. 4. 4 (B), the $S_{HB}(t)$ profiles of the first hydration shell of Mg^{2+} has a slower decay

(slower HB dynamics) than bulk water and the $S_{HB}(t)$ profiles of the second hydration shells of Mg^{2+} has faster decay (faster HB dynamics) than bulk water. The effects of Mg^{2+} on the surrounding water molecules follow, therefore, the ionic hydration model proposed by Frank and Wen [87]: in the innermost region the water molecules are tightly bound to Mg^{2+} and exhibit lower HB dynamics than those in pure water; in the second region the magnesium ion induces a "structure breaking effect", wherein disruption of the hydrogen bonding network enhances the mobility of the water molecules [88]. Dissolved Mg^{2+} ions have a long-range effect, which goes beyond the first hydration shell. In comparison, the $S_{HB}(t)$ profiles of the first and second hydration shells of Cl^- overlap with that of bulk water suggesting that the chloride ion does not have short- or long-range effects on the HB dynamics of water as shown in Fig. 4. 4 (B). As shown in table 4. 1, The computed values of the HB relaxation time of the solvent molecules in the first (1.35 ps) and second (1.25) shell of chloride, and in the bulk of the solution (1.28 ps) confirm this observation. The different influence of Mg^{2+} and Cl^- on the HB dynamics of the surrounding water molecules should be linked to the hydration numbers of these two ions, which have estimated values of h=15 for Mg^{2+} and h=0 for Cl^-, according to (thermodynamic) colligative [89] and isothermal compressibility data [90]. The long-range effects of Mg^{2+} beyond its first shell also explains why the hydration number does not correspond to the coordination number (6).

4.3 Water reorientation dynamics

Rotational motion of water molecules plays a crucial role in the breaking and making of HB (more strongly hydrogen-bonded water molecules reorient more slowly) [91,92]. We have quantified the rotational relaxation of the water dipole by computing the first-order Legendre polynomial time correlation function [93]:

$$C_1(t) = \frac{< \vec{\mu}(0) \cdot \vec{\mu}(t) >}{< \vec{\mu}(0)^2 >} \qquad (4.\ 4)$$

where $\vec{\mu}(0)$ and $\vec{\mu}(t)$ are the unit vectors defining the orientation of the dipole moment of a water molecule at times 0 and t, respectively. The average in equation (4. 3) was computed over all water molecules in the solution, using multiple time origins and overlapping intervals [0, t] of equal time length (t=16 ps). In Fig. 4. 5, the $C_1(t)$ function starts at 1 and decays asymptotically to zero because of the random and isotropic orientation of the water molecules in solution. The early stage of fast loss of correlation is caused by librational motion. The long-term decay is due to reorientational motion and is fitted by a bi-exponential function $a \cdot \exp(-t/\tau_1)+b \cdot \exp(-t/\tau_2)$ [93]. The relaxation time associated with the reorientational motion, τ_{reor}, is given by the weighted average of the fitting parameters τ_1 and τ_2:

$$\tau_{reor} = \frac{a \cdot \tau_1 + b \cdot \tau_2}{a + b} \qquad (4.\ 4)$$

The bi-exponential fitting curve gives a more accurate estimate of the relaxation time associated with the water reorientation process because it removes the contribution from the water librational dynamics. It is also important to note that the single-water relaxation times computed from the

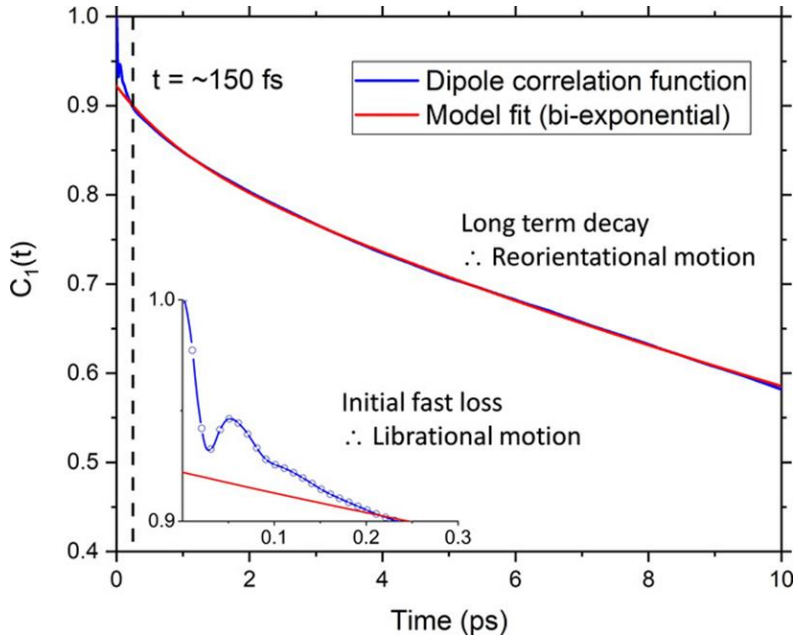

Figure 4. 5 Orientation time correlation function $\mathbf{C_1(t)}$ obtained from ab initio MD of pure liquid water.

integration of the first-order Legendre polynomial-time correlation functions cannot be directly compared with reorientation times obtained experimentally using dielectric relaxation spectroscopy. To realize such comparison the TCF of the total system dipole correlation should be considered by computing the auto- and cross-correlation terms, as done by Sega and Schroder [94], and Zarzycki and Gilbert [95]. The connection between single-water molecule reorientational dynamics and dielectric relaxation spectroscopy measurement is explained in Appendix B. The concentration-dependent time correlation profiles, $C_1(t)$, of the MgCl2 solutions are reported in Figure 4. 6. Compared to pure water, the dipole reorientation dynamics is slower in $MgCl_2$(aq) and decreases with the solution concentration. The $C_1(t)$ profiles are also significantly influenced by the type of ion pairs present in solution; the 0.63

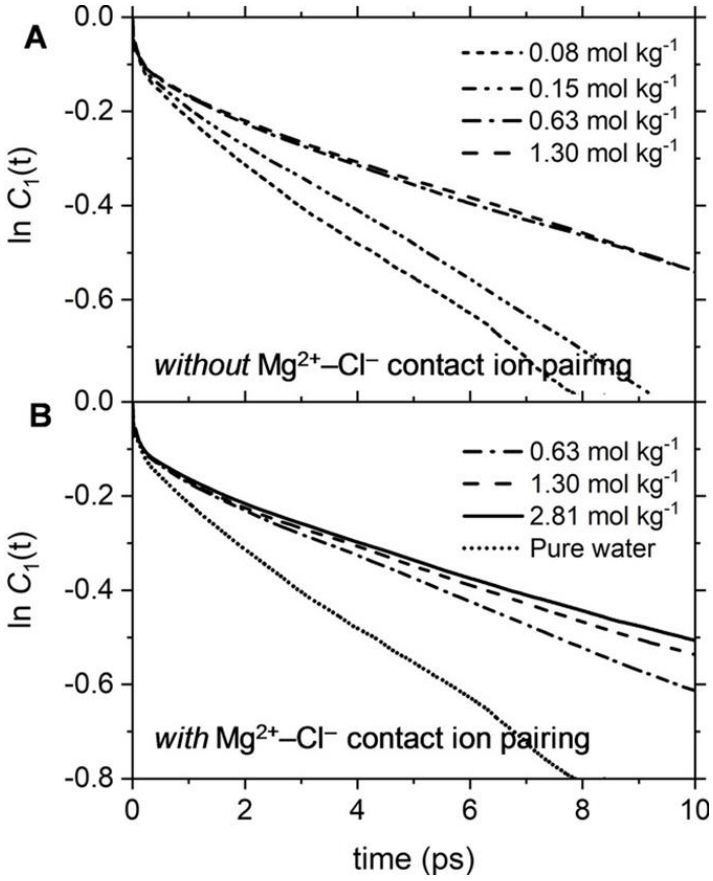

Figure 4. 6 The time dependence of the orientation time correlation function $\mathbf{C_1}(\boldsymbol{t})$ for aqueous $MgCl_2$ solutions at different concentrations. (A) Solutions *without* Mg^{2+}-Cl^- contact ion pairing. (B) Solutions *with* Mg^{2+}-Cl^- contact ion pairing.

and 1.30 mol kg^{-1} solution without CIPs have very similar water reorientation behavior in Fig. 4. 6 (A), whereas significant differences can be observed in the solutions with CIPs in Fig. 4. 6 (B). The correlation function $\mathbf{C_1}(\boldsymbol{t})$ is, therefore, sensitive to solution speciation and could provide insights into the cooperative effect of Mg^{2+} and Cl^- ions on the water dipole reorientation dynamics.

Chapter 5

Cooperative effect on ion hydration

5.1 Cooperative hydration model

Speciation analysis of the aqueous $MgCl_2$ solutions shown in Table 2. 3 in Chapter 2 shows that Mg^{2+} and Cl^- ions are mainly present as free ions only in the most dilute solutions (0.08 and 0.15 mol kg^{-1}). Otherwise, they form contact, solvent shared, and solvent-separated ion pairs. As cooperative effects of ions in the aqueous electrolyte can induce specific changes to the water dynamics [96, 97], we have implemented a cooperative hydration model to categorize the water molecules in $MgCl_2$(aq) in different subpopulations in Fig. 5. 1 and characterize the dynamic properties of water depending on the relative position from the ions.

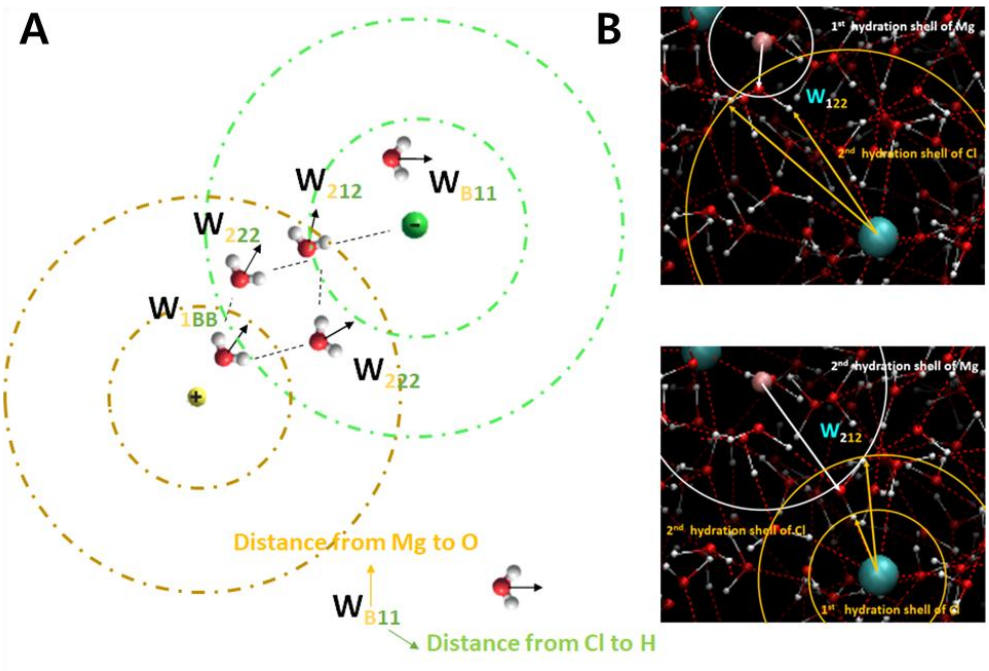

Figure 5. 1 Classification of different water molecules into different subpopulation by using cooperative hydration scheme (A) Cooperative hydration model in solvent separated ion pair (B) Water classification in snapshot of ab-initio MD simulation

The hydrogen and oxygen atoms in each water molecule were labelled $O_aH_bH_c$ where a, b, c = 1, 2, and B in terms of the following criteria: 1 when the atom in the first coordination shell of the nearest ion; 2 when the atom is in the second coordination shell of the nearest ion; B when the above conditions are not met. Assignments were made by comparing the distance between O_a and the nearest magnesium ion with position of the first (r_{Mg-O}^{min1}) and second (r_{Mg-O}^{min2}) minima of the Mg–O RDF in Fig. 5. 2 (A), and the distance between H_b (or H_c) and the nearest chlorine ion with first (r_{Cl-H}^{min1}) and second (r_{Cl-H}^{min2}) minima of the Cl–H RDF in Fig. 5. 2 (B):

i. O_a is labelled O_1 if $r_{Mg-O_1} < r_{Mg-O}^{min1}$;

ii. O_a is labelled O_2 if $r_{Mg-O}^{min1} < r_{Mg-O_1} < r_{Mg-O}^{min2}$;

iii. O_a is labelled O_B if $r_{Mg-O_1} > r_{Mg-O}^{min2}$;

iv. H_b (or H_c) is labelled H_1 if $r_{Cl-H} < r_{Cl-H}^{min1}$;

v. H_b (or H_c) is labelled H_2 if $r_{Cl-H}^{min1} < r_{Cl-H_b} < r_{Cl-H}^{min2}$;

vi. H_b (or H_c) is labelled H_B if $r_{Cl-H_b} > r_{Cl-H}^{min2}$.

Using these geometrical criteria at time $t = 0$, the water molecules in the $MgCl_2$ solutions were classified in different water subpopulations labelled $\mathbf{W_{abc}}$ as shown in Fig. 5. 1. For example: $\mathbf{W_{111}}$ refers to a subpopulation of water molecules of type $O_1H_1H_1$ where oxygen is in the first coordination shell of Mg^{2+} and both hydrogen atoms are in the first coordination shell of Cl^-; $\mathbf{W_{112}}$ refers to a subpopulation of water molecules of type $O_1H_1H_2$ where oxygen is in the first coordination shell of Mg^{2+}, a hydrogen is in the first coordination shell of Cl^- and the other is the second coordination shell of Cl^-. The continuous HB and dipole reorientational TCFs were then evaluated for all **Wabc** subpopulations.

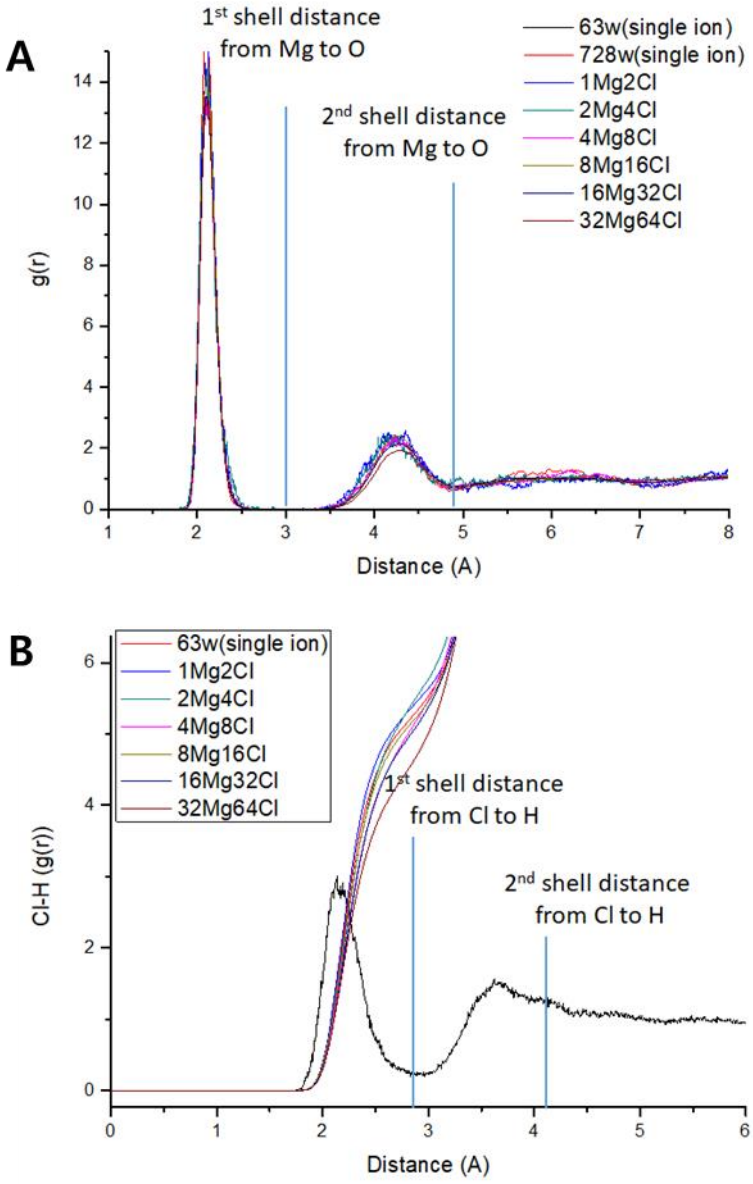

Figure 5. 2 Radial distribution function and geometric criteria for cooperative hydration model (A) Mg-O RDF (B) Cl-H RDF

The application of these criteria to categorize water molecules in $MgCl_2$ solutions is based on the semi-rigid hydration scheme, where water dynamics are "locked" in two directions: the orientation of the water dipole is mainly affected by cations; the O-H orientation is mainly affected by anions [96]. Previous experimental and simulation work provide evidence for orientation ordering of water in extended hydration shells around the ion [98-101]. Using this approach, the water molecules in the solution can be classified into 18 subpopulations, W_{abc}, where a, b, c=1, 2, B. For examples, W_{112} refers to the subpopulation $O_1H_1H_2$ of molecules having the oxygen in the first coordination shell of Mg^{2+}, one hydrogen atoms in the first coordination shell of Cl^-, and the other hydrogen in the second shell of Cl^-. The number of water molecules in W_{11B}, W_{21B}, and W_{B1B} are zero because these subpopulations correspond to molecules where the O-H bond is dissociated, that is one hydrogen is in the first shell and the other hydrogen in the bulk. The detailed analysis of the process of water "exchange" between different subpopulations is presented in Appendix C. Fig. 5. 3 reports the distribution of water molecules among the fifteen subpopulations in the 1.3mol kg^{-1} MgCl2 solution. The subpopulation analysis has been conducted at each time step using four simulation blocks each lasting 5 ps. The error bars in Fig. 5. 3 are <1 % because of the small variation of the average number of water molecules in each subpopulation during the four consecutive time blocks in Fig. 5. 4. From this population distribution is also possible to evaluate the number of water molecules that are in the bulk (or free water), coordinated to one ion, or coordinated to both Mg^{2+} and Cl^- in Fig. 5. 5. The fraction of bulk and single-coordinated ion per number of Mg^{2+} decreases as the $MgCl_2$ concentration increases and beyond 1.3 mol kg^{-1} most molecules are coordinated to both ions. This makes cooperative ionic effects important in most solutions.

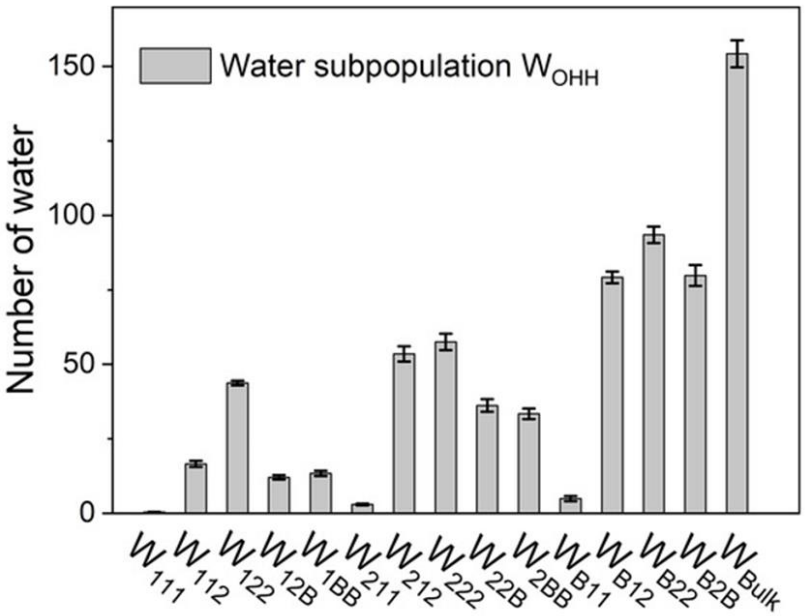

Figure 5. 3 Distribution of molecules among the subpopulations for the 1.3 mol kg^{-1} $MgCl_2$ solution

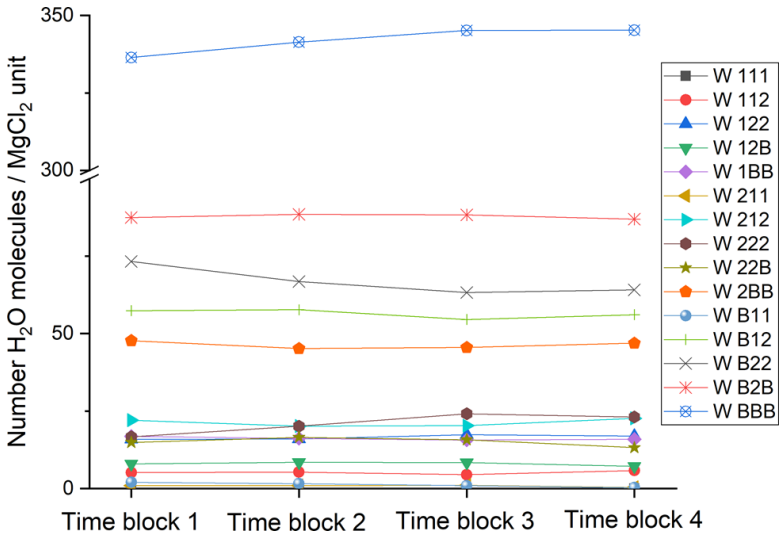

Figure 5. 4 Variation of the average number of molecules into the water subpopulations during four consecutive non-overlapping time blocks each lasting 5 ps. (0.6 mol.kg^{-1} $MgCl_2$ solution)

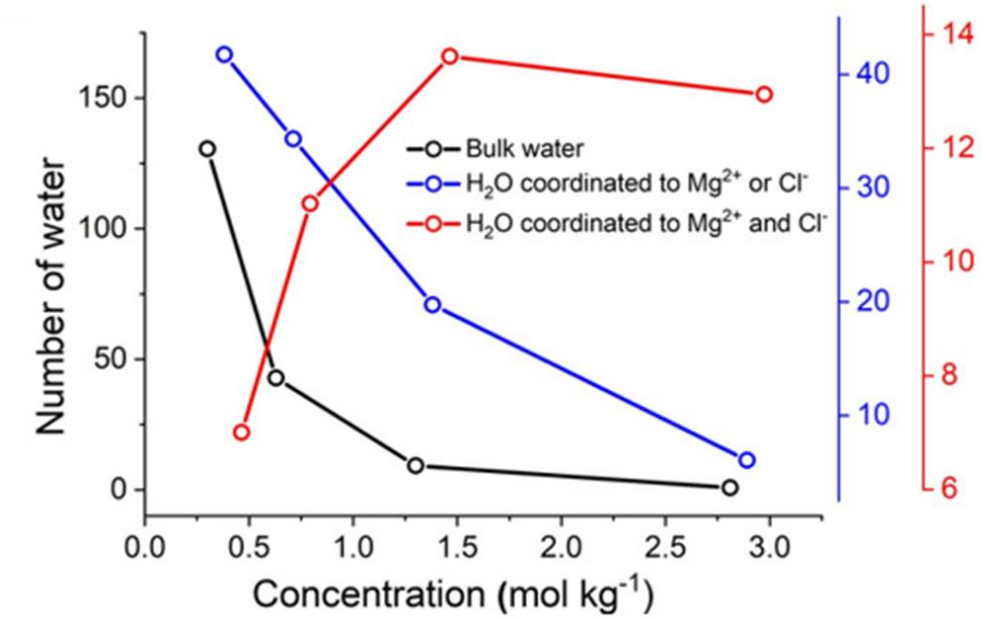

Figure 5. 5 Number of water molecules in the bulk (black), coordinated to either Mg^{2+} or Cl^{-} (blue), or coordinated to both Mg^{2+} or Cl^{-} (red). Values normalized to $MgCl_2$ units.

5.2 Reorientation dynamics in different water subpopulation

For each water subpopulations, the orientation time correlation function was computed by tracking the dipole vectors of the water molecules belonging to that specific subpopulation. We used 1024 time origins to generate well convergent $C_1(t)$ profiles from which we computed the reorientation relaxation time of each water subpopulation. We define the retardation factor as the ratio between the reorientation relaxation time of the subpopulation i and bulk water:

$$f_i = \frac{\tau^i_{W_{OHH}}}{\tau^i_{W_{bulk}}} \quad (5.\ 1)$$

The retardation factors for the subpopulations in the 2.81 mol kg−1 MgCl2 solution are reported in Fig. 5. 6 (A). The inset of this figure presents the statistical approach we have adopted to classify bulk-like and hydration water, which is based on the empirical rule, known as the three-sigma rule: for a subpopulation to be classified as bulk-like water the retardation factor must lie within 3σ of the mean value of bulk-like water (green domain in Fig. 5. 6 (A)). Water molecules in W_{222}, W_{22B}, W_{B11}, W_{B12}, W_{B22}, and W_{B2B} (f≈1) are within the 2σ deviation and are classified as bulk-like water. On the other hand, the slow relaxation dynamics (f values 2–6 times larger compared to the bulk) is observed for water molecules that are in the first coordination shell of Mg^{2+} (subpopulations W_{111}, W_{112}, W_{122}, W_{12B}, W_{1BB}) or in the second coordination shell of Mg^{2+} and first coordination shell of Cl^- (W_{211}, W_{212}) as shown in Fig. 5. 6 (B). The $C_1(t)$ profiles of the water molecules in the first and second coordination shells of hydrated Mg^{2+} and Cl^- (isolated ion, no counterions) confirm the long-range effect of Mg^{2+} and short-range effect of Cl^- on the reorientation water dynamics as shown in Fig. 5. 7. In particular, W_{211} and W_{212} are distributed well beyond the 3σ deviation (even larger than 4σ) and contribute, therefore, to the hydration water of $MgCl_2$(aq). As shown above, unlike other waters belonging to the second hydration shell of Mg^{2+}, W_{211} and W_{212} have slow reorientation motion compare to bulk-like water. On the other hand, looking at the reorientation dynamics of water molecules around isolated Cl^-, it can be considered that Cl^- alone cannot significantly change the reorientation dynamics of water without Mg^{2+}. Therefore, the effect of ions on reorientation dynamics should be understood as a concept of cooperative effect, not merely as an effect of individual ions.

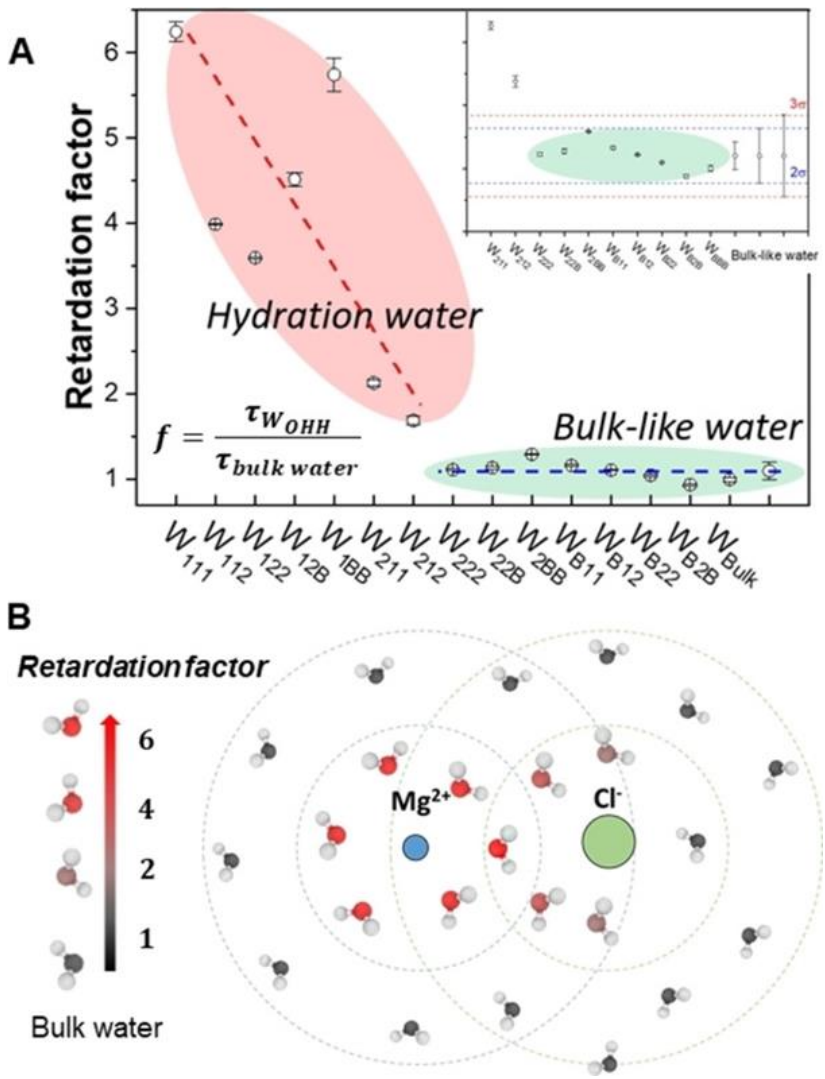

Figure 5. 6 Retardation factor of each water subpopulation.

(A) Retardation factor for the reorientation relaxation time of the water subpopulations in the 2.81 mol kg^{-1} solution *Inset*: statistical approach used to classify bulk-like and hydration (B) Representation of the slow relaxation dynamics (red area) for the subpopulations of molecules in the first or second shell of Mg^{2+} and in first coordination shell of Cl^{-}.

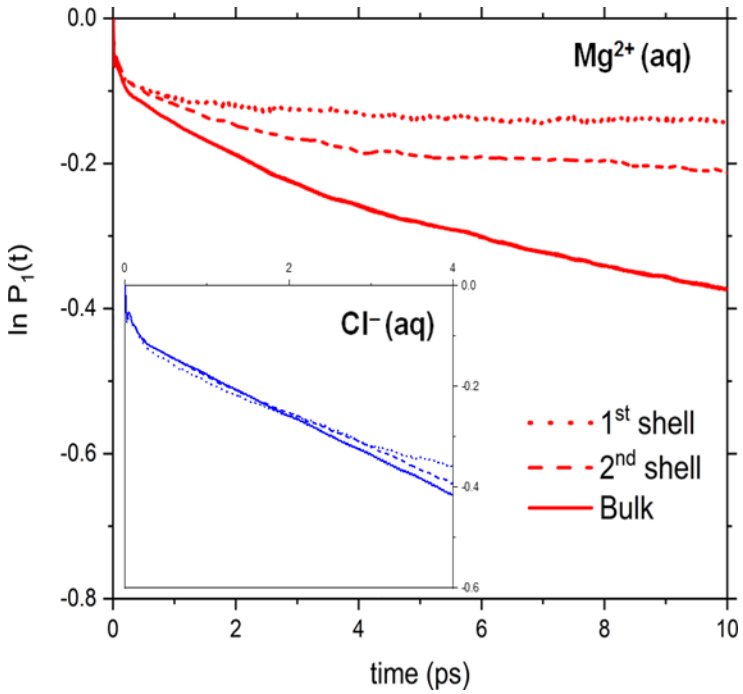

Figure 5. 7 First-order Legendre reorientational TCFs, $\boldsymbol{P_1(t)}$, of the water molecules in the first and second coordination shells of Mg^{2+} and Cl^{-}. Results compared to $\boldsymbol{P_1(t)}$ of the water molecules in the bulk (beyond the second coordination shell of the ion).

This result also agrees with a theoretical analysis on individual water entropy around ions, which showed that the rotational entropy reduction of the first solvation shell water molecules near Cl^- is almost half compared to that around Mg^{2+} [101]. The retardation of the water dipole reorientation near ions, including Mg^{2+} [102], has also been discussed in the "jump model" by Stirnemann et al. to explain the long- and short-range effects of Mg^{2+} on the orientation time correlation function. Our finding that subpopulations such as W_{211} and W_{212} in $MgCl_2$(aq) have a slow reorientation dynamics compared to bulk behavior supports previous investigations of electrolyte solutions reporting on the long-range effects of ions, beyond their first hydration shell [96, 103, 104]. The combined THz absorption spectroscopy (frequency region 50–640 cm^{-1}) and classical MD study of MgSO4 solutions by Vila Verde et al. [104] suggests that the reorientational dynamics of the water molecules between two ions in the solvent shared configuration is slowed down, via a cooperative, supra-additive, effect. Also, the hydration number of Mg^{2+} deduced from THz dielectric relaxation and THz absorption spectroscopy is well above the number of water molecules in the first hydration shell of Mg^{2+} (6) [96], which again suggests that some portion of water molecules beyond the first hydration shell of Mg^{2+} have different physical property (such as vibrational absorption or reorientation dynamics) compared to bulk water.

Hydration numbers from water reorientation dynamics

The number of bulk-like and slow-orienting molecules in the water subpopulations of the 0.6 mol kg^{-1} $MgCl_2$ solution are reported in Fig. 5. 8. Here, we define the hydration number (h) as the number of water molecules per dissolved $MgCl_2$ units that no longer participate in bulk-like reorientation dynamics. This definition yields an h value of 15 for the 0.6 mol kg^{-1} $MgCl_2$ solution, which corresponds to approximately 6 slow water molecules in the first shell of Mg^{2+} and 9 slow water molecules that are beyond the first shell of this ion. The hydration numbers identified using our computational procedure is independent from the structural definition of the hydration shells and corresponds slow water molecules within or outside the first hydration shells of magnesium and chloride ions.

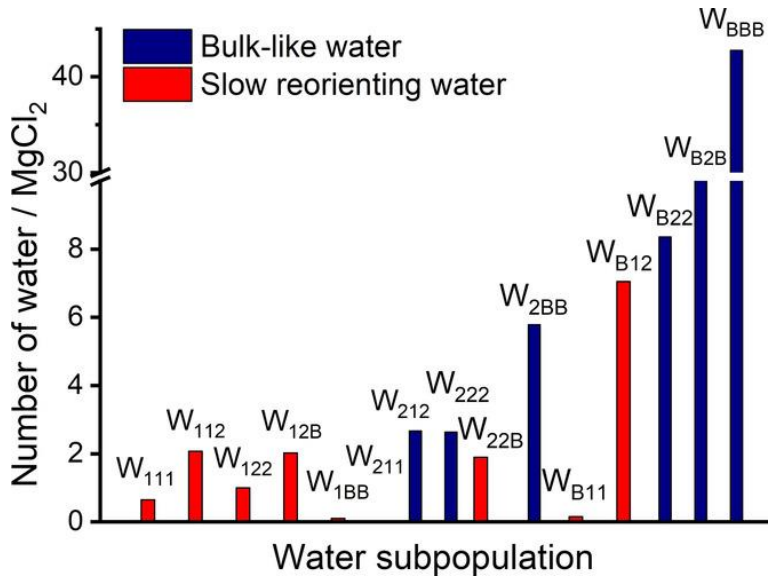

Figure 5. 8 Distribution of water molecules in the water subpopulations labelled as bulk-like (blue) and slow (red) reorienting water dipoles for the 0.6 mol kg^{-1} $MgCl_2$ solution.

5.3 Dielectric relaxation spectroscopy of ion solution

The concentration-dependent dielectric loss spectra of $MgCl_2$ solutions with concentrations ranging from 0.0 to 2.6 mol kg^{-1} (Appendix E) as shown in Fig. 5. 9 were analyzed by simultaneously fitting the real and imaginary parts of the spectra to the double-Debye dielectric relaxation model for the frequency dependent dielectric permittivity (ϵ) [105, 106]:

$$\varepsilon(\omega) = \frac{S_1}{1 + i\omega\tau_1} + \frac{S_2}{1 + i\omega\tau_2} + \varepsilon_\infty \qquad (5.\ 2)$$

where ε_∞ is the high-frequency permittivity in aqueous solution, which was set equal to 3.52 based on recent THz spectroscopy experiments of aqueous salt solutions [25]. The first and second terms in equation (5. 2) are due to the reorientation motion of water with mode strength S_1 and relaxation time τ_1 (centred at 20 GHz), and mode strength S_2 and relaxation time τ_2 (centred at 1 THz). The conductivity term due to Ohmic loss from the ion conductivity was removed by conducting independent conductivity experiments, such that only dielectric relaxation contribution from dipole fluctuation was considered in the fitting process. According to the extended Cavell equation [107], the intensities of the relaxation modes S_1 and S_2 are proportional to the number of molecules participating to each mode. The dielectric strength of an aqueous electrolyte solution with concentration c, $S(c) = S_1 + S_2$, is generally less than that of neat water due to the following depolarization effects [97]: dilution effect, ions in solutions reduce the number of waters per unit volume resulting in the decrease of dipole concentration; kinetic depolarization, under the

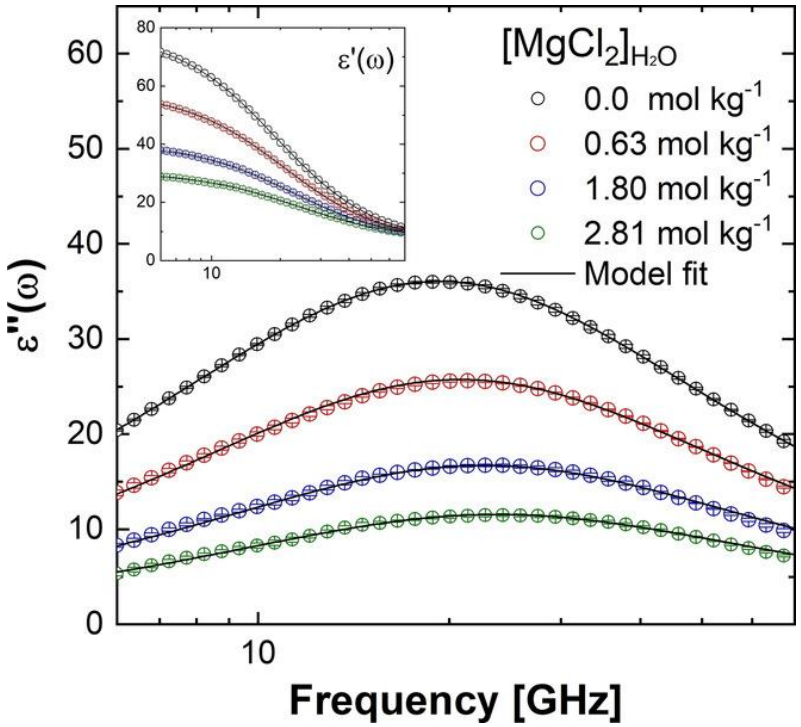

Figure 5. 9 Concentration-dependent dielectric loss spectrum of aqueous $MgCl_2$ solutions. Imaginary and real (inset) components of the double-Debye dielectric relaxation model.

influence of an external electric field, ions in solution diffuse according to the direction of the field, inducing a reorientation of the surrounding water molecules that is opposite to the direction of the field; static depolarization, some water molecules in the solution are bound or strongly affected by the presence of ions and are oriented towards the local ionic field caused. These water molecules have the slow reorientation dynamics with a relaxation time that is outside the GHz-to-THz window in which the reorientation process of bulk-like water occurs [96]. Therefore, the water molecules in an electrolyte solution which reorientation dynamics is retarded with respect to bulk behavior do not contribute to the GHz-to-THz dielectric spectrum, leading to an additional dielectric loss in this frequency range.

In dielectric relaxation spectroscopy, the hydration number of an aqueous electrolyte solution is defined as the number of water molecules characterized by a slow reorientation dynamic and that do not contribute to the bulk-like relaxation process. To determine the hydration numbers of $MgCl_2$ solutions from the dielectric loss spectra, first the static depolarization component is computed, according to the total depolarization model, as the difference between the total dielectric loss (ΔS_{total}) and the kinetic depolarization contribution ($\Delta S_{kinetic}$) [106, 108]:

$$\begin{aligned}\Delta S_{static} &= \Delta S_{total} - \Delta S_{kinetic} \\ &= \Delta S(c) - \sigma(c) \cdot \frac{2\tau_1}{3} \frac{\varepsilon_\infty(c) - \varepsilon_s(0)}{\varepsilon_s(0)\varepsilon_0}\end{aligned} \tag{5. 5}$$

where $\varepsilon_s(0)$ is the static permittivity of pure water, $\varepsilon_\infty(c)$ is the high-frequency permittivity of the aqueous electrolyte solution, and $\sigma(c)$ is the conductivity of electrolyte solution with concentration c. The expression for the kinetic depolarization assumes that water dipoles rotate to the opposite direction of the external field and according to their reorientation time scale. Therefore, $\tau_1(0)$ is the reorientation time of the bulk water relaxation mode, and the 2/3 factor originates from the assumption that the flow of solvent at the ion surface is governed by the perfect slip boundary condition [106]. By considering the dilution effect, the number of slow water molecules (hydration number) is obtained using the following expression:

$$N_{hyd} = \frac{1}{c} \cdot \left(c_{H_2O}(c) - \frac{S(0) + \Delta S_{static}}{S(0)} c_{H_2O}(0) \right) \tag{5. 4}$$

where $c_{H_2O}(c)$ and c represents the concentration of water and of solute, respectively. In dielectric relaxation spectroscopy, larger amounts of depolarization were measured than depolarization by dilution effect and

kinetic depolarization. This amount of depolarization can be explained by the presence of the water molecules which no longer participate in bulk-like reorientation dynamics. This corresponds to the hydration water [96, 97].

5.4 Cooperativity in ion hydration

Fig. 5. 10 compares the values of hydration number h(c) for aqueous $MgCl_2$ solutions with concentrations ranging from 0.1 to 2.8 $mol\,kg^{-1}$ obtained computationally from the ab initio MD simulations and experimentally from the concentration-dependent dielectric loss spectra. The connection between single-water molecules reorientational dynamics and the values obtained from DRS measurements is discussed in Appendix B. The theoretical values are in good agreement with the experimental hydration numbers, especially at higher concentrations. The two h(c) profiles diminish as the concentration increases because of the cooperative hydration of Mg^{2+} and Cl^- ions beyond their first hydration shells (Fig. 5. 10, inset), which corresponds to a decrease of the number of water molecules belonging to the first and second shells of Mg^{2+} with an increase in salt concentration. Since ab initio MD simulations is a very computational intensive technique, it would be more advantageous using trajectories generated from classical MD. Divalent cations such as Mg^{2+} represent a challenge for empirical force field calculations, particularly regarding the treatment of over-polarization and Coulombic singularities [109], with several works discussing the importance of polarization and charge transfer in modulating the properties of water [110, 111]. A simple approach to improve force fields for electrolyte solutions is the electronic continuum correction (ECC) [109, 112, 113]. In this approach, the fast electronic polarization is taken into account in a mean field approach and implemented numerically by scaling the charges of the ions. Here, we have

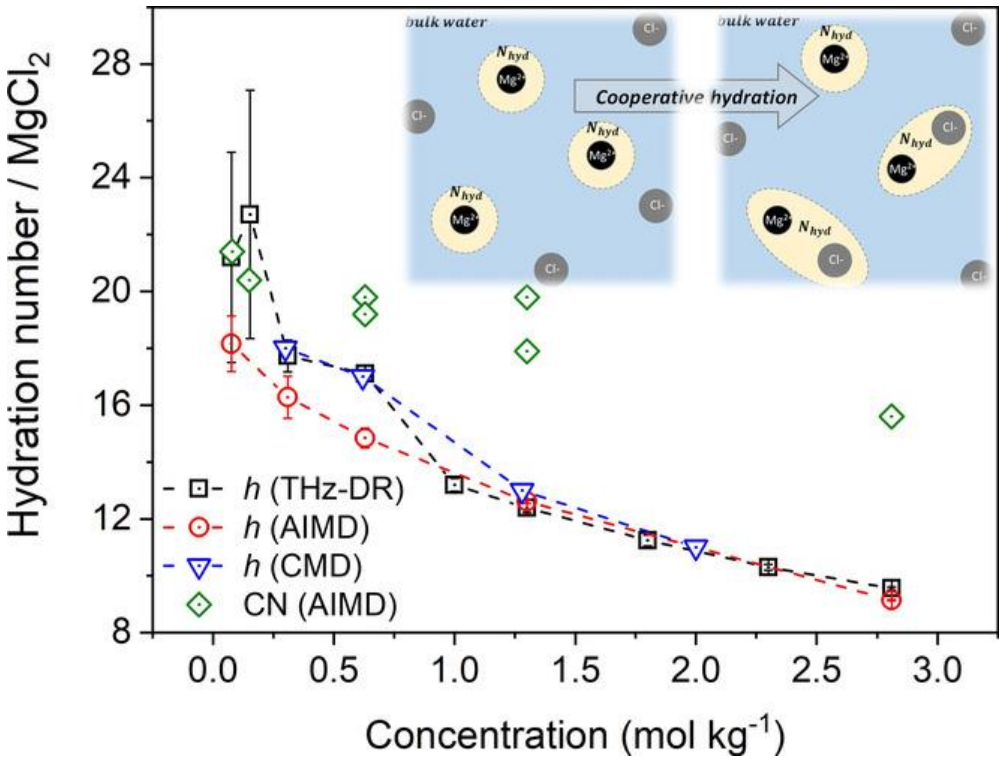

Figure 5. 10 The hydration numbers (h) of $MgCl_2$ as a function of concentration computed from the water reorientation dynamic analysis of *ab initio* and classical MD simulations, and from the THz-DR experiments.

used the Lennard-Jones potentials for $MgCl_2$ solutions parameterized by Duboue-Dijon et al. named ECC [30], in which the charges for the magnesium and chlorine ions are set to +1.7 and −0.85, respectively, and the water molecules are represented by SPC/E. Di Tommaso and co-workers have conducted a detailed assessment of several non-polarizable interatomic potentials for hydrated Mg^{2+} by computing the energetic (gas phase dissociation reaction of $Mg(H2O)_6$), structural (Mg-water radial and angular distribution functions), dynamic (velocity-autocorrelation function of Mg), and kinetic (free energy of Mg-dehydration) properties [48]. Overall, the potential model of Duboue-Dijon (ECC big) provided the best agreement with respect to quantum mechanical and experimental reference data. The retardation factor associated with the water subpopulations of MgCl2 was determined with the approach used for ab initio MD as shown in Appendix D, from which the hydration numbers of MgCl2(aq) was computed as a function of the salt concentration. Fig. 5. 10 shows the hydration numbers generated from the classical MD trajectories of $MgCl_2$ (100 ps) are consistent with the ab initio MD result and in good agreement with dielectric relaxation spectroscopy, especially at lower concentration, probably because of the longer simulation period. Fig. 5. 10 also reports the average coordination number (CN) of the first and second shell of Mg^{2+} as a function of the $MgCl_2$ concentration, which were obtained from the integration of the Mg−O radial distribution functions at the second minima. Except for the more dilute solution, the values of CN are too high compared with the hydration numbers obtained from the water reorientation dynamic analysis. Since the coordination number is based on a simple spatial definition, it cannot capture the subtle cooperative hydration effects of Mg^{2+} and Cl^{-} on the dynamical properties of the surrounding water molecules.

Chapter 6

Summary and Conclusion

By means of ab initio MD simulations, we have investigated the structural and low-frequency dynamics of aqueous $MgCl_2$ solutions, with concentrations ranging from 0.1 to 2.8 mol kg^{-1}. Compared with bulk water, $MgCl_2$ has a considerable influence on the water-water hydrogen bonding network, as confirmed by detailed analysis of the radial distribution function, hydrogen bonding statistics, and vibrational density of states, which we have ascribed to the specific strong Mg-water interaction. The dynamics of the hydrogen bond network solutions was characterized in terms of the water-water hydrogen bonding lifetimes and water dipole reorientation. The presence of $MgCl_2$ in solution accelerates the dynamics of hydrogen bond making and breaking because of the weakening of the water-water interaction strength. These effects have been assigned to the specific strong Mg-water

interaction rather than the Cl-water interaction.

We propose an approach to determine concentration-dependent values of the hydration number of $MgCl_2$(aq) based on the water dipole reorientation dynamics. In this methodology, a hydration status analysis is devised to quantify the cooperative effect of ions on the reorientation dynamics of different water subpopulations in electrolyte solutions. This hydration model provides a tool to characterize the behavior of water in the hydration shell of ions and quantify the cation-anion mixture effect on water reorientational dynamics. We have found that water molecules that are in the first shell of Mg^{2+}, and water molecules that are in the second shell of Mg^{2+} and the first shell of Cl^- have a retarded reorientation dynamics compared with bulk-like behavior, but no cooperative long-range effects are observed for water molecules that are in the second hydration shell of Mg^{2+} and Cl^-. The hydration number is determined from the number of moles of water molecules per mole of dissolved salt that no longer participate in bulk-like reorientation dynamics. The hydration numbers of $MgCl_2$ from this ab initio MD analysis are in good agreement with those obtained from dielectric relaxation spectroscopy. This approach is based on a well-defined criterion for the definition of the hydration number and provides a link between this macroscopic parameter and the molecular-level processes responsible for affecting the dynamic properties of the solution compared with bulk-liquid water.

Bibliography

[1] M. Chaplin, *Anomalous properties of water*, last updated by M. Chaplin on 7 November, 2020. [Internet URL] http://www1.lsbu.ac.uk/water/anmlies.html. Retrieved on 9 November, 2020.

[2] M. Chaplin, *Do we underestimate the importance of water in cell biology?*, Nat Rev Mol Cell Biol. 2006 Nov;7(11):861-6. doi:10.1038/nrm2021. Epub 2006 Sep 6. PMID: 16955076.

[3] Collins, K. D.; Washabaugh, M. W. Q. Rev. Biophys. 1985, 18 (4), 323–422.

[4] Ruiz-Agudo, E.; Kowacz, M.; Putnis, C. V; Putnis, A. Geochim. Cosmochim. Acta 2010, 74 (4), 1256–1267.

[5] F. Hofmeister Naunyn-Schmiedebergs Arch. Pharmacol., 1888, 24 , 247 - 260

[6] W. Kunz , J. Henle and B. W. Ninham , Curr. Opin. Colloid Interface Sci., 2004, 9 , 19 -37

[7] Y. Zhang, P. S. Cremer, Interactions between macromolecules and ions: The Hofmeister series. Curr. Opin. Chem. Biol. 10, 658–663 (2006).

[8] H. Donald, B. Jenkins, Y.Marcus, Chem. Rev. 1995, 95, 8, 2695–2724

[9] G.Jones, M.Dole, J. Am. Chem. Soc. 1929, 51, 10, 2950–2964

[10] Cox, W. M.; Wolfenden, J. H. Proc. R. Soc. (London) 1934, A145, 475.

[11] K.Collins, Biophysical Journal Volume 72 January 1997 65-76
[12] Gurney, R. W. Ionic Processes in Solution; McGraw-Hill: New York, 1953.
[13] Ohtaki, H.; Radnai, T. Structure and Dynamics of Hydrated Ions. Chem. Rev. 1993, 93, 1157−1204.
[14] Krestov, G. A. Thermodynamics of Solvation; Ellis Horwood: New York, 1991.
[15] Omta, A. W.; Kropman, M. F.; Woutersen, S.; Bakker, H. J. Negligible Effect of Ions on the Hydrogen-Bond Structure in Liquid Water. Science 2003, 301, 347−349.
[16] Naslund, L.-Å.; Edwards, D. C.; Wernet, P.; Bergmann, U.; ̈Ogasawara, H.; Pettersson, L. G. M.; Myneni, S.; Nilsson, A. X-ray Absorption Spectroscopy Study of the Hydrogen Bond Network in the Bulk Water of Aqueous Solutions. J. Phys. Chem. A 2005, 109, 5995−6002.
[17] Juurinen, I., Pylkkanen, T., Ruotsalainen, K. O., Sahle, C. J., Monaco, G.; Hama¨ lä inen, K.; Huotari, S.; Hakala, M. Saturation, Behavior in X-ray Raman Scattering Spectra of Aqueous LiCl. J. Phys. Chem. B 2013, 117, 16506−16511.
[18] Smiechowski, M.; Sun, J.; Forbert, H.; Marx, D. Solvation Shell´ Resolved THz Spectra of Simple Aqua Ions−Distinct Distance- and Frequency-Dependent Contributions of Solvation Shells. Phys. Chem. Chem. Phys. 2015, 17, 8323−8329
[19] Ding, Y.; Hassanali, A. A.; Parrinello, M. Anomalous Water Diffusion in Salt Solutions. Proc. Natl. Acad. Sci. U. S. A. 2014, 111, 3310−3315.
[20] P. Debye, Polar Molecules by P. Debye, Chemical Catalog, New York, NY, USA, 1929.
[21] Verlet, L. [1967], ‘Computer” experiments” on classical fluids. I.

Thermodynamical properties of Lennard-Jones molecules', Phys. Rev. 159(1), 98.
[22] Nos´e, S. [1984a], 'A molecular dynamics method for simulations in the canonical ensemble', Mol. Phys. 52(2), 255–268.
[23] Hoover,W. [1985], 'Canonical dynamics: Equilibrium phase-space distributions', Phys. Rev. A 31(3), 1695–1697.
[24] VandeVondele, J., Iannuzzi, M. and Hutter, J. [2006], Large scale condensed matter calculations using the gaussian and augmented plane waves method, in M. Ferrario, G. Ciccotti and K. Binder, eds, 'Computer Simulations in Condensed Matter Systems: From Materials to Chemical Biology Volume 1', Vol. 703 of Lecture Notes in Physics, Springer Berlin Heidelberg, Berlin, Heidelberg, pp. 287–314.
[25] S. Friesen, G. Hefter, R. Buchner, J. Phys. Chem. B 2019, 123, 891–900.
[26] J. Phys. Chem. B 2020, 124, 37, 8141–8148
[27] Todorov, I. T., Smith, W., Trachenko, K. & Dove, M. T. DL_POLY_3: new dimensions in molecular dynamics simulations via massive parallelism. J. Mater. Chem. 16, 1911–1918 (2006).
[28] Berendsen, H. J. C., Postma, J. P. M., van Gunsteren, W. F., DiNola, A. & Haak, J. R. Molecular dynamics with coupling to an external bath. J. Chem. Phys. 81, (1984).
[29] Ewald, P. P. Die Berechnung optischer und elektrostatischer Gitterpotentiale. Ann. Phys. 369, 253–287 (1921).
[30] Berendsen, H. J. C., Grigera, J. R. & Straatsma, T. P. The missing term in effective pair potentials. J. Phys. Chem. 91, 6269–6271 (1987).
[31] Ryckaert, J.-P., Ciccotti, G. & Berendsen, H. J. C. Numerical integration of the cartesian equations of motion of a system with constraints:

molecular dynamics of n-alkanes. J. Comput. Phys. 23, 327–341 (1977).
[32] J. Hutter, M. Iannuzzi, F. Schiffmann, J. VandeVondele, Wiley Interdiscip.Rev.: Comput. Mol. Sci. 2014, 4, 15–25.
[33] J. Perdew, K. Burke, M. Ernzerhof, Phys. Rev. Lett. 1996, 77, 3865–3868.
[34] S. Grimme, J. Antony, S. Ehrlich, H. Krieg, J. Chem. Phys. 2010, 132, DOIhttps://doi.org/10.1063/1.3382344.
[35] J. Schmidt, J. Van de Vondele, I.-F. W. Kuo, D. Sebastiani, J. I. Siepmann,J. Hutter, C. J. Mundy, J. Phys. Chem. B 2009, 113, 11959–11964.
[36] R. Jonchiere, A. P. Seitsonen, G. Ferlat, A. M. Saitta, R. Vuilleumier, J. Chem. Phys. 2011, 135, 154503
[37] S. Goedecker, M. Teter, J. Hutter, Phys. Rev. B 1996, 54, 1703–1710.
[38] T. T. Duignan, G. K. Schenter, J. L. Fulton, T. Huthwelker, M. Balasubramanian, M. Galib, M. D. Baer, J. Wilhelm, J. Hutter, M. Del Ben, X. S. Zhao, C. J. Mundy, Phys. Chem. Chem. Phys. 2020, 22, 10641–10652.
[39] M. Galib, M. D. Baer, L. B. Skinner, C. J. Mundy, T. Huthwelker, G. K. Schenter, C. J. Benmore, N. Govind, J. L. Fulton, J. Chem. Phys. 2017, 146, 84504.
[40] V. A. Glezakou, Y. Chen, J. L. Fulton, G. K. Schenter, L. X. Dang, Theor. Chem. Acc. 2006, 115, 86–99.
[41] S. Roy, V. S. Bryantsev, J. Phys. Chem. B 2018, 122, 12067–12076.
[42] D. Di Tommaso, N. H. de Leeuw, Cryst. Growth Des. 2010, 10, 4292–4302.
[43] K. M. Callahan, N. N. Casillas-Ituarte, M. Roeselová, H. C. Allen, D. J. Tobias, J. Phys. Chem. A 2010, 114, 5141–5148.
[44] I. Bakó, J. Hutter, G. Pálinkás, J. Chem. Phys. 2002, 117, 9838–9843.

[45] J. L. Fulton, S. M. Heald, Y. S. Badyal, J. M. Simonson, J. Phys. Chem. A 2003, 107, 4688–4696.
[46] A. Chatterjee, M. K. Dixit, B. L. Tembe, J. Phys. Chem. A 2013, 117, 8703–8709.
[47] J. Åqvist, J. Phys. Chem. 1990, 94, 8021–8024.
[48] X. Zhang, P. Alvarez-Lloret, G. Chass, D. Di Tommaso, Eur. J. Mineral. 2019, 31, 275–287.
[49] A. Bleuzen, L. Helm, A. E. Merbach, Magn. Reson. Chem. 1997, 35, 765–773.
[50] S. Evans et al, Meas. Sci. Technol. 9, 1721-1732 (1995)
[51] U. Kaatze, Meas. Sci. Technol. 18, 967-976 (2007)
[52] Barthel, Chem. Phys. Lett, 306, 57 (1999)
[53] Buchner, J. Chem. Phys. 119, 10789 (2003)
[54] Sato, T., Chiba, A., & Nozaki, R. (1999). Dynamical aspects of mixing schemes in ethanol–water mixtures in terms of the excess partial molar activation free energy, enthalpy, and entropy of the dielectric relaxation process. The Journal of Chemical Physics, 110(5), 2508. http://doi.org/10.1063/1.477956
[55] O Kratky, H Leopold, H Stabinger Z. Angew. Phys., 27 (1969), p. 273
[56] Mat. Res. vol.20 no.2 São Carlos Mar./Apr. 2017 Epub Feb 06, 2017 http://dx.doi.org/10.1590/1980-5373-mr-2016-0318
[57] Y. Marcus, Chem. Rev. 1988, 88, 1475–1498.
[58] H. Ohtaki, T. Radnai, Chem. Rev. 1993, 93, 1157–1204.
[59] T. S. Hofer, H. T. Tran, C. F. Schwenk, B. M. Rode, J. Comput. Chem. 2004, 25, 211–7.
[60] S. Kerisit, S. C. Parker, J. Am. Chem. Soc. 2004, 126, 10152–10161.
[61] D. Spångberg, K. Hermansson, P. Lindqvist-Reis, F. Jalilehvand, M.

Sandström, I. Persson, J. Phys. Chem. B 2000, 104, 10467–10472.
[62] L. X. Dang, J. Phys. Chem. C 2014, 118, 29028–29033.
[63] P. Raiteri, R. Demichelis, J. D. Gale, J. Phys. Chem. C 2015, 119, 24447–24458.
[64] K. M. Callahan, N. N. Casillas-Ituarte, M. Roeselová, H. C. Allen, D. J. Tobias, J. Phys. Chem. A 2010, 114, 5141–5148.
[65] N. Schwierz, J. Chem. Phys. 2020, 152, 224106.
[66] A. P. Gaiduk, C. Zhang, F. Gygi, G. Galli, Chem. Phys. Lett. 2014, 604, 89–96.
[67] D. Di Tommaso, E. Ruiz-Agudo, N. H. De Leeuw, A. Putnis, C. V. Putnis, Phys. Chem. Chem. Phys. 2014, 16, 7772–7785.
[68] Chandra Phys. Rev. Lett. 85, 768 (2000)
[69] A. Luzar, D. Chandler, Phys. Rev. Lett. 1996, 76, 928–931.
[70] F. S. Csajka, D. Chandler, J. Chem. Phys. 1998, 109, 1125–1133.
[71] M. Chen, H. Ko, R. C. Remsing, M. F. Calegari, B. Santra, Z. Sun, 2017, 1–6.
[72] S. Chowdhuri, A. Chandra, Phys. Rev. E 2002, 66, 41203.
[73] S. Koneshan, J. C. Rasaiah, R. M. Lynden-Bell, S. H. Lee, J. Phys. Chem. B 1998, 102, 4193–4204.
[74] S. Chowdhuri, A. Chandra, J. Phys. Chem. B 2006, 110, 9674–9680.
[75] D. Di Tommaso, M. Prakash, T. Lemaire, M. Lewerenz, N. H. De Leeuw,S. Naili, Crystals 2017, 7, DOI 10.3390/cryst7020057.
[76] E. Duboué-Dijon, P. E. Mason, H. E. Fischer, P. Jungwirth, J. Phys. Chem. B 2018, 122, 3296–3306.
[77] Chen et al. PNAS 2017 114: 10846-10851.
[78] V. P. Tayal, B. K. Srivastava, D. P. Khandelwal, H. D. Bist, Appl. Spectrosc. Rev. 1980, 16, 43–134.

[79] N. W. Ockwig, R. T. Cygan, M. A. Hartl, L. L. Daemen, T. M. Nenoff, J.Phys. Chem. C 2008, 112, 13629–13634.

[80] A. Koishi, A. Fernandez-Martinez, B. Ruta, M. Jimenez-Ruiz, R. Poloni, D. Di Tommaso, F. Zontone, G. A. Waychunas, G. Montes-Hernandez, J. Phys. Chem. C 2018, 122, 16983–16991

[81] M. Montagna, F. Sterpone, L. Guidoni, J. Phys. Chem. B 2012, 116,11695–11700

[82] Z. Yin, L. Inhester, S. Thekku Veedu, W. Quevedo, A. Pietzsch, P. Wernet, G. Groenhof, A. Föhlisch, H. Grubmüller, S. Techert, J. Phys. Chem. Lett. 2017, 8, 3759–3764.

[83] D. C. Rapaport, Mol. Phys. 1971, 22, 977–992.

[84] E. Guardia, I. Skarmoutsos, M. Masia, J. Phys. Chem. B 2015, 119, 8926–8938.

[85] A. R. Leach, Molecular Modelling: Principles and Applications, PrenticeHall (Pearson Education), Harlow, 2009

[86] A. Bankura, A. Karmakar, V. Carnevale, A. Chandra, M. L. Klein, J. Phys. Chem. C 2014, 118, 29401–29411.

[87] H. S. Frank, W. Y. Wen, Discuss. Faraday Soc. 1957, 24, 133–140.

[88] M. Kondoh, Y. Ohshima, M. Tsubouchi, Chem. Phys. Lett. 2014, 591,317–322.

[89] A. A. Zavitsas, J. Phys. Chem. B 2001, 105, 7805–7817.

[90] Y. Marcus, J. Phys. Chem. B 2014, 118, 10471–10476.

[91] D. Laage, J. T. Hynes, Proc. Natl. Acad. Sci. 2007, 104, 11167–11172.

[92] D. Laage, J. T. Hynes, Chem. Phys. Lett. 2006, 433, 80–85.

[93] G. Stirnemann, E. Wernersson, P. Jungwirth, D. Laage, J. Am. Chem. Soc. 2013, 135, 11824–11831.

[94] M. Sega, C. Schröder, J. Phys. Chem. A 2015, 119, 1539–1547.

[95] P. Zarzycki, B. Gilbert, Phys. Chem. Chem. Phys. 2020, 22, 1011–1018.
[96] H. J. Bakker, K. J. Tielrooij, N. Garcia-Araez, M. Bonn, Science 2010, 328,1006–1009.
[97] K. J. Tielrooij, S. T. van der Post, J. Hunger, M. Bonn, H. J. Bakker, J. Phys. Chem. B 2011, 115, 12638–12647.
[98] D. M. Wilkins, D. E. Manolopoulos, S. Roke, M. Ceriotti, J. Chem. Phys. 2017, 146, 181103.
[99] Q. A. Besford, A. J. Christofferson, M. Liu, I. Yarovsky, J. Chem. Phys. 2017, 147, 194503.
[100] Y. Chen, H. I. Okur, N. Gomopoulos, C. Macias-Romero, P. S. Cremer, P. B. Petersen, G. Tocci, D. M. Wilkins, C. Liang, M. Ceriotti, S. Roke, Sci. Adv. 2016, 2, e1501891.
[101] Y. Chen, H. I. Okur, C. Liang, S. Roke, Phys. Chem. Chem. Phys. 2017, 19,24678–24688.
[101] D. Saha, A. Mukherjee, J. Phys. Chem. B 2016, 120, 7471–7479.
[102] G. Stirnemann, E. Wernersson, P. Jungwirth, D. Laage, J. Am. Chem. Soc.2013, 135, 11824–11831.
[103] A. Fournier, W. Carpenter, L. De Marco, A. Tokmakoff, J. Am. Chem. Soc. 2016, 138, 9634–9645.
[104] A. Vila Verde, M. Santer, R. Lipowsky, Phys. Chem. Chem. Phys. 2016, 18,1918–1930
[105] R. Buchner, J. Barthel, J. Stauber, Chem. Phys. Lett. 1999, 306, 57–63.
[106] R. Buchner, G. T. Hefter, P. M. May, J. Phys. Chem. A 1999, 103, 1–9.
[107] R. Buchner, C. Hölzl, J. Stauber, J. Barthel, Phys. Chem. Chem. Phys. 2002, 4, 2169–2179.
[108] U. Kaatze, J. Solution Chem. 1997, DOI 10.1007/BF02768829.
[109] M. Kohagen, P. E. Mason, P. Jungwirth, J. Phys. Chem. B 2014, 118,

DOI10.1021/jp5005693.

[110] K. Ulman, S. Busch, A. A. Hassanali, J. Chem. Phys. 2018, 148, 222826.

[111] E. Poli, K. H. Jong, A. Hassanali, Nat. Commun. 2020, 11, 1–13.

[112] I. Leontyev, A. Stuchebrukhov, Phys. Chem. Chem. Phys. 2011, 13,2613–2626.

[113] I. M. Zeron, J. L. F. Abascal, C. Vega, J. Chem. Phys. 2019, 151, DOI10.1063/1.5121392.

Appendix A

Calculation of time correlation function

Protocol for the calculation of time correlation functions

The methodology below been adopted to compute the hydrogen bonding, $S_{HB}(\mathrm{t})$, and reorientation time correlation functions (TCF), $P_1(\mathrm{t})$, defined as the first-order Legendre polynomials of water dipole, a unit bisector of the H–O–H angle ($\vec{\mu}$).

1. Calculate dipole vectors of each water molecules at all time step from trajectory, $\mu_i(t)$: dipole vectors of ith water molecule at time t.
2. Compute the inner product between the unit vectors defining the orientation of the dipole moment of the *i*-th water molecule at the time origin t_o and time t: $\mathbf{u}_i(t_o) \cdot \mathbf{u}_i(t)$.

3. The first-order Legendre polynomial TCF is obtained from the average over whole water molecule in the simulation box (or in the subpopulation of water molecule):

$$P_1^o(t) = \frac{1}{N_w}\sum_i^{N_w} \mathbf{u}_i(t_o)\cdot\mathbf{u}_i(t) \qquad \text{(A. 1)}$$

4. The first-order Legendre polynomial TCF is obtained for several time origin and overlapping intervals [0, t] of equal time length (Fig. A. 1).

5. The value of $P_1(t)$ in the time intervals [0, t] is obtain from the average of $P_1^o(t)$:

$$P_1(t) = \frac{1}{N_o}\sum_i^{N_o} P_1^o(t) \qquad \text{(A. 2)}$$

The calculation of the continuous hydrogen bonding time correlation function, $S_{HB}(t)$, adopted a similar protocol.

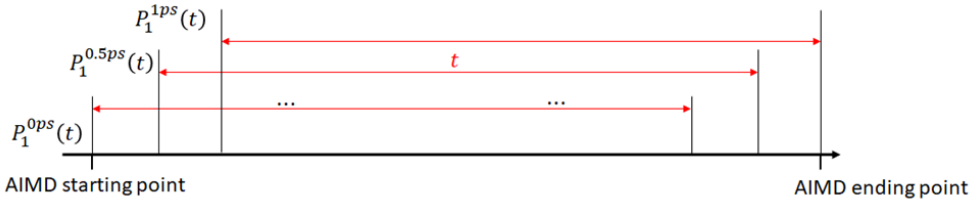

Figure A. 1 Procedure adopted to calculate the value of $\boldsymbol{P_1^o(t)}$ for several time origins and overlapping time of equal time length, [0, t] = 16 ps.

Time average of time correlation functions over several time origin

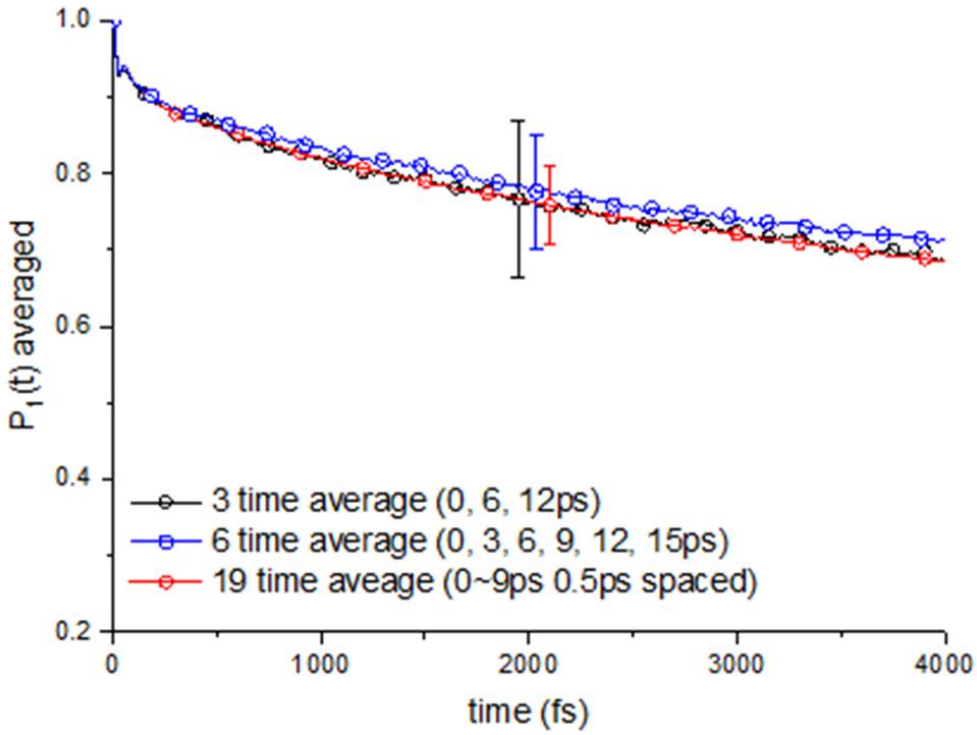

Figure A. 2 First-order Legendre reorientational TCFs, $P_1(t)$, of water in solutions of $MgCl_2$ obtained using indicated time origins. Standard deviation (error bars) decreases by increasing the number of time origins.

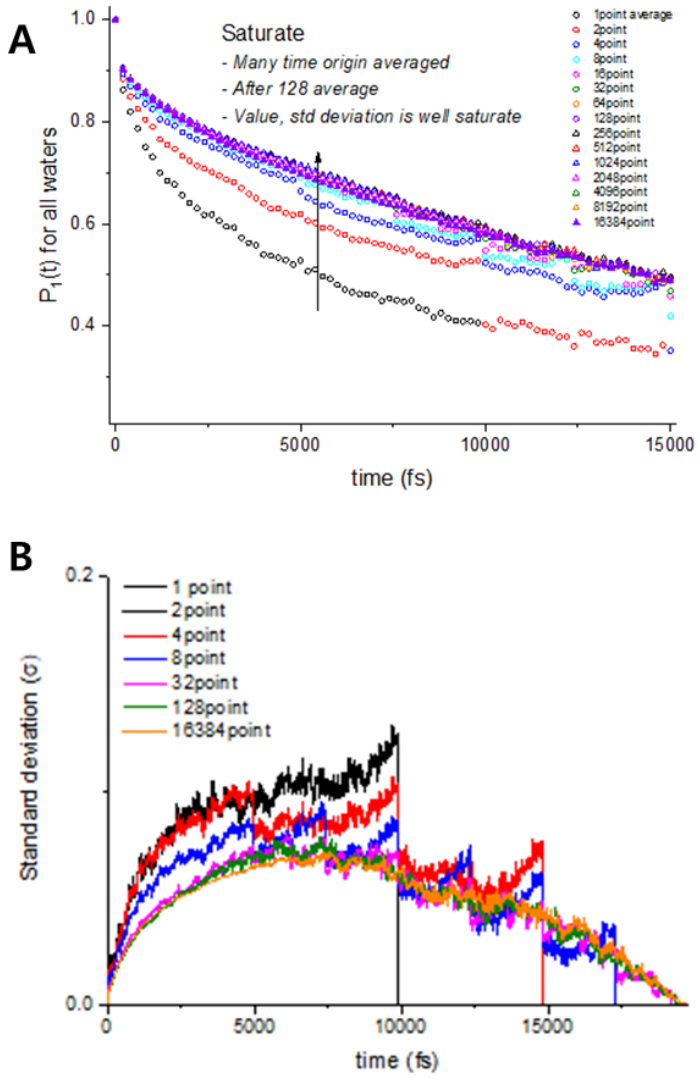

Figure A. 3 First-order Legendre reorientational TCFs, $P_1(t)$, of water in solutions of $MgCl_2$ obtained using indicated time origins. Behavior of the reorientation decay (a) and of the standard deviation (b) with the number of time origins used in the evaluation of $P_1(t)$ (equation A. 2). Time interval used to compute $P_1(t)$ is 16000 steps. Dipole correlation and standard deviation reach convergence after 128 origin time averages.

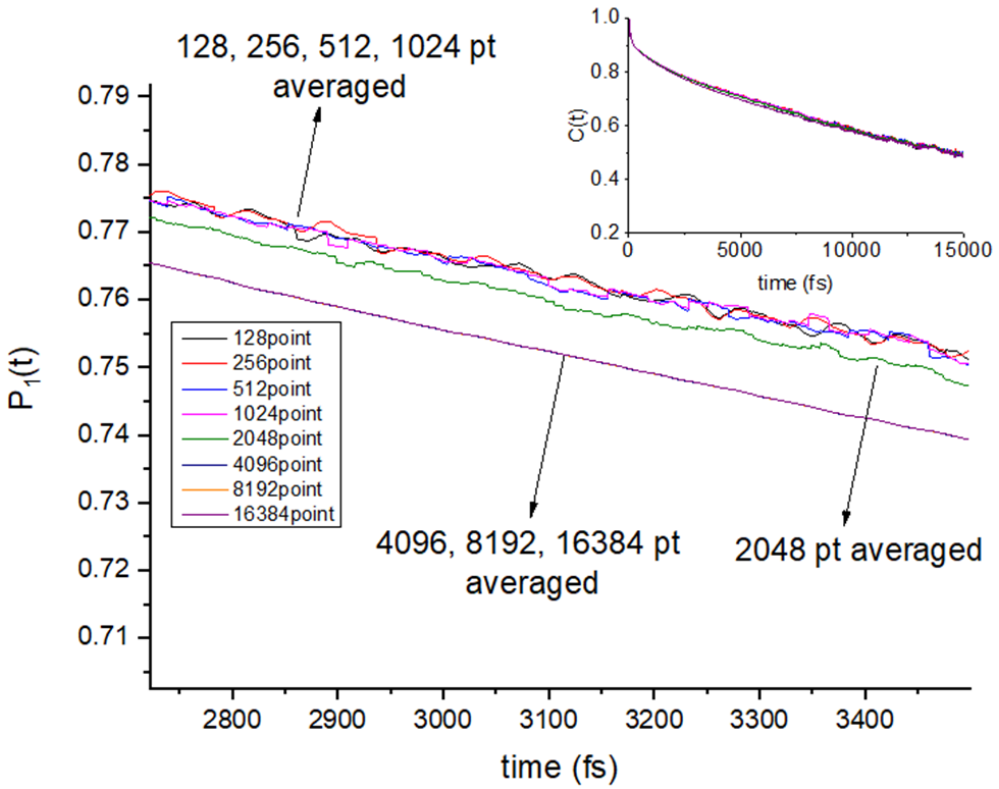

Figure A. 4 First-order Legendre reorientational TCFs, $P_1(t)$, of water in solutions of $MgCl_2$ obtained using indicated time origins. The plots in the time interval [2.8–3.4 ps] show that differences in the computed values of $P_1(t)$ are less than 0.01 (2%).

Appendix B

Connection between single-water molecule reorientational dynamics and DRS measurements

The frequency-dependent dielectric constant (ε) is obtained from the Fourier-Laplace transform of the time-derivative of dielectric decay function (ϕ):

$$\frac{\varepsilon(\omega)-1}{\varepsilon(0)-1}=\int_0^\infty\left(-\frac{d\phi(t)}{dt}\right)e^{-i\omega t}\,dt \qquad \text{(B. 1)}$$

where ϕ is given by the normalized autocorrelation function of the total dipole moment $\vec{P}$ [B. 1]:

$$\phi(t) = \frac{< \vec{P}(t) \cdot \vec{P}(0) >}{< P(0)^2 >} \quad \text{(B. 2)}$$

For an ensemble of (water) molecules, each characterised by an unit vector $\vec{\mu}$ defining the orientation of the molecular dipole moment, the total dipole moment is given by:

$$\vec{P} = \sum_i \vec{\mu}_i \quad \text{(B. 6)}$$

Using this expression for total dipole moment in equation (B. 2), the dielectric decay function can be written in terms of autocorrelation and cross-correlation of the molecular dipole:

$$\phi(t) = \frac{< \vec{\mu}_i(0) \cdot \vec{\mu}_i(t) > + < \vec{\mu}_i(0) \cdot \sum_{j \neq i} \vec{\mu}_j(t) >}{< \mu_i(0)^2 > + < \vec{\mu}_i(0) \cdot \sum_{j \neq i} \vec{\mu}_j(0) >} \quad \text{(B. 4)}$$

$$\phi(t) = \frac{\psi(t) + \gamma(t) - 1}{\gamma(0)} \quad \text{(B. 5)}$$

where $\psi(t)$ denotes the autocorrelation function of the molecular dipole moments,

$$\psi(t) = \frac{< \vec{\mu}_i(0) \cdot \vec{\mu}_i(t) >}{< \mu_i(0)^2 >} \quad \text{(B. 6)}$$

and $\gamma(t)$ denotes the multi-molecular dipole cross-correlation function,

$$\gamma(t) - 1 = < \vec{\mu}_i(0) \cdot \sum_{j \neq i} \vec{\mu}_j(t) > / < \mu_i(0)^2 > \quad \text{(B. 7)}$$

Let us assume that the auto-correlation function of the molecular dipole $\psi(t)$ and the auto-correlation of the total dipole $\phi(t)$ are governed by one correlation time:

$$\tau_{\phi} = -\phi(t)/\{d\phi(t)/dt]$$
$$\tau_{\psi} = -\psi(t)/\{d\psi(t)/dt] \quad \text{(B. 8)}$$

where τ_{ϕ} and τ_{ψ} are the *macroscopic* decay function and *molecular* dipole moment decay function, respectively. The expression connecting these two functions has been derived by Kivelson and Madden [B.2]:

$$\tau_{\phi} = \tau_{\psi}\left[1 + \frac{<\overrightarrow{\mu_{\iota}(0)} \cdot \sum_{i\neq j}\overrightarrow{\mu_1(t)}>}{<\mu_i(0)^2>} >\right] = \tau_{\psi}\gamma(0) \quad \text{(B. 9)}$$

Since the steady function $\gamma(0)$ corresponds to the Kirkwood dipole orientation correlation factor, g_K,[18] we can simply rewrite equation (B. 9) as:

$$\tau_{\psi} = \tau_{\phi}/g_K \quad \text{(B. 10)}$$

In our study, we have found that the relaxation time of the molecular dipole correlation function τ_{ψ} of certain water subpopulation are retarded (2 to 6 times slower) compared to bulk-like water molecules. On the other hand, τ_{ϕ} is the same for all water subpopulation because the macroscopic relaxation time is obtained from the total dipole auto-correlation. it follows from equation (B. 10) that water subpopulations with a retarded reorientation dynamics have a lower Kirkwood factor compare to the bulk-like water. Based on the conclusion made by Rinne et al. on single water versus collective water effects on ion-specific reorientation water dynamics [B. 3], the presence of an ion perturbs the cooperative structure of water in the subpopulations with a retarded reorientation dynamics because ion because of lower Kirkwood dipole orientation correlation factor. The lower dipole correlation factor of the water subpopulation with retarded dipole correlation makes this water subpopulation less contribute to bulk relaxation dynamics. This interpretation

is also corroborated by the reduction of multi-molecular dipole cross-correlation contribution in the dielectric loss spectrum calculated, as suggested by Rinne et al. [B. 3] Also, in the dielectric relaxation spectroscopy, the hydration number is calculated from the dielectric loss spectrum of electrolyte solution compare to bulk water. This leads to a decrease in the dielectric loss spectrum (static depolarization) and from static depolarization we can get hydration number.

To summarize, the hydration number computed from the water reorientation dynamic analysis of ab initio and classical MD simulations connects to THz-DR experimental values as follow: the presence of ions in solution can cause the single-molecule reorientation dynamic of some water subpopulations to be slower than bulk water; water subpopulation with retarded reorientational dynamics have lower correlation with other water molecules compared to bulk-like water; in these water subpopulation the multi-molecular dipolar correlation contribution to the dielectric loss spectrum is decreased; as a result, the dielectric loss spectrum, which is measured by DRS is lower than that of bulk water.

[B. 1] D. van der Spoel, P. J. van Maaren, H. J. C. Berendsen, J. Chem. Phys. 1998, 108, 10220–10230.

[B. 2] D. Kivelson, P. Madden, Mol. Phys. 1975, 30, 1749–1780.

[B. 3] K. F. Rinne, S. Gekle, R. R. Netz, J. Phys. Chem. A 2014, 118, 11667–11677.

Appendix C

Water exchange between different subpopulations

In this work, we simply tracked the water molecules belonging to a specific water subpopulation at the time origin (t = 0 ps) for calculating the dipole TCF of each water subpopulation:

$$P_1^o(t) = \frac{1}{N} \sum_{i \in W_{abc}}^{N} \mathrm{u}_i(t_o) \cdot \mathrm{u}_i(t) \qquad \text{(C. 1)}$$

This approximation has been adopted by other groups to compute time correlation functions of dynamical properties of different water layers at solid/water and air/water interfaces [C. 1-3]. However, water molecules that are in a particular subpopulation at *t* = 0 ps, e.g. W_{12B} and W_{12B} in Fig. C. 1,

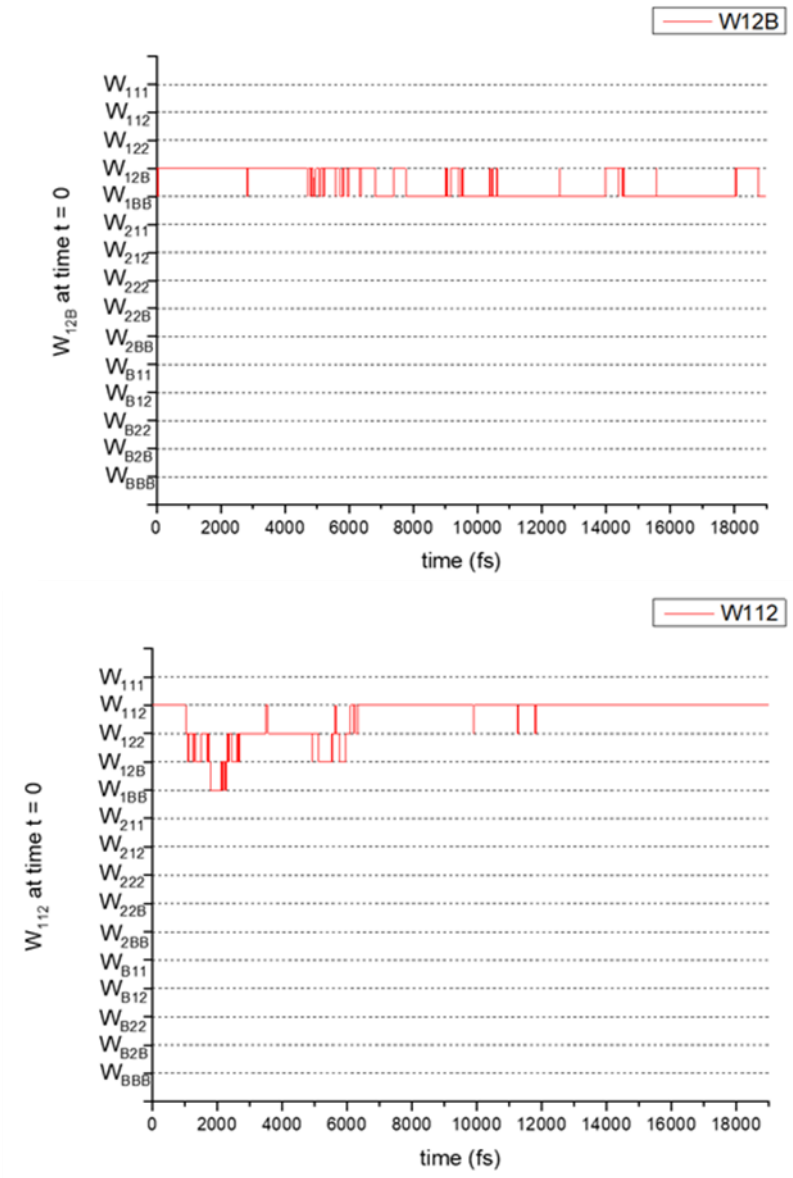

Figure C. 1 Exchange of water molecules between different water subpopulations. Analysis conducted on the 0.6 mol.kg^{-1} $MgCl_2$ solution.

can exchange to "neighboring" subpopulations. For example, a water molecule that is W_{12B} initially goes to W_{1BB}, a neighbor subpopulation, but molecules in both subpopulations contribute to the hydration water.

From the graphs in Fig. C. 1 we can distinguish two kinds of phenomena: *short-time fluctuations* and *long-term exchange*. Short term fluctuation (top figure) are fast exchanges of a water molecule between the initial subpopulation (t = 0 ps) and neighboring water subpopulations, which can occur because of rotational or vibrational motion of molecules that are at the margin of the distance criteria distinguishing between subpopulations. A long-term exchange (bottom figure) is seen when a water molecule exists for a considerable time in different water subpopulations and then returns to initial subpopulation or moves into another one; it could occur because of the translational motion of water between neighboring ions. To analyze the long term exchange in more detail, let us consider a simplified hydration model, W_{ab}, that only considers the positions of the oxygen atom: a, b = 1, 2, or B, where 1 corresponds to O in the 1st shell of Mg or Cl, 2 corresponds to O in the 2nd shell of Mg or Cl, and B corresponds to O beyond the 2nd shell of Mg or Cl. Using this simplified classification method, we can exclude the short-term fluctuation and focus on the temporal behavior of the long term exchanges. Let us now define the following function:

$$N_{ab}(t) = \frac{1}{N_{ab}(0)} \sum_{i \in W_{ab}}^{N_{ab}(0)} F_i(t) \qquad \text{(C. 2)}$$

where $N_{ab}(0)$ corresponds to the number of water molecules in the subpopulation W_{ab} at time t = 0, and the quantity $F_i(t)$ is computed as follows:

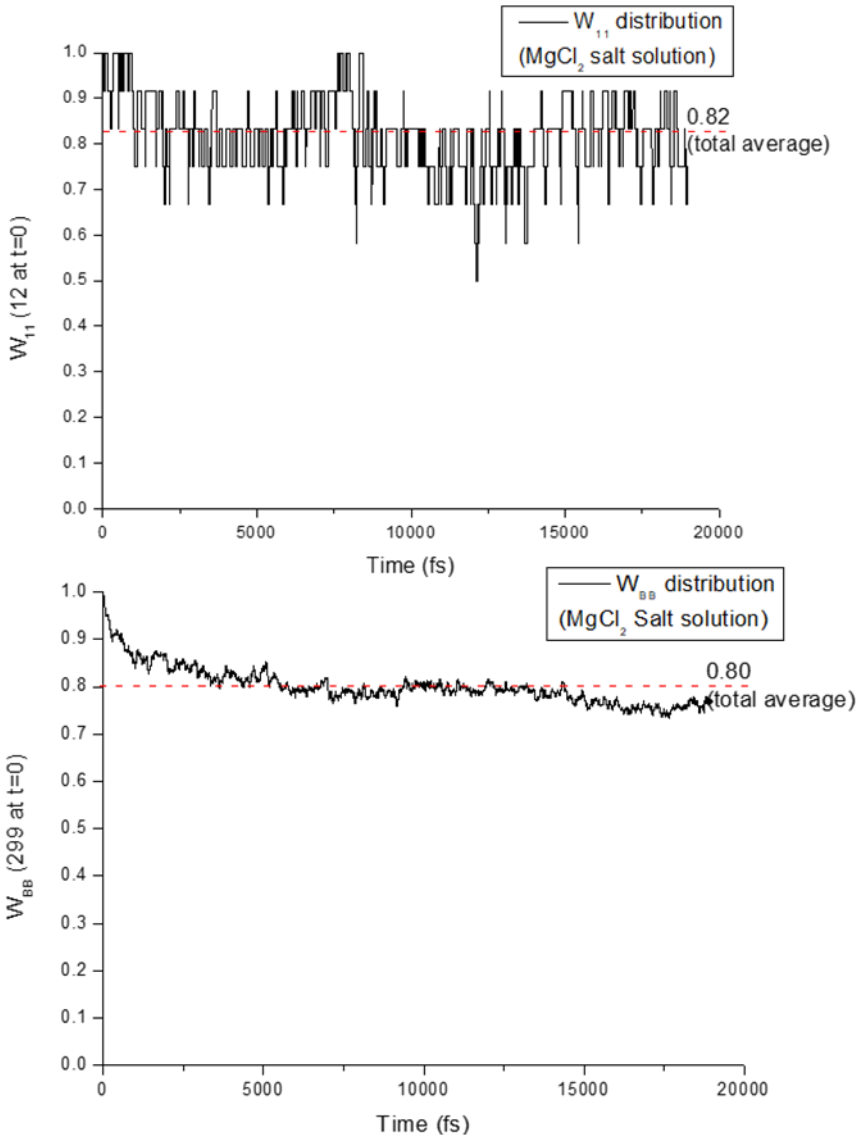

Figure C. 2 Fraction of water molecules that have remained in the same category at time t. W_{11} (top) W_{BB} (bottom)

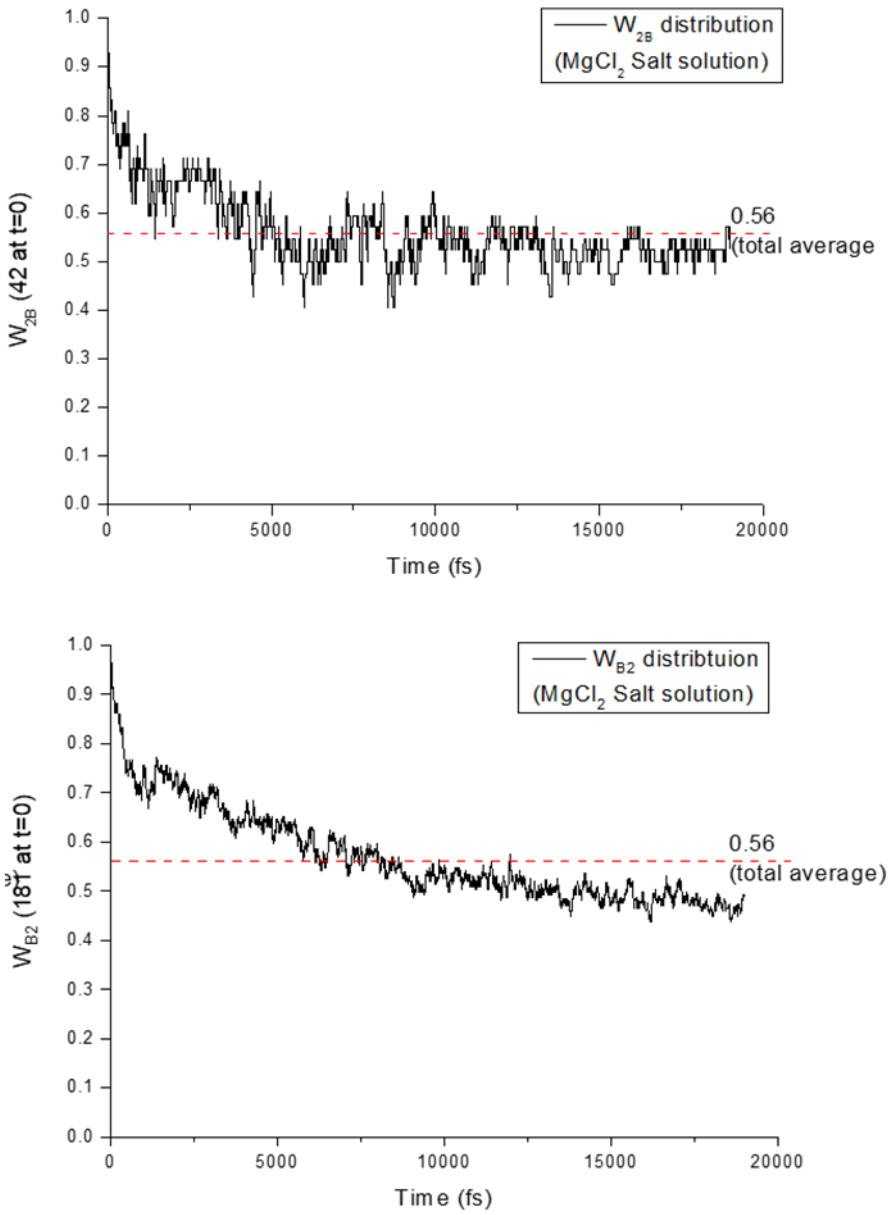

Figure C. 3 Fraction of water molecules that have remained in the same category at time t. W_{2B} (top) W_{B2} (bottom)

$$F_i(t) = \begin{cases} 1 & \text{if } i \in W_{ab} \\ 0 & \text{if } i \notin W_{ab} \end{cases} \quad \text{(C. 3)}$$

The normalized, time-dependent function $N_{ab}(t)$ corresponds to the fraction of water molecules initially in W_{ab} that have remained in the same category. Fig. C. 2 shows that W_{11} (water molecules in the first hydration shell of Mg and Cl) is quite "rigid" as more than 80% of water molecules remained in the original subpopulation. Also, about 80% of water molecule which is initially bulk water is still belongs to W_{BB} under dynamic exchange equilibrium. In case of water molecules in the second shell either Mg^{2+} and Cl^- ion, (W_{B2}, W_{2B}) between 50 and 60 % remains in the same category. In order to minimize the effect originating from the exchange of water molecules from one subpopulation to another, we used the first 8000 steps data (8ps) of the dipole correlation function to fit the bi-exponential model which give us the averaged relaxation time; this gives more than 70% of water molecules remaining in the initial category. Water molecules of each subpopulation are exchanged with each other, but the relaxation time of dipole correlation function we have obtained is fitted over time intervals that exchange effect is not significant to dipole correlation function because majority of water molecules remain same category.

[C. 1] S. Pezzotti, D. R. Galimberti, M.-P. Gaigeot, Phys. Chem. Chem. Phys. 2019, 21, 22188–22202.

[C. 2] S. Pezzotti, D. R. Galimberti, Y. R. Shen, M. P. Gaigeot, Minerals 2018, 8, 1–16.

[C. 3] R. Khatib, E. H. G. Backus, M. Bonn, M. J. Perez-Haro, M. P. Gaigeot, M. Sulpizi, Sci. Rep. 2016, 6, 1–10.

Appendix D

Reorientation time correlation function analysis from classical MD

The retardation factor associated with the water subpopulations of $MgCl_2$ was determined with the approach used for ab initio MD (Fig. D. 1). Also, the slow-reorienting water and bulk-like water was classified as the manner used for ab initio MD (Calculate average relaxation time and its deviation of bulk-like water and water category with reorientation relaxation time slower than bulk-like water over 3σ is classified slow-reorienting water (hydration water). Finally, the hydration number per unit $MgCl_2$ can be obtained using the distribution of each category (inset of Fig. D. 1).

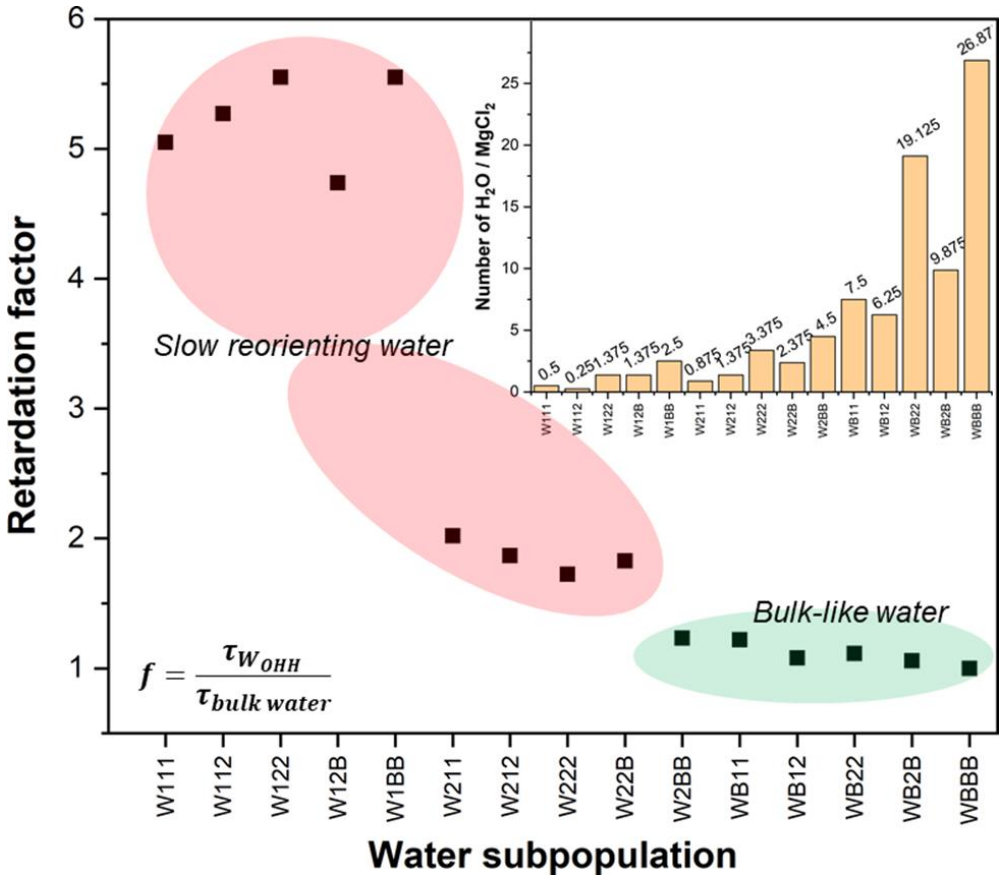

Figure D. 1 Retardation factor for the reorientation relaxation time of the water subpopulations obtained from classical MD simulation of the 0.6 mol.kg^{-1} solution using the Duboue-Dijon forcefield. *Inset*: number of water molecules per $MgCl_2$ units in each subpopulation.

Appendix E

Information on DRS of $MgCl_2$ (aq)

This section summarizes the results of the double Debye fitting, conductivity measurement, and density measurement related to the dielectric relaxation spectroscopy. Conductivity (Fig E. 1) was measured to determine the contribution of dielectric relaxation due to reorientation, excluding Ohmic loss. Density measurement (Fig E. 2) was performed as a supporting experiment to accurately calculate the molar concentrations of water and ions in the electrolyte solution based on accurate density measurements. Based on these data, the concentration dependent hydration number described in the main text was obtained.

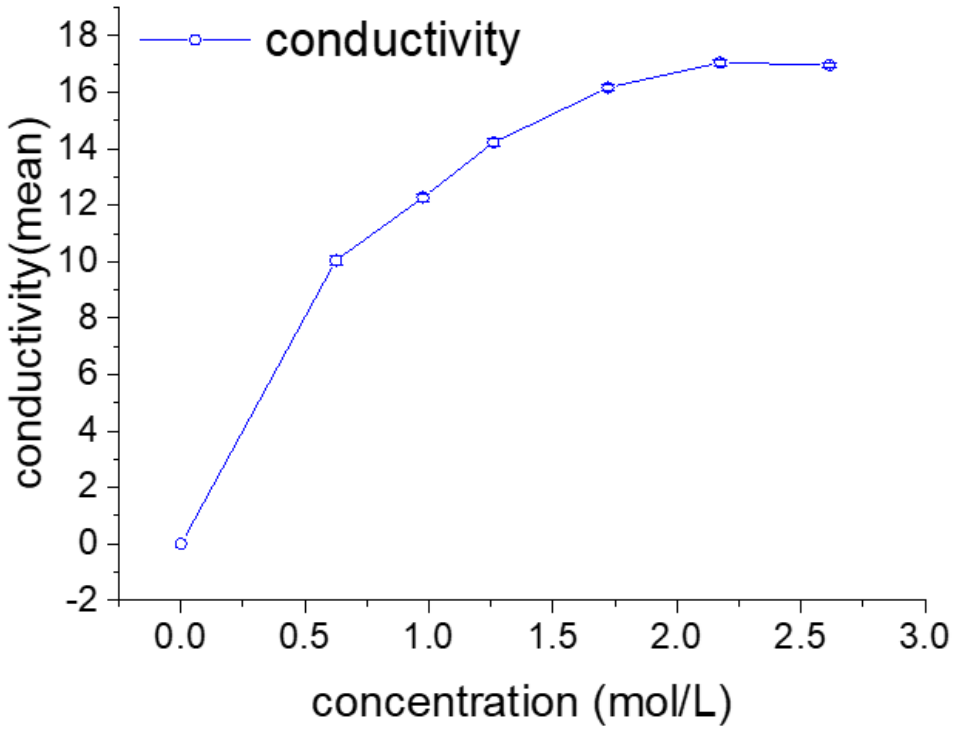

Figure E. 1 Conductivity measurement on MgCl2 aqueous solution in concentration of 0.0764-2.81 mol kg^{-1}

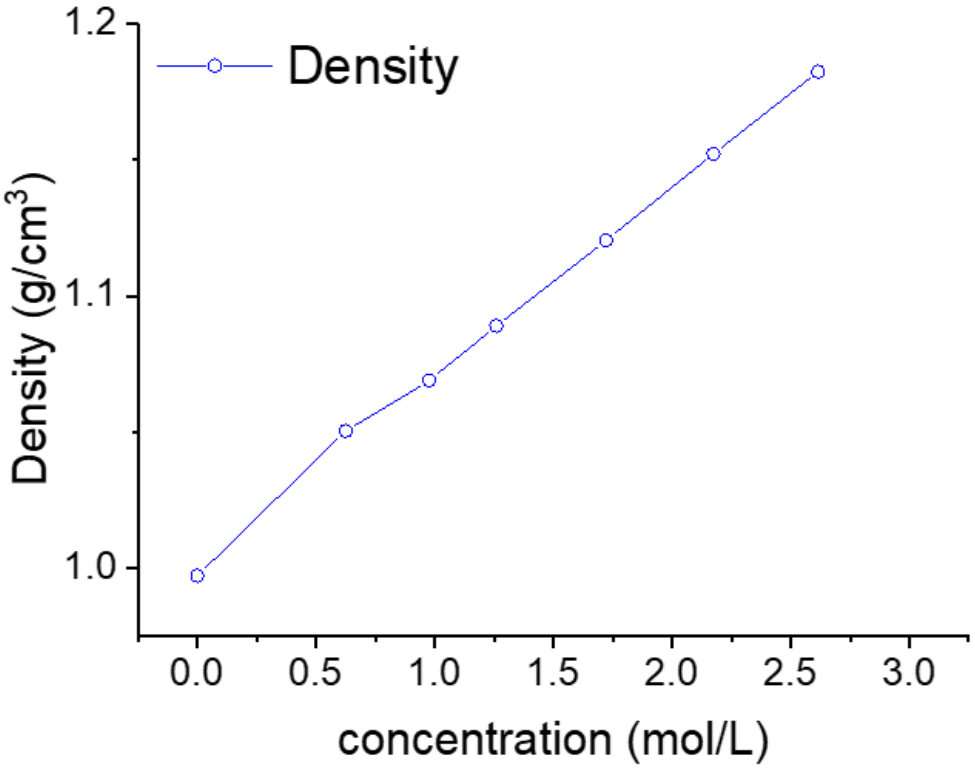

Figure E. 2 Density measurement on MgCl2 aqueous solution in concentration of 0.0764-2.81 mol kg^{-1}

The double Debye model fitting for DRS on $MgCl_2$ aqueous solution:

$$\varepsilon(\omega) = \frac{S_1}{1 + i\omega\tau_D} + \frac{S_2}{1 + i\omega\tau_2} + \varepsilon_\infty \qquad \text{(E. 1)}$$

and the fitting parameters as shown in Fig. E. 3 and E. 4.

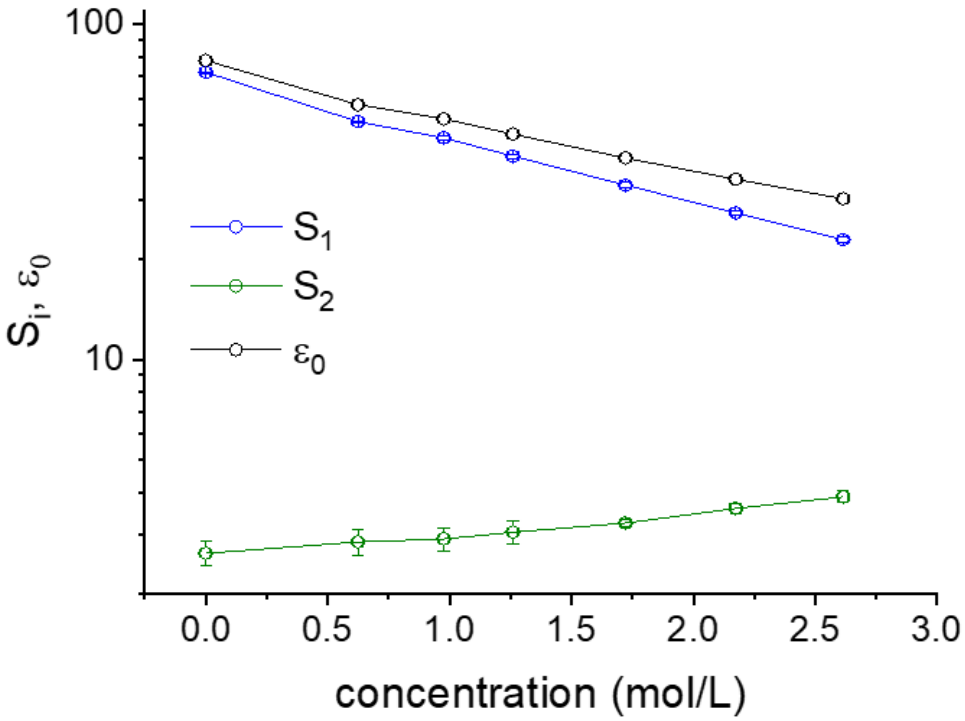

Figure E. 3 Double Debye fitting parameters of MgCl2 aqueous solution in concentration of 0.0764-2.81 mol kg^{-1}

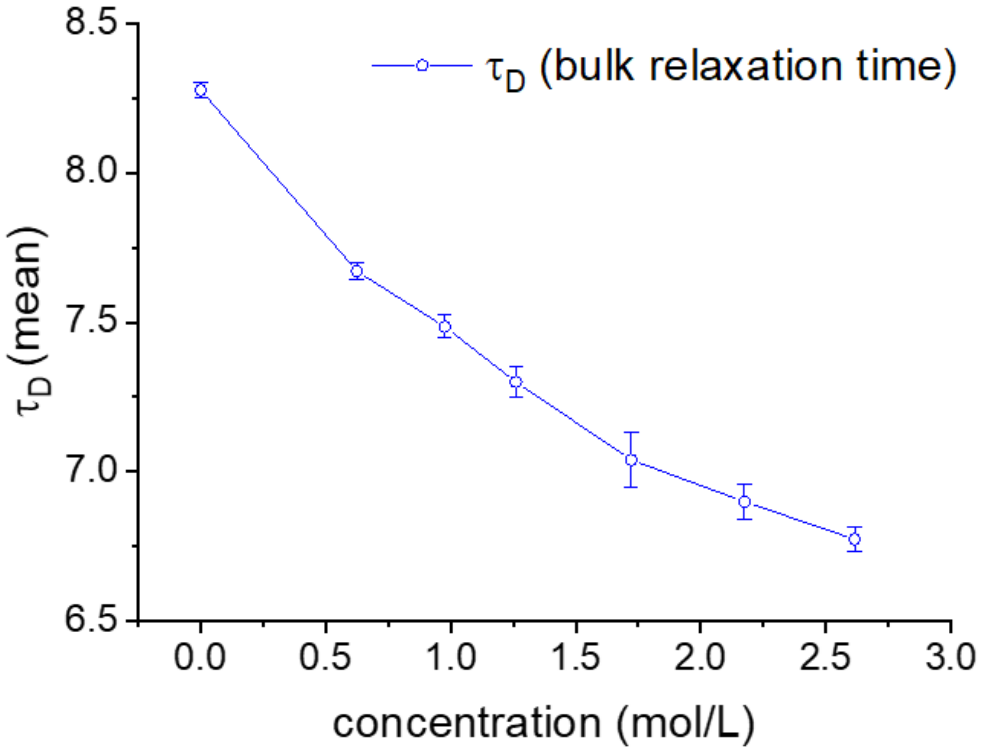

Figure E. 4 Bulk relaxation time of MgCl2 aqueous solution in concentration of 0.0764-2.81 mol kg^{-1}

초록

본 연구에서는 ab-initio 전산 모사와 유전체 분광학의 방법으로 염화마그네슘 전해질 수용액의 구조 및 물 분자의 재배향 동역학을 연구하였다. 또한 이온 수화 현상과 여기서 나타나는 협동 수화 효과를 효과적으로 관찰하기 위해 수화 효과가 강한 MgCl2 수용액을 모델 시스템으로 사용했다. 순수한 물과는 다르게 염화마그네슘은 수용액 상태의 물의 수소 결합 네트워크에 영향을 미치며, 이 영향은 방사 방향 분포 함수 (Radial distribution function), 수소결합 동역학, 진동 모드의 상태 밀도 함수 (vibrational density of states) 등을 통해 확인되었다. 이를 통하여 마그네슘 이온의 제 1 수화 껍질 영역에 물과 마그네슘의 강한 상호작용으로 인해 억류 수(bound water)가 생길 뿐 아니라, 그 너머의 물에 대하여 수소 결합 네트워크의 결속이 약해지는 것을 확인할 수 있었다.

또한 본 연구에서는 이온의 수화 과정 속에서 나타나는 협동 효과를 정량화 할 수 있는 협동 수화 모형을 이용하여 물 분자의 재배향 동역학의 특성을 규명하였다. 위 수화 모형을 통해서 전해질 수용액에서 나타나는 협동 수화 효과는 마그네슘 이온의 제 2 수화 껍질과 염소 이온의 제 1 수화 껍질에 동시에 속하는 물분자에서 주로 나타나며 그 결과로 물의 재배향 동역학이 느려짐을 확인하였다.

마지막으로 거시적인 유전체 분광학 측정과 분자 수준의 전산 모사의 결과 비교를 통하여, 이온의 수화 현상을 가법 효과로 (additive effect) 고려했을 때 농도에 따라 변화하는 수화 수 (hydration number) 를 설명할 수 없으나, 협동 수화 효과를 고려한 모형으로는 정확하게 설명할 수 있음을 확인했다. 이는 미시 영역에서 나타나는 협동 수화 효과가 거시 영역의 수용액의 성질을 결정하는데 중요한 요소가 될 수 있음을 의미한다.

핵심어: 이온 수화, 협동 효과, 전산 모사, 유전체 분광법, 염화마그네슘

학번: 2014-21351